

UNIVERSITY OF LJUBLJANA
FACULTY OF MATHEMATICS AND PHYSICS

Samo Kupper

Charm production in 920 GeV proton-nucleus interactions

DOCTORAL THESIS

ADVISOR: ASSOC. PROF. DR. MARKO STARIČ

LJUBLJANA, 2007

UNIVERZA V LJUBLJANI
FAKULTETA ZA MATEMATIKO IN FIZIKO

Samo Kupper

**Produkcija mezonov s kvarkom c
v trkih protonov energije 920 GeV z jedri**

DISERTACIJA

MENTOR: PROF. DR. MARKO STARIČ

Ljubljana, 2007

Prof. dr. Petru Križanu bi se rad zahvalil za vso potrpežljivost od mojega prvega obiska na Inštitutu Jožef Stefan in na Fakulteti za Matematiko in Fiziko dalje, pred vsem tudi, da mi je omogočil vpis na podiplomski študij fizike osnovnih delcev, da je kot mentor na magistrskem študiju prenašal moje neznanje in mi poleg tega nudil možnost sodelovanja v raziskovalni skupini oddelka F9 na inštitutu Jožef Stefan.

Prof. dr. Svjetlani Fajfer se zahvaljujem za podporo in vzpodbude pri pripravah na vpis in med študijem, dodatno tudi za nasvete in popravke pri izdelavi tega dela.

Dr. Andreju Gorišku se zahvaljujem, da me je naučil prve korake pri obdelavi podatkov zajetih s spektrometrom HERA-B.

Iskrena zahvala gre mentorju prof. dr. Maretu Stariču, ki me je spremljal pri izdelavi tega dela, mi neutrudno pomagal z nešteti nasveti in razlagami tako pri razumevanju detektorja, pri matematičnih pristopih in pri interpretaciji rezultatov, kakor tudi pri uporabi njegovih številnih računalniških pripomočkov za analizo podatkov. Za vsakega mojih problemov je v najkrajšem času našel rešitev in mi potrpežljivo odgovarjal na moja – včasih tudi trivialna – vprašanja. Poleg tega se je mučil z mnogokratnim branjem in popravljanjem mojih dostikrat nedokončnih in pogosto neizdelanih besedil. Brez njegove podpore ne bi prispel do cilja.

Svoji družini se za vso podporo z besedami ne morem zahvaliti – vesel sem, da vas imam!

Abstract

The subject of this thesis is the measurement of open charm cross sections in 920 GeV proton-nucleus interactions with the HERA-B spectrometer. The data were taken with targets of three different materials: carbon, tungsten and titanium. The measurement includes the total production cross sections for the charmed mesons D^0 , D^+ , D_s^+ and D^{*+} as well as for the charm quark pair, the differential cross sections in the longitudinal and in the transverse direction, the dependence of the total production cross section on the atomic number of the target material, the leading to non leading particle asymmetries and the ratios of the charm meson cross sections. The results are compared with the published experimental data and with the theoretical expectations.

PACS: 13.20.Fc, 13.25.Ft, 13.85.Ni, 14.40.Lb, 19.85.+c

Keywords: Particle physics, charm meson production, cross section measurement

Povzetek

V doktorski disertaciji obravnavam analizo zajetih podatkov s spektrometrom HERA-B v trku protonov energije 920 GeV z jedri. Podatki so bili zajeti s tarčami iz ogljika, volframa in titana. Opisane so meritve totalnega produkcijskega preseka za tvorbo mezonov D^0 , D^+ , D_s^+ , D^{*+} in za tvorbo para kvarkov $c\bar{c}$, meritve diferencialnih presekov v vzdožni in prečni smeri, meritve asimetrije vodilnega proti nevodilnemu delcu in meritev odvisnosti totalnega produkcijskega preseka od masnega števila jeder v tarči ter podani rezultati. Na koncu je predstavljena primerjava izmerjenih vrednosti s teoretskimi napovedmi in z objavljenimi rezultati drugih eksperimentov.

PACS: 13.20.Fc, 13.25.Ft, 13.85.Ni, 14.40.Lb, 19.85.+c

Ključne besede: fizika osnovnih delcev, produkcija mezonov c , produkcijski presek

Contents

1	Preface	1
1.1	Introduction	1
1.2	The Standard Model	1
1.3	Quantum Chromodynamics	2
1.4	Charm quark pair production in hadron-hadron collision	3
1.5	The parton distribution function	5
1.6	Interaction	5
1.7	Hadronization	10
1.8	Existing experimental data	11
1.9	Other open charm analyses at HERA-B	16
2	The HERA-B experiment	19
2.1	The HERA accelerator	20
2.2	The HERA-B detector	21
2.3	Target	22
2.4	Vertex detector	22
2.5	Tracking system	23
2.5.1	Inner Tracker	23
2.5.2	Outer Tracker	24
2.6	Ring imaging Cherenkov detector	25
2.7	Electromagnetic calorimeter	26
2.8	Muon chambers	26
2.9	The data acquisition and triggering system	28
2.9.1	Di-lepton trigger	29
2.9.2	Random Trigger	30
2.9.3	Interaction trigger	30
2.10	Luminosity determination	31
3	Data sample	35
3.1	Selected runs	35
3.2	Monte Carlo samples	35

4	Data selection	39
4.1	Reconstruction of D mesons	39
4.2	Analysis cuts	41
4.3	Optimization of analysis cuts	42
4.4	Data signals	47
4.5	D meson life times	53
4.6	Other consistency checks	57
5	Total visible production cross sections	59
5.1	Basic formulae	59
5.2	Efficiency determination	60
5.3	Cross sections	61
5.4	Leading to non-leading particle asymmetries	62
5.5	A-dependence of cross sections	64
6	Kinematical distributions	69
6.1	Parameterization of distributions	69
6.1.1	Transverse momentum	69
6.1.2	Feynman's x variable	70
6.2	Generated distributions with the Monte Carlo simulation	71
6.3	Acceptances	73
6.4	Measurement of $d\sigma/dp_T^2$	76
6.5	Measurement of $d\sigma/dx_F$	80
6.6	Re-weighting of Monte Carlo events	81
6.7	Visible fraction	84
7	Systematic errors	87
7.1	Total visible cross sections	87
7.1.1	Event counting	87
7.1.2	Branching fractions	88
7.1.3	Integrated luminosities	88
7.1.4	Efficiency	88
7.1.5	Summary of systematic uncertainties	91
7.2	Cross section ratios	91
7.3	A-dependence parameter α	92
7.4	Leading to non-leading particle asymmetries	93
8	Results	95
8.1	Corrected cross sections	95
8.2	Cross section for the charm quark pair production	96
8.3	Cross section ratios	96

8.4	Fraction of vector mesons	97
8.5	Leading to non-leading particle asymmetries	98
8.6	A-dependence parameter α	98
9	Summary	99
A	Stability of cuts	101
B	Comparison between MC and data	107
	References	121
	Povzetek doktorskega dela	125
	Rekonstrukcija mezonov D	126
	Selekcija dogodkov	126
	Signalni dogodki	128
	Presek	131
	Kinematske porazdelitve	132
	Sistematske napake	135
	Rezultati	137

1 Preface

1.1 Introduction

Processes with heavy quarks involved are an important test for perturbative quantum chromodynamics (pQCD). In such a theory cross sections can be calculated, if the quark masses are large enough and the contribution of processes with a small momentum transfer is negligible [1, 2, 3].

In the parton model we treat the interaction between two nucleons as an interaction of partons in the nucleon. According to the Factorization theorem [4] we assume that it is possible to divide the cross section into three different parts: the non perturbative initial conditions, the scattering process itself and the hadronization of the decay products.

The mass of the c quark is far from the limit, where contributions with a small momentum transfer can be neglected, so the predictions strongly depend on the selection of the parameters of the model, such as Λ_{QCD} , the factorization scale and the quark mass.

The $c\bar{c}$ production cross section can be determined from the production cross section of one of the charmed mesons, if we know its fragmentation fraction. The c quark factorizes most frequently into mesons D^0 , D^+ and D_s^+ and their excited states. The predictions of a simple model for the fragmentation fractions [1] are approximately: 60% (D^0), 20% (D^+) and 10% (D_s^+); the remaining fraction is due to fragmentation into charmed baryons. The probability that a $c\bar{c}$ bound state is formed (like J/ψ), is suppressed by two orders of magnitude.

Charmed mesons are identified as a peak in the invariant mass distribution of its decay products. The most suitable decay channels of ground state charmed mesons are*:

$$\begin{aligned} D^0 &\rightarrow K^-\pi^+, \\ D^+ &\rightarrow K^-\pi^+\pi^+ \\ D_s^+ &\rightarrow \phi\pi^+ \rightarrow K^-K^+\pi^+. \end{aligned}$$

1.2 The Standard Model

The Standard Model is a gauge theory based on the symmetry group $SU(3)_C \times SU(2)_L \times U(1)_Y$. It describes the strong and electroweak interactions of elementary pointlike fermions, mediated by gauge bosons [5].

*Throughout this work charge conjugate states are implied.

The fundamental constituents of matter, the leptons and quarks, are organized in three generations. There are three leptons with electric charge -1 : the electron (e^-), the muon (μ^-) and the tau (τ^-), and three electrically neutral leptons, the electron neutrino (ν_e), the muon neutrino (ν_μ) and the tau neutrino (ν_τ). Similarly there are three quarks with electrical charge $-1/3$, the down (d), strange (s) and bottom (b) quark and also three quarks with an electrical charge $+2/3$, the up (u), charm (c) and top (t) quark. The left handed fermions form doublets of the weak isospin $SU(2)_L$, while the right handed ones are singlets. The generator of the $U(1)_Y$ component of the electroweak gauge group is the hypercharge Y , which is twice the difference between the electrical charge and the weak isospin. For each particle there exists a corresponding antiparticle. Quarks are triplets of $SU(3)_C$ group; they carry color as an additional quantum number. Between the generations of quarks there is mixing, which is parameterized by the Cabibbo-Kobayashi-Maskawa (CKM) matrix. The origin of this matrix is not explained by the Standard Model. In the Standard Model the neutrinos are massless, and therefore there is no mixing between different generations of leptons.

The electroweak interaction, which is described by the the $SU(2)_L \times U(1)_Y$ symmetry group, is spontaneously broken by the existence of the scalar Higgs field with a non-zero vacuum expectation value. This leads to the appearance of massive vector bosons W^+ , W^- and Z^0 , which mediate the weak interaction, while the photon, which mediates the electromagnetic force, remains massless. One physical degree of freedom remains in the Higgs sector, which should manifest as a massive neutral scalar boson H^0 .

The strong interaction is mediated by eight massless gluons. Gluons carry color charges and are therefore self interacting. The strong coupling constant α_s is small for large momentum transfers and becomes large for small momentum transfers. This behavior leads to the confinement of quarks inside color neutral bound systems. Attempting to free a quark leads to the production of jets of hadrons through a production of quark-antiquark pairs and gluons.

1.3 Quantum Chromodynamics

Quantum Chromodynamics (QCD) describes the strong interaction and is a non-Abelian gauge quantum field theory. The Lagrange density describing the interaction of quarks and gluons can be written as [6]:

$$L = -\frac{1}{4}G_{\mu\nu}^a G_a^{\mu\nu} + \sum \bar{q}_f^\alpha (i\gamma^\mu D_\mu - m_f) q_f^\alpha \quad (1.1)$$

where

$$G_{\mu\nu}^a = \partial_\mu G_\nu^a - \partial_\nu G_\mu^a + g_s f_{abc} G_\mu^b G_\nu^c \quad (1.2)$$

$$D_\mu = \partial_\mu - ig_s \frac{\lambda^a}{2} G_\mu^a \quad (1.3)$$

q_f are Dirac bi-spinors with indices α for three colors and f for six flavors and m_f is a quark mass. G_μ^a are the eight gluon fields, D_μ is the covariant derivative, which ensures the gauge invariance of the Lagrange density in respect to local transformations of the type

$$q_f^\alpha \rightarrow (q_f^\alpha)' = U_\beta^\alpha q_f^\beta \quad (1.4)$$

where the $SU(3)$ matrices U_β^α are written in the form

$$U_\beta^\alpha = \exp \left\{ -ig_s \frac{\lambda^a}{2} \theta_a(x) \right\}, \quad (1.5)$$

matrices λ^a ($a = 1, 2, \dots, 8$) are the generators of the fundamental representation of the $SU(3)_C$ algebra, $\theta_a = \theta_a(x)$ are eight arbitrary parameters, g_s is the coupling constant of the strong interaction and f_{abc} are the structure constants of the $SU(3)$ algebra. In all equations we use Einstein's convention, summing over repeated indices.

Using Eqs. 1.2 and 1.3 the Lagrangian density Eq. 1.1 can be rewritten as:

$$\begin{aligned} L_{QCD} = & -\frac{1}{4}(\partial^\mu G_a^\nu - \partial^\nu G_a^\mu)(\partial_\mu G_\nu^a - \partial_\nu G_\mu^a) \\ & + \sum_f \bar{q}_f^i (i\gamma^\mu \partial_\mu - m_f) q_f^i \\ & + g_s G_a^\mu \sum_f \bar{q}_f^a \gamma_\mu \left(\frac{\lambda^a}{2} \right)_{\alpha\beta} q_f^\beta \\ & - \frac{g_s}{2} f^{abc} (\partial^\mu G_a^\nu - \partial^\nu G_a^\mu) G_\mu^b G_\nu^c - \\ & - \frac{g_s^2}{4} f^{abc} f_{ade} G_b^\mu G_c^\nu G_\mu^d G_\nu^e \end{aligned} \quad (1.6)$$

The first two lines contain the kinetic terms for the gluon and quark fields; the third line, which involves the $SU(3)_C$ matrices λ^a , describes the interaction of quarks with gluons, in which the quark changes its color. The last two lines describe the self interaction of three and four gluons. The important property of the Lagrange density, and therefore of Quantum Chromodynamics, is that all contributions in Eq. 1.6 use the same coupling g_s . Alternatively the strong coupling constant $\alpha_s = \frac{g_s^2}{4\pi}$ can be used. Since the value of α_s depends on the energy μ , at which the coupling is observed, it is called "running coupling".

1.4 Charm quark pair production in hadron-hadron collision

An interaction of two hadrons at sufficiently high energy can be described as an interaction of two partons inside the hadrons [2]. Such processes can be calculated with perturbative quantum chromodynamics, if the momentum transfer is high enough, or if the products are heavy enough.

Figure 1.1 shows an interaction of two hadrons with momenta P_1 and P_2 . We interpret the

collision as the interaction of two partons, which carry parts of the hadron's momentum, x_1 and x_2 . The cross section for the production of a quark-antiquark pair is derived by convoluting the parton distribution function (PDF) with the cross section for the interaction between the two partons [1]

$$d^3\sigma = \sum_{i,j} \int dx_1 dx_2 d^3\bar{\sigma}_{ij}(x_1 P_1, x_2 P_2, k, \bar{k}, m, \mu) F_i^1(x_1, \mu) F_j^2(x_2, \mu) \quad (1.7)$$

where μ is the scale for calculating the strong coupling constant $\alpha_s(\mu)$, which in this case is of the order of magnitude of the quark mass m . k and \bar{k} are the momenta of the produced quark and anti quark, F_i are the parton distribution functions within the hadron, evaluated at the scale μ . $\bar{\sigma}_{ij}$ is the cross section for the quark production in the parton-parton interaction. The sum runs over all types of initial partons.

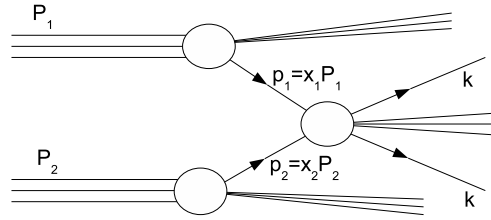


Figure 1.1: Interaction of two partons within hadrons

In the limit of heavy quarks ($\mu \gg \Lambda_{QCD}$), the interaction can be described with a first order perturbation. This is valid for the t quark and approximately valid for the b quark. The c quark is not heavy enough and in addition higher order corrections have to be taken into account.

The process of quark production can be divided into three steps:

- The partons before interaction, usually described with the parton distribution function
- The interaction itself
- Hadronization (factorization) of the produced quarks

1.5 The parton distribution function

The first part of the interaction process can be described with the parton distribution functions of the hadrons. PDFs are independent of the type of interaction and depend only on the type of the hadron and the parton. The parton distribution functions have to be determined experimentally and can be used in every process governed by the strong force. PDFs for valence and sea quarks as well as for gluons inside a proton are shown in Fig. 1.2 We can see that, for high momentum

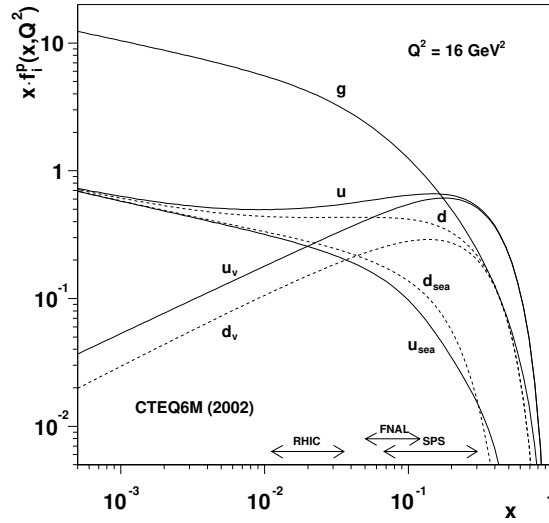


Figure 1.2: PDF of quarks and gluons within a proton [7]

fractions $x = p_{\text{parton}}/p_{\text{nucleon}}$, it is more likely to find quarks within a proton, while for small values the probability to find gluons is higher. It can also be seen, that the distributions of valence u and d quarks are different.

1.6 Interaction

At the tree level only two processes contribute in the scattering of partons, the quark-antiquark ($q\bar{q}$) annihilation and gluon-gluon (gg) fusion. In Fig. 1.3 the contribution of the gg fusion to the total cross section is shown; the remaining contribution to the cross section coming from the $q\bar{q}$ annihilation. It can be seen that the contribution of gluon-gluon fusion rises from about 50% at low energies to about 90% at $\sqrt{s} > 80$ GeV. At HERA-B energies ($\sqrt{s} = 41.6$ GeV) the contribution of gluon-gluon fusion is $\sim 80\%$.

After the phase space integration of Eq. 1.7 we obtain

$$\sigma(s) = \sum_{i,j} \int dx_1 dx_2 \bar{\sigma}_{i,j}(x_1 x_2 s, m^2, \mu^2) F_i^1(x_1, \mu) F_j^2(x_2, \mu) \quad (1.8)$$

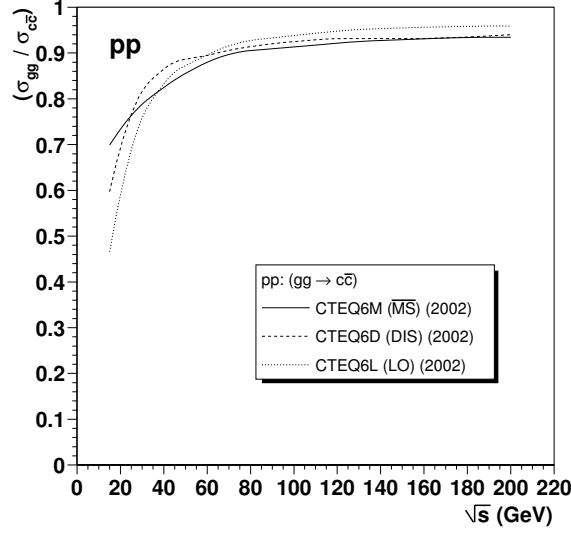


Figure 1.3: Contribution of gg fusion to the total cross section [7]

where s is the square of the hadron energy in the initial state measured in their center-of-mass system. The cross section for the interaction of partons can be written as

$$\bar{\sigma}_{ij} = \frac{\alpha_s^2(\mu^2)}{m^2} f_{ij}\left(\rho, \frac{\mu^2}{m^2}\right) \quad (1.9)$$

with $\rho = \frac{4m^2}{\bar{s}}$ and \bar{s} the square of the energy in the center-of-mass system of the partons and the function f_{ij} can be written as a perturbation series for α_s

$$f_{ij}\left(\rho, \frac{\mu^2}{m^2}\right) = f_{ij}^{(0)}(\rho) + g_s^2(\mu^2) \left[f_{ij}^{(1)}(\rho) + \bar{f}_{ij}^{(1)}(\rho) \log\left(\frac{\mu^2}{m^2}\right) \right] + \mathcal{O}(g_s^4) \quad (1.10)$$

with $g_s^2(\mu) = 4\pi\alpha_s(\mu)$.

At the tree level, taking into account only the Feynman diagrams shown in Fig. 1.4, the calculation of the functions f_{ij} gives [3]:

$$f_{q\bar{q}}^{(0)}(\rho) = \frac{\pi\beta\rho}{27}(2 + \rho) \quad (1.11)$$

$$f_{g\bar{g}}^{(0)}(\rho) = \frac{\pi\beta\rho}{192} \left(\frac{1}{\beta}(\rho^2 + 16\rho + 16) \ln\left(\frac{1+\beta}{1-\beta}\right) - 28 - 31\rho \right) \quad (1.12)$$

$$f_{g\bar{q}}^{(0)}(\rho) = f_{q\bar{g}}^{(0)}(\rho) = 0 \quad (1.13)$$

with $\beta = \sqrt{1 - \rho}$ and $\rho = 4m^2/\bar{s}$.

Higher order contributions usually contain loops with infinite contributions (Ultraviolet divergencies). By using Feynman rules we can write the contribution of the self energy of the

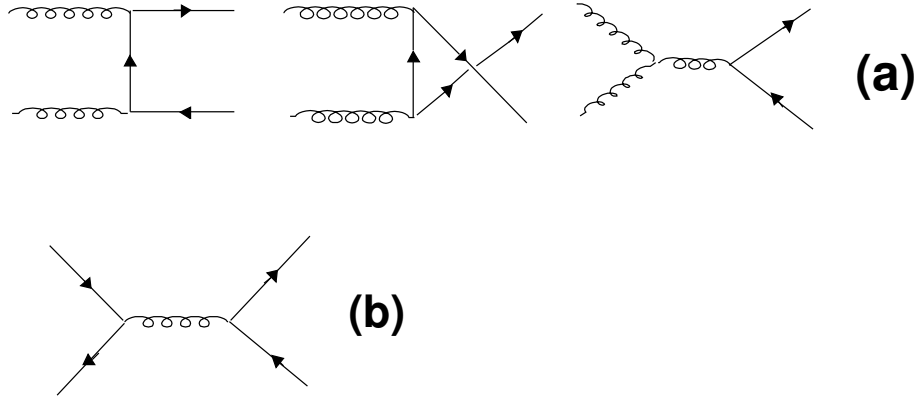


Figure 1.4: The Feynman diagrams at tree level. Diagram (a) shows the production of a quark-antiquark pair from gluon-gluon fusion and diagram (b) shows the production through quark-antiquark annihilation.

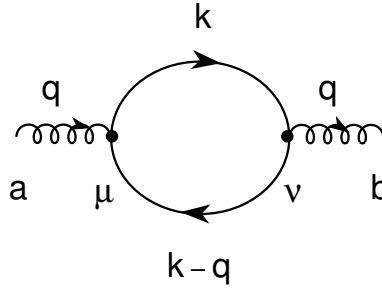


Figure 1.5: Feynman graph for the gluon self energy

gluon shown in Fig. 1.5 in the Dirac notation:

$$i\Pi_{ab}^{\mu\nu} = -g_s^2 \delta_{ab} \frac{1}{2} \int \frac{d^4 k}{(2\pi)^4} \frac{\text{Tr}[\gamma^\mu \not{k} \gamma^\nu (\not{k} - \not{q})]}{k^2 (k - q)^2} \quad (1.14)$$

Since we have two $q\bar{q}g$ -vertices, the result is proportional to g_s^2 .

The integration over k is divergent. Several techniques exist to avoid infinities. One possibility is to apply a cut-off in the integration over loop momenta at some large but finite momentum Λ . After finishing the calculation, one takes the limit $\Lambda \rightarrow \infty$, as the result should not depend on Λ . Another possibility is dimensional regulation, where the calculation is performed in $D = 4 + 2\epsilon$ dimensions and after the calculation ϵ is taken to 0. The results are independent of the procedure and finite [8].

Using dimensional regulation, the contribution of the loop in Fig. 1.5 can be written as

$$\Pi_{ab}^{\mu\nu} = \delta_{ab} (-q^2 g^{\mu\nu} + q^\mu q^\nu \Pi(q^2)) \quad (1.15)$$

with

$$\Pi(q^2) = -\frac{4}{6}\left(\frac{g_s\mu^\epsilon}{4\pi}\right)^2\left(\frac{1}{\epsilon} + \gamma_E - \ln(4\pi) + \ln(-q^2/\mu^2) - \frac{5}{3} + O(\epsilon)\right) \quad (1.16)$$

where $\gamma_E = 0.577251$.

If we know the value $\Pi(q^2)$ for the reference scale, the result can be generalized to an arbitrary scale by:

$$\Pi(q^2) = \Pi(q_0^2) - \frac{4}{6}(g_s/4\pi)^2 \ln(q^2/q_0^2) \quad (1.17)$$

The contribution of the loop can be divided into two parts:

$$\Pi(q^2) = \Delta\Pi_\epsilon(\mu^2) + \Pi_R(q^2/\mu^2) \quad (1.18)$$

The first term represents the infinite part, while the second term is finite. Different schemes are used to split Eq. 1.16 into finite and infinite terms. The most common schemes are:

μ -scheme:

$$\begin{aligned} \Delta\Pi_\epsilon(\mu^2) &= -\frac{g_s^2}{12\pi^2}\mu^{2\epsilon}\left[1/\epsilon + \gamma_E - \ln(4\pi) - \frac{5}{3}\right] \\ \Pi_R(q^2/\mu^2) &= -\frac{g_s^2}{12\pi^2}\mu^{2\epsilon} \ln(-q^2/\mu^2) \end{aligned} \quad (1.19)$$

MS -scheme:

$$\begin{aligned} \Delta\Pi_\epsilon(\mu^2) &= -\frac{g_s^2}{12\pi^2}\mu^{2\epsilon}[1/\epsilon] \\ \Pi_R(q^2/\mu^2) &= -\frac{g_s^2}{12\pi^2}\mu^{2\epsilon}[\ln(-q^2/\mu^2) + \gamma_E - \ln(4\pi) - \frac{5}{3}] \end{aligned} \quad (1.20)$$

\overline{MS} -scheme:

$$\begin{aligned} \Delta\Pi_\epsilon(\mu^2) &= -\frac{g_s^2}{12\pi^2}\mu^{2\epsilon}[1/\epsilon + \gamma_E - \ln(4\pi)] \\ \Pi_R(q^2/\mu^2) &= -\frac{g_s^2}{12\pi^2}\mu^{2\epsilon}[\ln(q^2/\mu^2) - \frac{5}{3}] \end{aligned} \quad (1.21)$$

In the μ scheme, one uses the value of $\Pi(-\mu^2)$ to define the divergent part. MS and \overline{MS} stand for "minimal subtraction" and "modified minimal subtraction" schemes. In the MS case, one subtracts only the divergent term, while in the \overline{MS} the divergent part is constructed from the divergent term $1/\epsilon$ and the constant factor $\gamma_E - \ln(4\pi)$.

A quantum field theory is renormalizable, if the ultraviolet divergences can be absorbed in a redefinition of the strong coupling constant α_s , which becomes a function of the energy μ at which the processes take place.

The way, how the coupling constant depends on the scale, is given by the renormalization group equation [6]:

$$\mu \frac{d\alpha_s}{d\mu} = \alpha_s \beta(\alpha_s) \quad (1.22)$$

$$\beta(\alpha_s) = \beta_1 \frac{\alpha_s}{\pi} + \beta_2 \left(\frac{\alpha_s}{\pi}\right)^2 + \dots \quad (1.23)$$

The expressions for β_i depend on the selected scheme. One loop calculations, using diagrams with fermions, gluons and ghosts[†] in the loop (Fig. 1.6), give:

$$\beta(\alpha_s) = \beta_1 \frac{\alpha_s}{\pi} \quad (1.24)$$

$$\beta_1 = \frac{2}{6} N_f - \frac{11}{6} N_C \quad (1.25)$$

where N_f is the number of quark flavors and N_C is the number of colors. The first term in

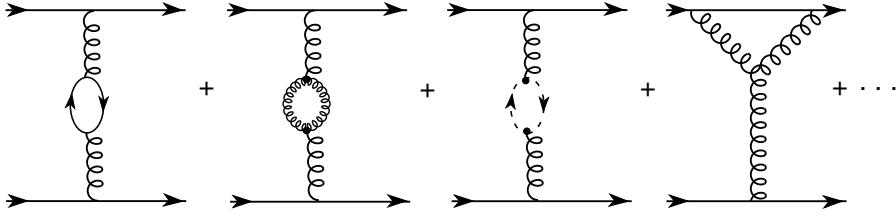


Figure 1.6: Some Feynman graphs used for the renormalization of the strong coupling constant. On the histograms, from left to right, the contributions of a fermion loop, a gluon loop, a ghost loop and the self interaction of three gluons is shown.

Eq. 1.25 comes from the loops of type $q\bar{q}$ and is similar to contributions obtained in quantum electrodynamics. The second term follows from of the self interaction of gluons and, since $N_f \leq 6$ causes, that $\beta_1 < 0$ and is therefore responsible for the asymptotic freedom of quarks in quantum chromodynamics ($\alpha_s(Q^2) \rightarrow 0$ if $Q^2 \rightarrow 0$).

By solving Eq. 1.22 we can write the result for one loop [6]:

$$\alpha_s(\mu^2) = \frac{2\pi}{-\beta_1 \ln\left(\frac{\mu^2}{\Lambda_{QCD}^2}\right)} \quad (1.26)$$

where the integration constant Λ_{QCD} is given by the expression

$$\ln(\Lambda_{QCD}) = \ln \mu_R + \frac{\pi}{\beta_1 \alpha_s(\mu_R^2)} \quad (1.27)$$

and μ_R is the renormalization scale.

[†]The covariant gluon propagator contains also unphysical scalar and longitudinal polarization components, which are canceled by adding additional unphysical ghost fields with an appropriate coupling to gluons [9].

The β functions are known to four loops and its coefficients in the \overline{MS} scheme (using $\varsigma_3 = 1.202056903$) are [6]

$$\beta_2 = -\frac{51}{4} + \frac{19}{12}N_f \quad (1.28)$$

$$\beta_3 = \frac{1}{64}[-2857 + \frac{5033}{9}N_f - \frac{325}{27}N_f^2] \quad (1.29)$$

$$\begin{aligned} \beta_4 = & -\frac{1}{128}[(\frac{149753}{6} + 3564\varsigma_3) - (\frac{1078361}{162} + \frac{6508}{27}\varsigma_3)N_f \\ & + (\frac{50065}{162} + \frac{6472}{81}\varsigma_3)N_f^2 + \frac{1093}{729}N_f^3]. \end{aligned} \quad (1.30)$$

$\beta_2 < 0$ for $N_f \leq 8$, $\beta_3 < 0$ for $N_f \leq 5$, β_4 is always negative and higher order corrections enhance the effect of asymptotic freedom of quarks in the quantum chromodynamics.

Infrared divergences arise if in the final state a gluon is nearly collinear with a produced quark or antiquark, or if the momentum of the emitted gluon is small. Similarly, as for ultraviolet divergences by redefining the coupling constant, one can avoid infrared divergences by redefining the parton distribution functions, which also become functions of the momentum transfer. If we are able to determine (to measure) the PDF $F_i^a(x_a, \mu_F)$ at the reference scale, then we can calculate its value for an arbitrary scale. This process introduces the factorization scale, μ_F . The renormalization scale μ_R and the factorization scale μ_F are different in general, hence we can write Eq. 1.8 and Eq. 1.9 in the form:

$$\sigma(s) = \sum_{i,j} \int dx_1 dx_2 \bar{\sigma}(x_1 x_2 s, m^2, \mu_R, \mu_F) F_i^1(x_1, \mu_F) F_j^2(x_2, \mu_F) \quad (1.31)$$

$$\bar{\sigma}_{ij} = \frac{\alpha_s^2(\mu_R^2)}{m^2} f_{ij}(\rho, \mu_F^2, \mu_R^2, m^2) \quad (1.32)$$

1.7 Hadronization

After their production the quarks have to bind with other quarks to form color singlets. The interaction field behaves like a tube, that stretches between the quarks, while the energy density along the tube is constant. The potential therefore increases linearly with the separation of the quarks. At some point a new quark-antiquark pair is created to lower the potential energy. In the Lund string fragmentation model [10] the probability for the produced quark flavor depends on the quark mass and is $u : d : s : c \sim 1 : 1 : 0.3 : 10^{-11}$. From these numbers it can be seen that light quark production during the hadronization is strongly favored. Heavy quark pairs are mostly produced at the primary interaction and rarely in the factorization process. The production of additional quark pairs continues as long as the available energy is sufficiently large.

The initial hadrons play an additional role. Since they lose a colored parton in the interaction, they also become colored and therefore they must contribute in the production of new

quark-antiquark pairs in the fragmentation. This is the reason why the process also depends on the type of the interacting particles.

The probabilities for the c quarks to form specific D mesons were measured at e^+e^- colliders [11]. The probability for D^0 is 57%, for D^+ it is 25% and 8% for D_s ; the rest is going into charmed baryons. The large difference between the probability for the neutral and the charged charmed meson production can be explained using a simple model [1]: D^0 and D^+ are pseudo scalar mesons; their spin is $S = 0$. They are produced either directly, by fragmentation of the c quark, or through a feed-down of charmed vector mesons, mainly the neutral D^{*0} (2007) and the charged meson D^{*+} (2010).

The ratio can be written in the form:

$$R = \frac{\sigma_{D^+}}{\sigma_{D^0}} = \frac{\sigma_{D^+}^d + \sigma_{D^{*0}}^d \cdot BR(D^{*0} \rightarrow D^+) + \sigma_{D^{*+}}^d \cdot BR(D^{*+} \rightarrow D^+)}{\sigma_{D^0}^d + \sigma_{D^{*0}}^d \cdot BR(D^{*0} \rightarrow D^0) + \sigma_{D^{*+}}^d \cdot BR(D^{*+} \rightarrow D^0)} \quad (1.33)$$

where $\sigma_{D^i}^d$, $i = +, 0, *+, *0$ is the direct cross section for the production of the meson D^i and $BR(D^{*a} \rightarrow D^b)$ with $a, b = +, 0$ being the probability that the meson D^{*a} will decay into particles with a meson D^b in its final state .

With the use of Clebbsh-Gordon coefficients or the use of measured branching ratios from [11], one can find that for a D^{*+} (2010) the decay $D^{*+} \rightarrow D^0\pi^+$ is twice as likely, as the decay $D^{*+} \rightarrow D^+\pi^0$, while the neutral vector meson D^{*0} (2007) decays with a probability of nearly 100% into the two neutral particles $D^0\pi^0$. The reason for the latter is that the invariant mass of the second charge-conserving combination, $D^+\pi^-$, is higher than the invariant mass of the vector particle D^{*0} (2007) and therefore the phase space for such a decay is zero.

Due to the three possible spin polarizations of vector particles, about three times more vector particles than scalars could be expected, if the masses of scalar and vector mesons were equal. The measured fraction of vector mesons, P_V , created in e^+e^- collisions, is 0.6, probably due to the higher masses of vector mesons. Assuming isospin invariance, one expects the same number of charged and neutral particles to be produced in the fragmentation process. With the measured value, $P_V = 0.6$, and the assumption of isospin invariance, the ratio determined from Eq. 1.33 is:

$$R = \frac{\sigma_{D^+}}{\sigma_{D^0}} = \frac{0.4 + 0.6 \cdot (0 + 0.322)}{0.4 + 0.6 \cdot (1 + 0.677)} = 0.42 \quad (1.34)$$

This simplified model predicts a 2.5 times higher production cross section for D^0 compared to the production cross section of the D^+ . The world average measured in e^+e^- collisions is $R = 0.44 \pm 0.04$ [11]

1.8 Existing experimental data

In the past twenty years, measurements from several experiments on open charm production cross sections in proton nucleus collisions, covering the proton energy range from 250 GeV

to 800 GeV were published. The experiments are summarized in Table 1.1. A more detailed overview is given in [4]. With only one exception (E789), these experiments covered the full forward hemisphere in the phase space, but the number of collected D mesons is rather low.

The kinematics of the produced D mesons is determined by the two dimensional distribution in the momentum space $d^2\sigma/\pi dp_T^2 dx_F$, given in the center-of-mass system (CMS) of the collisions; p_T and x_F are the transverse and the normalized longitudinal momentum coordinates. The normalized longitudinal momentum x_F (Feynman's x variable) is defined as $x_F = 2p_z/\sqrt{s}$, where p_z is longitudinal momentum and \sqrt{s} the total energy of the collision, both given in the CMS.

Exp.	Target	Beam E_{lab} [GeV]	Phase space coverage	Events	
				D^0	D^+
E769 [12]	Be,Al,Cu,W	250	$x_F > -0.1$	136	159
NA16 [13]	liquid H ₂	360	$x_F > -0.1$	5	10
NA27 [14]	liquid H ₂	400	$x_F > -0.1$	98	119
E743 [15]	liquid H ₂	800	$x_F > -0.1$	10	46
E653 [16]	emulsion	800	$x_F > -0.1$	108	18
E789 [17]	Be, Au	800	$0 < x_F < 0.08, p_T < 1.1 \text{ GeV}/c$	>4000	

Table 1.1: Experiments measuring the production cross sections of neutral and charged D mesons in pA interactions. The table is taken from [4]

Experiments NA16, NA27 and E743 [13] [14] [15] used the high resolution hydrogen bubble chamber (LEBC) as a target and vertexing device, while tracking, momentum measurement and particle identification utilized a 40 meter long ‘‘EHS’’ spectrometer. They used a simple interaction trigger, provided by wire chambers placed just downstream of the LEBC. The charm mesons were identified by their topology (displaced vertex), by observing the charge of the decaying particle and a given number of charged final state particles.

Experiment E653 [16] used a 1.47 cm long emulsion target followed by an 18-plane silicon vertex detector continued by a magnetic spectrometer. The trigger required an interaction in the target and a high p_T muon candidate, detected in the muon spectrometer. Cross sections were obtained essentially on the basis of semi-muonic decays.

Experiment E769 [12] used a multifoil target, consisting of 250 μm thick Be, Al and Cu foils, as well as 100 μm thick W foils, spaced by 1.6 mm. In total, 26 target foils were used. The detector included an 11-plane silicon vertex detector, two analyzing magnets, drift and multiwire proportional chambers for tracking, a segmented threshold Cherenkov counter for pion, kaon and proton identification, electromagnetic and hadron calorimeters and a muon identification

system. The trigger required the total transverse energy in the calorimeters to exceed 5.5 GeV. The charm mesons were identified in fully reconstructed decays to two or three charged final state particles. This experiment is the only one which measured D_s and Λ_c production in pA collisions, but was able only to give confidence intervals for the cross section.

Experiment E789 [17] used a thin strip target of Be or Au, 160 μm by 1.8 mm or 110 μm by 0.8 mm in cross section, and a 16-plane silicon vertex detector to measure the secondary vertices of D mesons. An on-line vertex processor selected events with secondary vertices at least 1.02 mm downstream of the target. The decay products were further analyzed by a spectrometer consisting of two magnets and tracking chambers, a ring-imaging Cherenkov detector, electromagnetic and hadronic calorimeters and a muon identification system. This experiment collected the largest open charm data sample, but measured only neutral D mesons. Unfortunately, their coverage of the phase space is rather small, causing a significant systematic uncertainty, when extrapolated to the full phase space, since the extrapolation is model dependent. E789 is the only experiment which measured the nuclear dependence of the D meson production. Their result, $\alpha = 1.02 \pm 0.03 \pm 0.02$, justifies the assumption of linear dependence of the production cross section on the atomic number of the target.

The experiments from Table 1.1 published D meson cross sections for proton-nucleon collisions, assuming a linear dependence on target atomic number A : $\sigma_{pA} = \sigma_{pN} \cdot A$. Their results, scaled where necessary to the full phase space and corrected for the present values of the branching ratios, are summarized in Table 1.2.

Exp.	Beam E_{lab} [GeV]	$\sigma_{pN}(D^0)$ [μb]	$\sigma_{pN}(D^+)$ [μb]	$\sigma_{pN}(D^{*+})$ [μb]	$\sigma_{pN}(D_s^+)$ [μb]
E769 [12]	250	$12.0 \pm 2.7 \pm 1.1$	$6.6 \pm 0.8 \pm 0.6$	$3.8 \pm 1.3 \pm 0.4$	$> 1.0 ; < 5.2$
NA16 [13]	360	$20.4^{+15.8}_{-8.6}$	$10.6^{+4.8}_{-3.2}$		
NA27 [14]	400	18.3 ± 2.5	11.9 ± 1.5	9.2 ± 2.4	
E743 [15]	800	$22^{+9}_{-7} \pm 5$	$26 \pm 4 \pm 6$		
E653 [16]	800	$43 \pm 3 \pm 12$	$31 \pm 9 \pm 13$		
E789 [17]	800	$17.0 \pm 0.9 \pm 3.3$			

Table 1.2: Existing data for D meson total production cross sections in pA collisions for proton energies from 250 to 800 GeV.

These measurements can be compared to the leading order (LO) predictions generated by PYTHIA [4]. The calculations include LO diagrams presented in Fig. 1.4 as well as initial and final state radiation. In the absence of higher-order diagrams the resulting cross sections are too low (Fig. 1.7). The missing contributions are expressed by scaling the result with empirical K -factors, which can be used under the hypothesis, that the shapes of kinematical distributions are not affected much by higher order corrections. Values for K -factors are, depending on

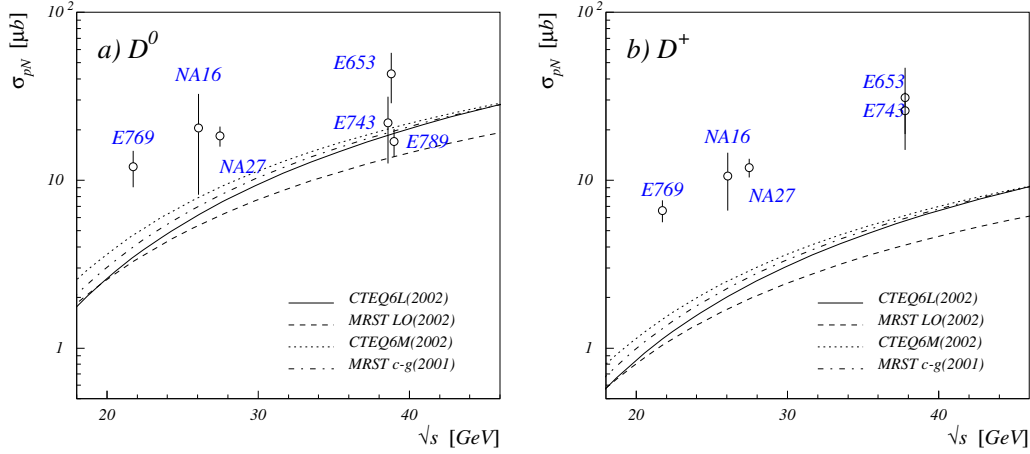


Figure 1.7: A comparison of PYTHIA predictions using different PDF's with the measured production cross sections for a) D^0 , b) D^+

the selected PDF, between 2.0 and 3.6 for the D^0 and between 4.2 and 7.4 for the D^+ [4]. A calculation of radiative corrections [18] shows, that the shapes of the differential distributions predicted by the leading order calculation are appreciably not altered. For charm hadroproduction the errors of such calculations are large and hard to estimate because of the smallness of the charm quark mass.

To obtain the estimates for the charm cross sections at the HERA-B energy, which are needed for the “blind” optimization of our analysis cuts, we fitted the data points from Table 1.2. We found a simple parameterization based on the fits to LO predictions for the energy dependence of the cross section in [7]:

$$\sigma(\sqrt{s}) = p_0 \cdot \left(1 - \frac{p_1}{\sqrt{s}^{p_3}}\right)^{p_2} \quad (1.35)$$

with $p_1 = 1.2$, $p_2 = 12$ and $p_3 = 0.35$ and only p_0 being free. Fig. 1.8 shows the charm data points together with results of the fits. Eq. 1.35 fits the D^+ and D^{*+} experimental data well, while for the D^0 the data point of E789 had to be excluded in order to get a good fit. [‡] The cross sections extrapolated to the HERA proton energy are summarized in Table 1.3.

$\sigma_{pN} [\mu\text{b}]$		
D^0	D^+	D^{*+}
45	31	21

Table 1.3: Cross sections extrapolated to 920 GeV

Most of the experiments published also measurements of kinematical distributions in x_F

[‡]One of the reasons for this discrepancy could be an underestimated systematic error due to the extrapolation from the very limited measured part of the phase space to the full phase space as required in the E789 experiment.

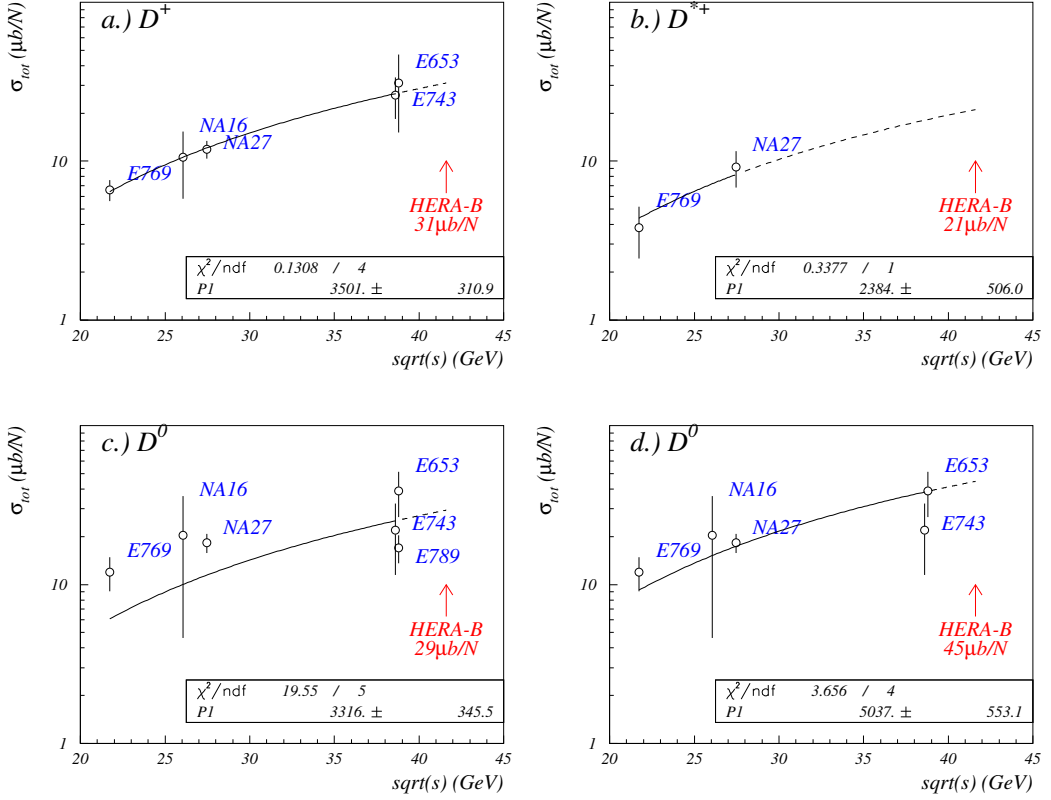


Figure 1.8: Energy dependence of the cross section for a) D^+ , b) D^{*+} , c) D^0 and d) D^0 with the E789 data point excluded from the fit

and p_T . They typically used the parameterization

$$\frac{d^2N}{dx_F dp_T^2} \propto (1 - |x_F|)^n e^{-bp_T^2} \quad (1.36)$$

with the two free parameters n and b describing the shapes in x_F and p_T projections of the 2D distribution respectively. Since one could expect some energy dependence of the shapes, we summarize in Table 1.4 only the results of the three experiments at 800 GeV, closest to HERA-B energy. The p_T range of these experiments is relatively small. As one can see from their published distributions, shown in Fig. 1.9, the limitation for the first two experiments is due to low statistics. For completeness we also show in Fig. 1.10 the published x_F distributions of E653 and E743.

The p_T^2 distribution with the highest statistics was collected by the E769 experiment at 250 GeV, covering the range of $p_T^2 < 10$ (GeV/c) 2 . They found that the simple exponential in Eq. 1.36 did not fit the measurement well and that the b parameter was sensitive to the fit range used. They tried a form, inspired by QCD, with two free parameters, α and β , and with a

Exp	events	effective range		n	b
E653 [16]	146	$-0.15 < x_F < 0.3$	$p_T^2 < 4$	$6.9^{+1.9}_{-1.8}$	$0.84^{+0.10}_{-0.08}$
E743 [15]	31	$-0.1 < x_F < 0.4$	$p_T^2 < 3.5$	8.6 ± 2.0	0.8 ± 0.2
E789 [17]	~ 2200	$0 < x_F < 0.08$	$p_T^2 < 1.2$		0.91 ± 0.12
Average				7.7 ± 1.4	0.86 ± 0.07

Table 1.4: Measurements of parameters n and b of Eq. 1.36 at 800 GeV

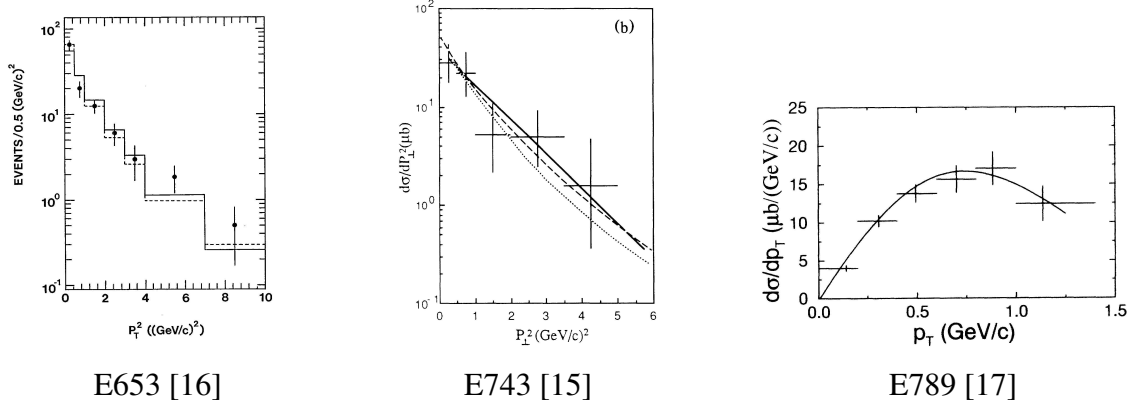


Figure 1.9: Published measurements of the p_T distributions at 800 GeV.

mass of $m_c = 1.5$ GeV:

$$\frac{dN}{dp_T^2} \propto (\alpha m_c^2 + p_t^2)^{-\beta} \quad (1.37)$$

and found it to fit their measured distribution well over the entire p_T range.

1.9 Other open charm analyses at HERA-B

Several open charm cross section measurements were performed on the data collected with the HERA-B experiment. D. Dujmić [19] analyzed a data sample collected in year 2000, which consisted of 4.4×10^6 single-lepton and di-lepton triggered events. He measured the total cross sections for the production of D^0 and D^+ mesons. P. Conde [20] used a similar data sample consisting of 5×10^6 events for the measurement of the production ratio of D^+ and D^0 mesons. A. Gorišek [21] analyzed a sample of 16.4×10^6 minimum bias events taken with the interaction trigger previously to the data samples used for the present analysis. He measured the D^0 and D^{*+} total production cross sections and the A-dependence parameter α . The results of these measurements are compatible with the present analysis, but the uncertainties are larger due to much smaller data samples.

A. Bogatyrev [22] did his analysis in parallel and independently to the analysis presented in this work. He analyzed the same data samples. His results are in agreement with the results of

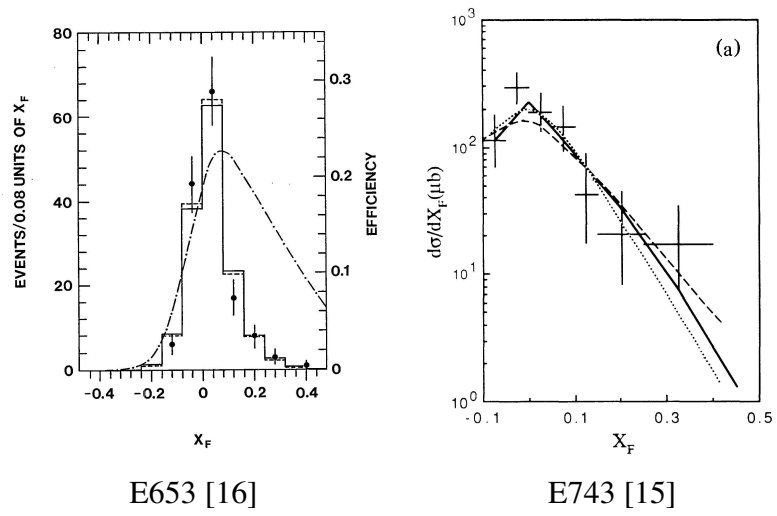


Figure 1.10: Published measurements of the x_F distributions at 800 GeV.

our analysis.

2 The HERA-B experiment

The HERA- B experiment was originally designed to measure the CP -violation in the system of neutral B mesons [23],[24]. The decay of interest is the "golden decay mode" of the neutral B -meson, in which the B^0 and its antiparticle decay into the same decay products: $B^0 \rightarrow J/\Psi K_S^0$ [25]

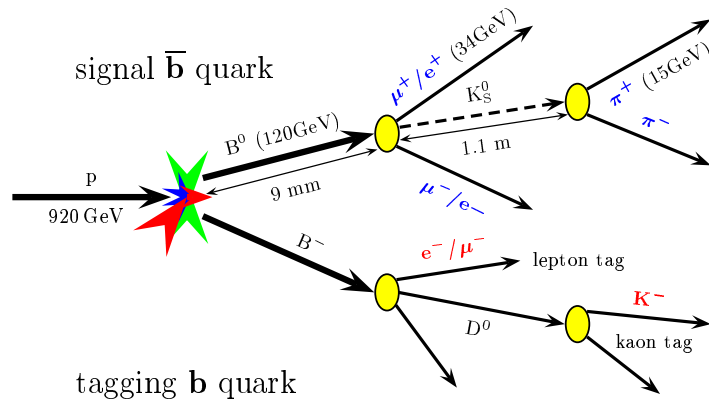


Figure 2.1: Schematic view of the *golden decay mode* $B^0 \rightarrow J/\Psi K_S^0$

The final state $J/\Psi K_S^0$ is a CP eigenstate. The J/Ψ decays immediately into two leptons with high transverse momenta, while the K_S^0 decays in most cases into two pions after traveling typically 1.1 m in the HERA-B lab frame. A scheme of the golden decay mode is shown in Fig. 2.1. Due to the relatively long lifetime of the neutral B meson, which corresponds to 11 mm in the HERA-B lab frame, the decay vertex is well separated from the primary interaction point and the J/Ψ can be distinguished from the large background of directly produced J/Ψ 's. Whether the neutral B meson was a particle or an antiparticle can be checked by determining the charge of the second produced B meson either through the charge of the lepton with a high transverse momentum (lepton tag) or the charge of the kaon (kaon tag) in the second B meson decay chain.

2.1 The HERA accelerator

The HERA Ring is a storage ring with a length of 6336 m. A scheme of the ring with its pre-accelerators is shown in Fig. 2.2. Two beams, one with protons at energies of 920 GeV and one with electrons at energies of 30 GeV, circulate in opposite directions and collide at two points used by the H1 and ZEUS collaboration. The HERMES experiment uses only the electron beam, which collides with a polarized target while HERA-B uses only the proton beam and a fixed target built from 8 wires of different materials. The target is positioned into the beam halo in order not to disturb the other experiments measuring $e - p$ collisions. The proton beam consists of 220 bunches with a length of 30 cm each, separated by about 3 meters. From the 220 bunches only 180 bunches are filled as the pre-accelerator has a capacity of 60 bunches.

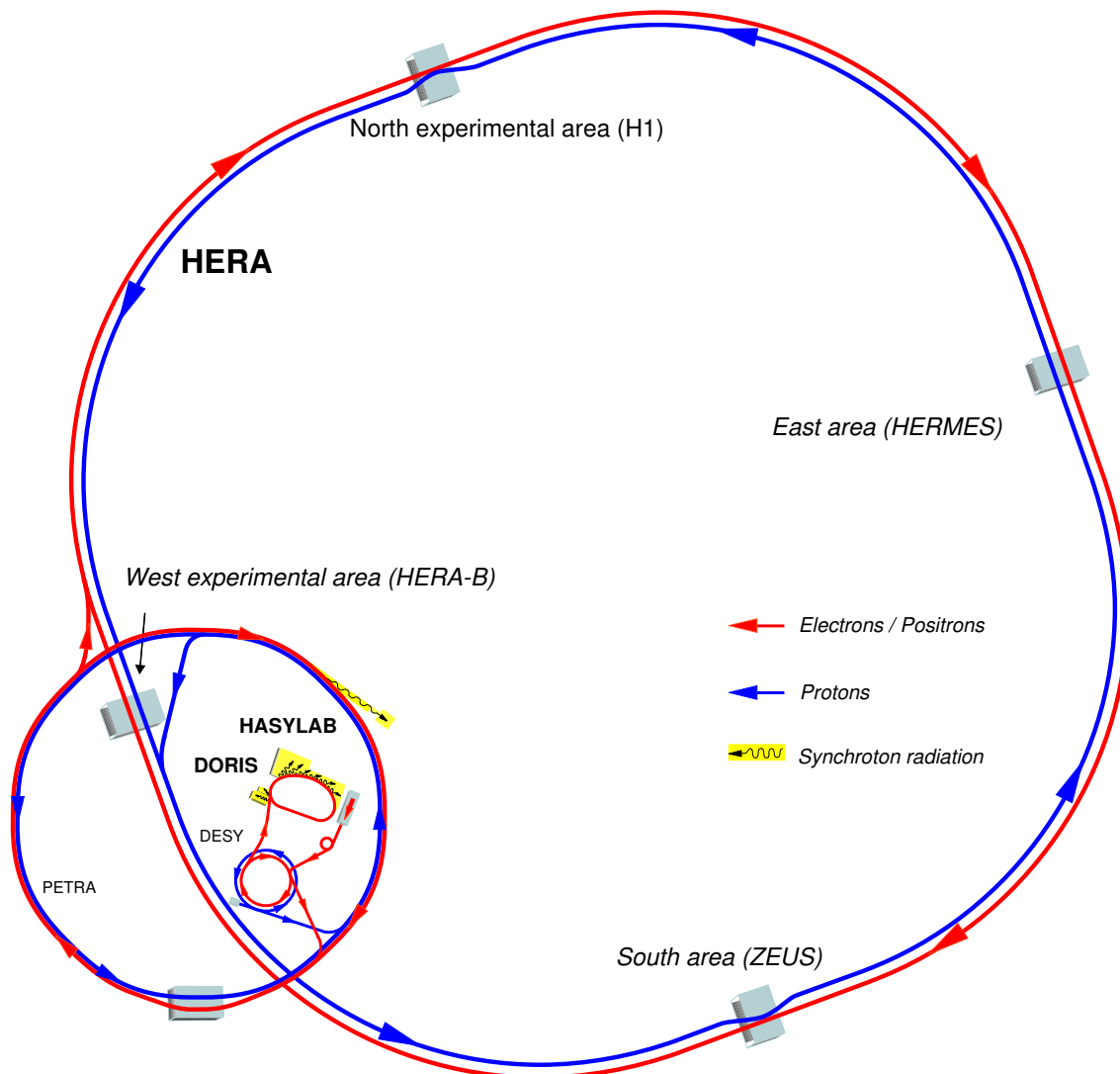


Figure 2.2: Schematic view of the Hera-B storage ring located at DESY, Hamburg

2.2 The HERA-B detector

The HERA-B detector is a forward spectrometer, covering an angle from 10 to 250 mrad in the bending plane of the magnet and an angle from 10 to 180 mrad in the non-bending plane. This configuration covers 90% of the solid angle in the center-of-mass system of the proton-nucleon collisions.

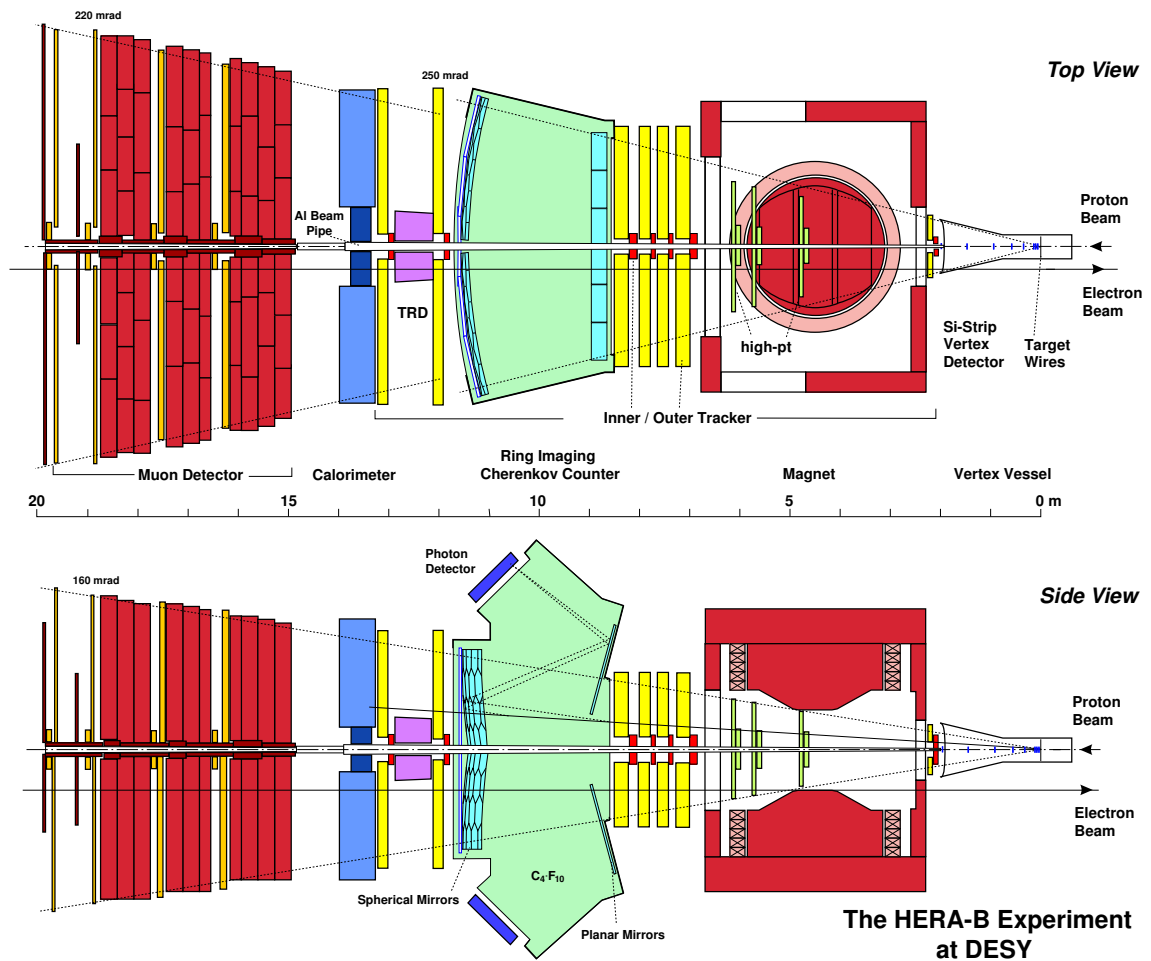


Figure 2.3: The Hera-B Detector

A schematic view of the detector is shown in Fig. 2.3. The components are divided into two groups: the tracking devices and the devices for particle identification. The first group consists of the vertex detector system (VDS) just downstream of the target, followed by the magnet and the inner (ITR) and outer tracker (OTR). The particle identification systems are the ring imaging Cherenkov counter (RICH), the electromagnetic calorimeter (ECAL) and the muon chambers (MUON). The length of the detector is approximately 20 m.

2.3 Target

The target [28] consists of 2 stations, separated by ~ 4.5 cm, with 4 wires each (Fig. 2.4). The wires are made from four different materials (C, W, Ti, Al), to allow measurements of the production cross section dependence on the atomic number of the target material. The tungsten and titanium wires have a diameter of $50 \mu\text{m}$, while the carbon wires are ribbons of the dimension $100 \mu\text{m} \times 500 \mu\text{m}$. The aluminum targets were not used in this analysis.

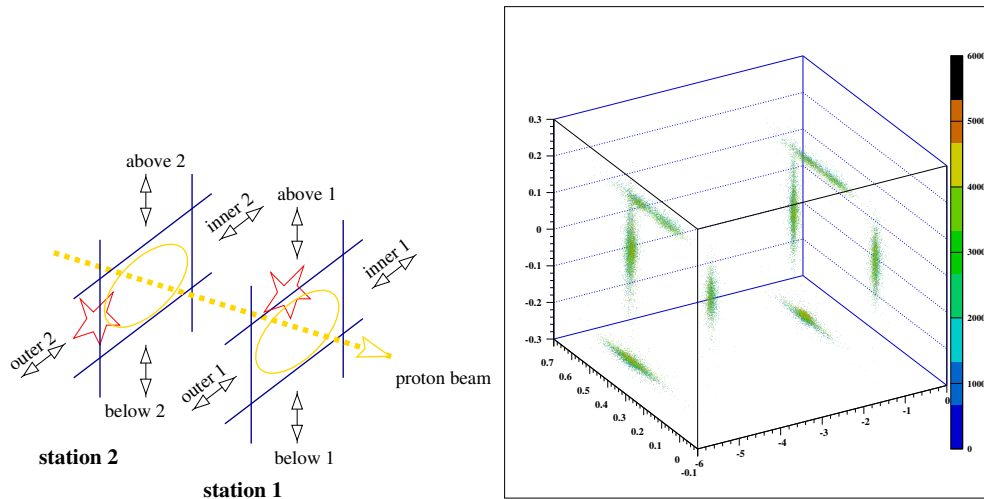


Figure 2.4: Schematic view of the eight target wires and reconstructed vertices inside the target wires around the proton beam

Each wire can be moved independently to adjust the interaction rate. The displacement of the two stations is large enough, for most of the heavy mesons produced in the first station to decay before reaching the second station, so the primary interaction point can be clearly defined.

2.4 Vertex detector

Tracks from proton interactions and decay vertices are measured with a vertex detector system (VDS) [29]. It consists of eight superlayers of silicon detectors (Fig. 2.5) that are arranged perpendicular to the beam axis. The layers are arranged between 7 cm and 100 cm downstream of the targets, covering an angular range from 10 to 250 mrad. A layer is composed of four modules forming four quadrants. Each module is equipped with two double sided microstrip detectors ($50 \times 79 \text{ mm}^2$, pitch of $50 \mu\text{m}$). The orthogonal strip pattern is rotated by $\pm 2.5^\circ$ in respect to the vertical axis. To minimize multiple scattering, the first seven superlayers are in roman pots under vacuum, while the last one is behind the exit window of the vessel. Their position could be adjusted within 10-15 mm from the beam center. The vertex resolution is $\sigma_z \sim 500 \mu\text{m}$ along the beam direction and $\sigma_{x,y} \sim 50 \mu\text{m}$ in the transverse plane.

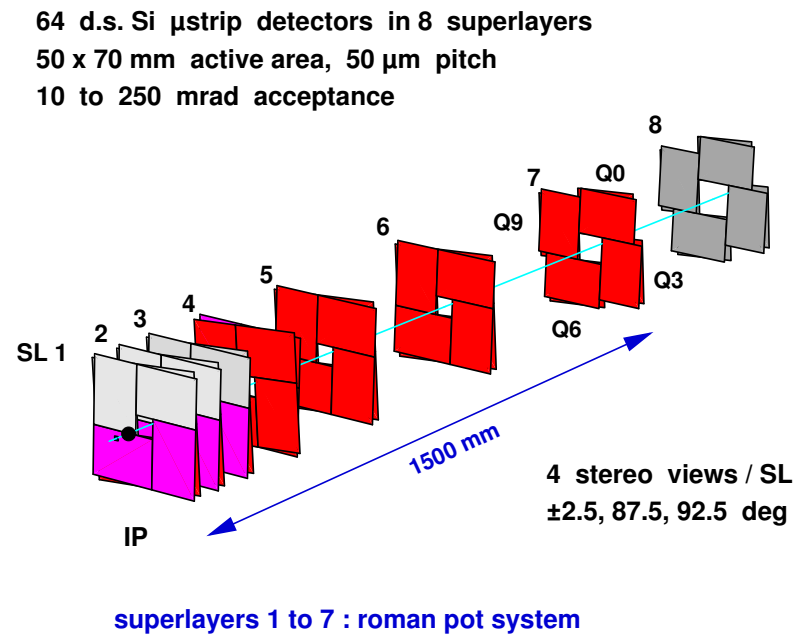


Figure 2.5: Scheme of the detector wafers in the VDS

2.5 Tracking system

Particle momenta are measured with a tracking system and a dipole magnet of 2.13 Tm field integral. The tracking system is divided into a fine grained inner tracker (ITR) [30] and a coarse grained outer tracker (OTR) [31]–[33]. The chambers are located up to 13 m downstream of the interaction region. Two chambers (magnet chambers – MC) are positioned in front of the magnet, four of them (pattern recognition chambers – PC) between the magnet and the ring imaging Cherenkov counter and two (trigger chambers – TC) between the RICH and the electromagnetic calorimeter. The TC and two of the PC are used by the di-lepton trigger. The momentum resolution is $\sigma_p/p = (1.61 + 0.0051p)\%$, with p expressed in GeV/ c .

2.5.1 Inner Tracker

The inner tracker (ITR) covers the innermost part of the detector from the beam pipe up to a radial distance of ~ 30 cm. It is composed of 184 microstrip gaseous chambers (MSGC) with gas electron multipliers (GEM) and with a strip pitch of ~ 300 μ m (Fig. 2.7). The GEM provides an electron multiplication of 15–50. Stereo layers (Fig. 2.6) of dimension 50×60 cm², oriented with angles 0° and $\pm 5^\circ$ in respect to the vertical axis, are grouped into 10 stations. The intrinsic spatial resolution of the ITR is 110 μ m. Due to differences in the response between Monte Carlo simulation and real data the ITR was not used in this analysis.

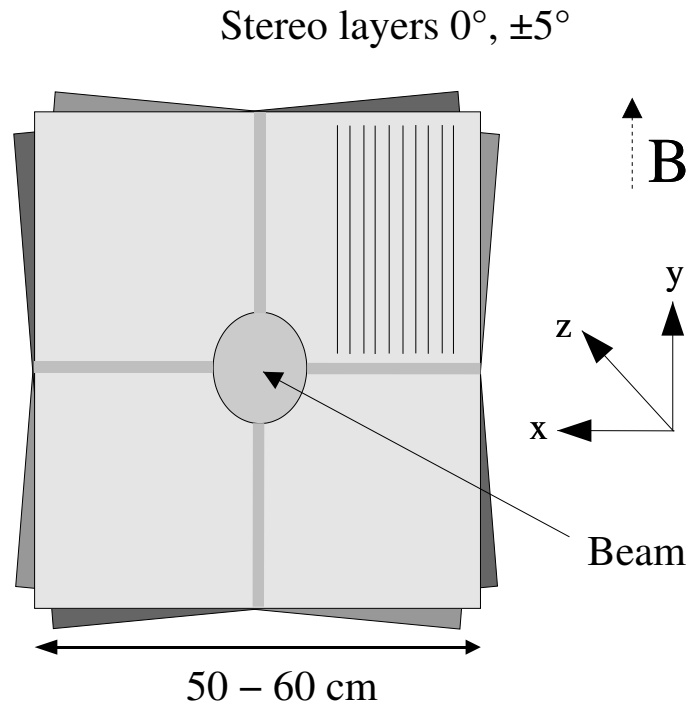


Figure 2.6: Geometry of the inner tracker stereo layers

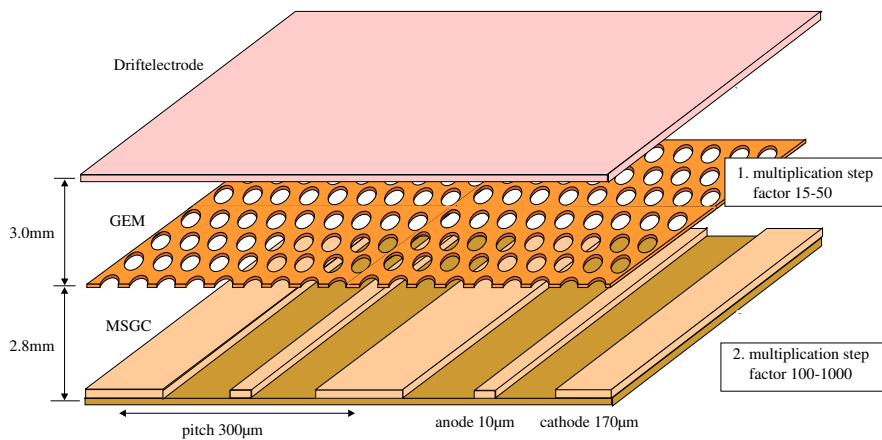


Figure 2.7: Schematic view of a microstrip gas chamber

2.5.2 Outer Tracker

The OTR covers the region from the outer acceptance limit of the detector (~ 250 mrad in the bending plane of the magnet, ~ 160 mrad in the non bending plane) down to a radial distance of 20 cm from the HERA proton beam. It consists of 8 superlayers, which are vertically divided into two independent chambers and twelve subsections (Fig. 2.8). A layer inside each chamber consists of honeycomb drift tube modules, shown in Fig. 2.9. The basic drift cell is a hexagonal

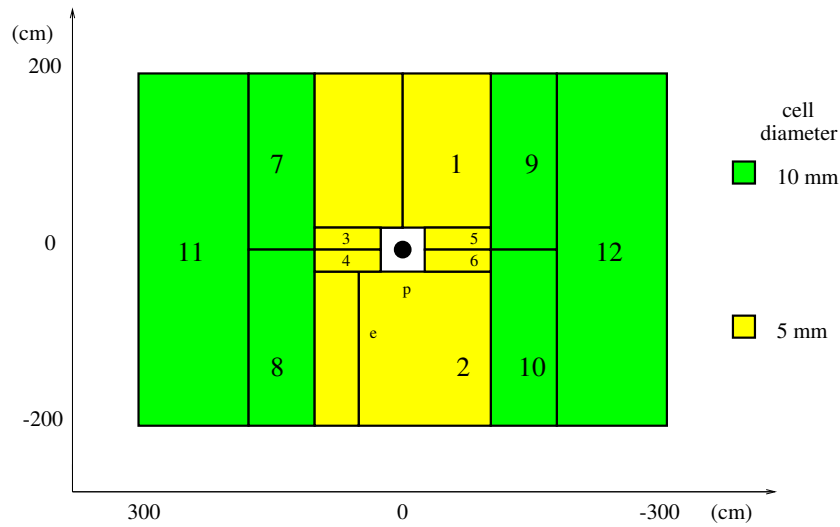


Figure 2.8: An OTR superlayer with its twelve subsections.

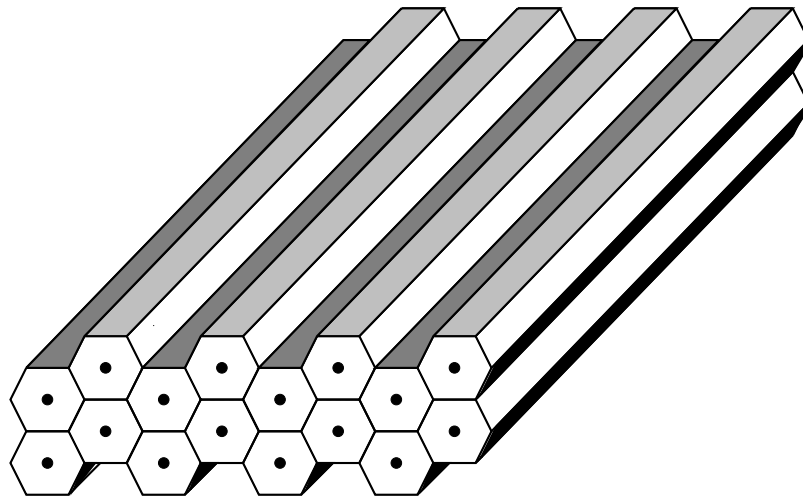


Figure 2.9: Schematic view of a honeycomb drift chamber

tube made of a conductive foil with a signal wire stretched along its center. The foil acts as the cathode. The wires are oriented with angles 0° and $\pm 5^\circ$ in respect to the vertical axis. The cell size varies from 5 mm in the inner part of the superlayer to 10 mm in the outer part to account for the different occupancy of these regions. The average hit efficiency is 94% for 5 mm cells and 97% for 10 mm cells, the hit resolution of the drift cells is $\sim 320 \mu\text{m}$.

2.6 Ring imaging Cherenkov detector

The ring imaging Cherenkov detector (RICH) [34] was designed to separate pions from kaons in the momentum interval from 5 to 50 GeV/c. A schematic view is presented in Fig 2.10. The RICH detector is a large vessel containing about 100 m^3 of C_4F_{10} gas at NTP, which provides

about 2 m of radiation path. Focusing of Cherenkov photons is achieved by two spherical mirrors with focal length of 5.7 m, tilted by 9° in opposite directions. Two planar mirrors then reflect the light to photon detectors at the top and bottom of the vessel.

Each photon detector consists of about 1100 multianode photomultiplier tubes (Hamamatsu R5900). The inner region is equipped with 16-channel and the outer region with 4-channel tubes. As the active area of a photomultiplier tube covers only about 23% of the tube's size a lens demagnifying system is placed in the front of each tube.

The Cherenkov angle for $\beta = 1$ particle is 52 mrad and the average number of photons per $\beta = 1$ particle is 33. The pion efficiency is about 90% in the momentum range up to 70 GeV/c with the kaon mis-identification probability below 10%, while the kaon efficiencies are above 85% for kaon momenta between 15 GeV/c and 45 GeV/c with the pion mis-identification of $\sim 1\%$. For kaons below Cherenkov threshold of ~ 10 GeV/c the mis-identification of pions is below 10%.

2.7 Electromagnetic calorimeter

The electromagnetic calorimeter (ECAL) [35] is used for the identification of electrons and positrons, and for the detection of γ photons. The ECAL is built as a matrix of 5956 calorimeter cell pads placed at about 13.5 m downstream the target wires (Fig. 2.11). The cell pads are squares of three different sizes in order to match the granularity requirements in different regions of the detector. They are built using shashlik technology as a sandwich of sampling plastic scintillators and tungsten (lead) absorbers (Fig. 2.12). The cell size in the outer region is 11.18×11.18 cm², in the middle region it is 5.59×5.59 cm², while in the inner region the size is 2.24×2.24 cm². The ECAL is organized in modules with a transverse segmentation of 25 cells. One such module in the inner region consists of 40 tungsten and scintillator layers and corresponds to a total thickness of 23 radiation lengths, while in the middle and outer region there are 37 layers with lead absorbers, corresponding to thickness of 20 radiation lengths. The energy deposited in the ECAL by a photon or an electron produces a scintillation light that is transformed into an electric current by photomultiplier readout tubes. Every cell employs its own PMT.

The energy resolution is different in the inner and outer regions and is $\sigma(E)/E = 17\%/\sqrt{E} \otimes 1.7\%$ in the inner region and $\sigma(E)/E = 10\%/\sqrt{E} \otimes 1\%$ in the outer regions (\otimes indicates sum in quadrature; E is expressed in GeV).

2.8 Muon chambers

The muon system [36] is able to detect muons in a momentum range starting from ~ 4.5 GeV/c. It consists of 4 large superlayers, with dimensions 8×6 m². The superlayers are interleaved with three hadron absorber segments, built from iron. To allow precise measurements of track directions, no absorber is put between the third and the fourth superlayer. The angular acceptance is 160 mrad vertically and 220 mrad horizontally. Three different chamber types are used

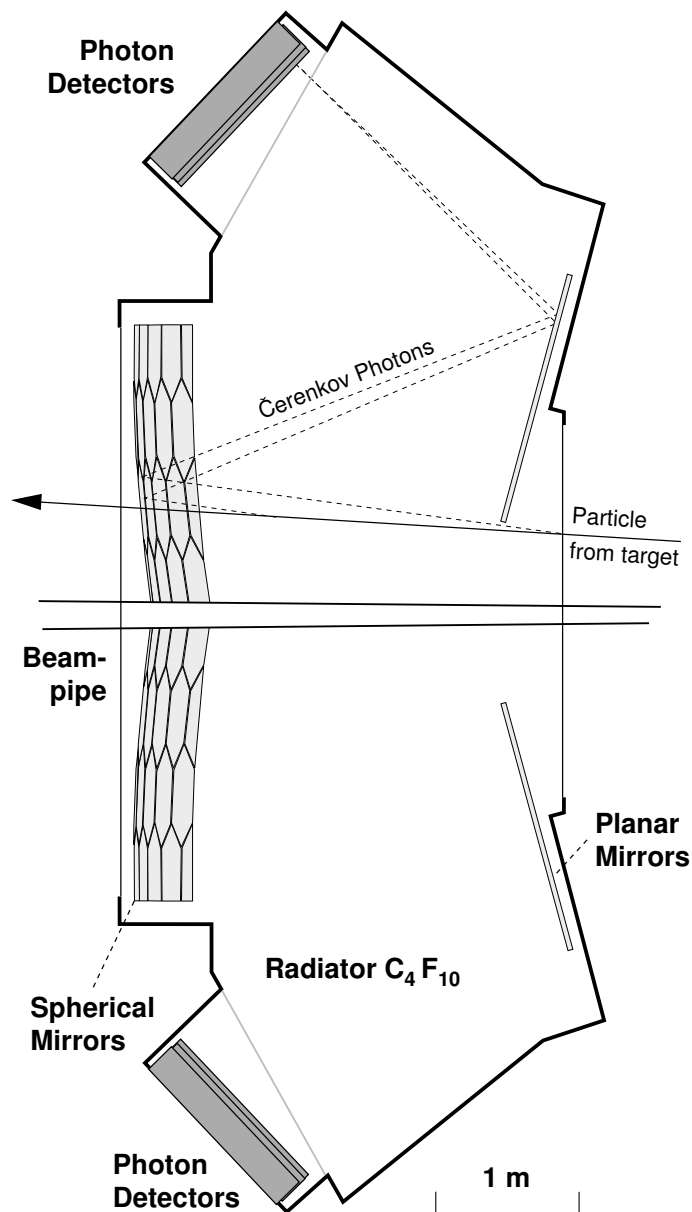


Figure 2.10: Ring imaging Cherenkov detector.

to compose the superlayers: tube chambers, pad chambers and gas pixel chambers. In the inner part of the muon detector gas pixel chambers of $9 \times 9 \times 30 \text{ mm}^3$ are used, in the outer part of the first two superlayers tube chambers are used, with cell dimensions of $14 \times 12 \text{ mm}^2$ and pitch 16 mm, while the last two superlayers use pad chambers of the same size. The tube chambers are closed-cell proportional wire chambers, while pad chambers are proportional wire chambers assembled from an open aluminum profile and closed with a copper phenolic board (Fig. 2.13). Both chambers consist of two mono layers, shifted for half a cell width, to ensure high efficiency. The chambers are 262 mm wide, and ~ 3 m long.

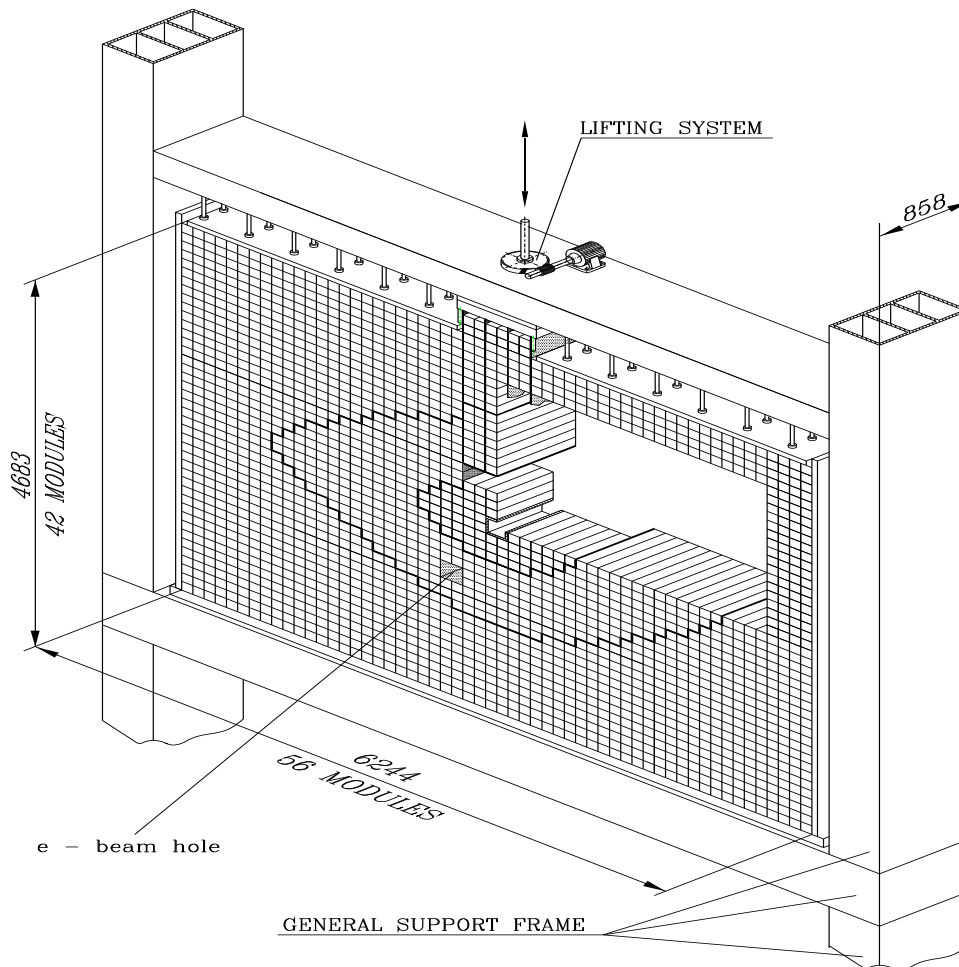


Figure 2.11: Schematic view of the ECAL

2.9 The data acquisition and triggering system

The HERA-B data was taken using two different types of triggers [37]. The di-lepton trigger was designed for the search of decays with two leptons in the final state, such as the decay of $J/\psi \rightarrow \mu^+ \mu^-$, which is one of the particles in the decay chain of the "golden decay mode". The second type is the interaction trigger, which does not enhance special physics states. During the data taking period 2002 and 2003, about 150×10^6 events were recorded using the di-lepton trigger and about 210×10^6 events using the interaction trigger. The data acquisition and the triggering architecture is shown in Fig. 2.14.

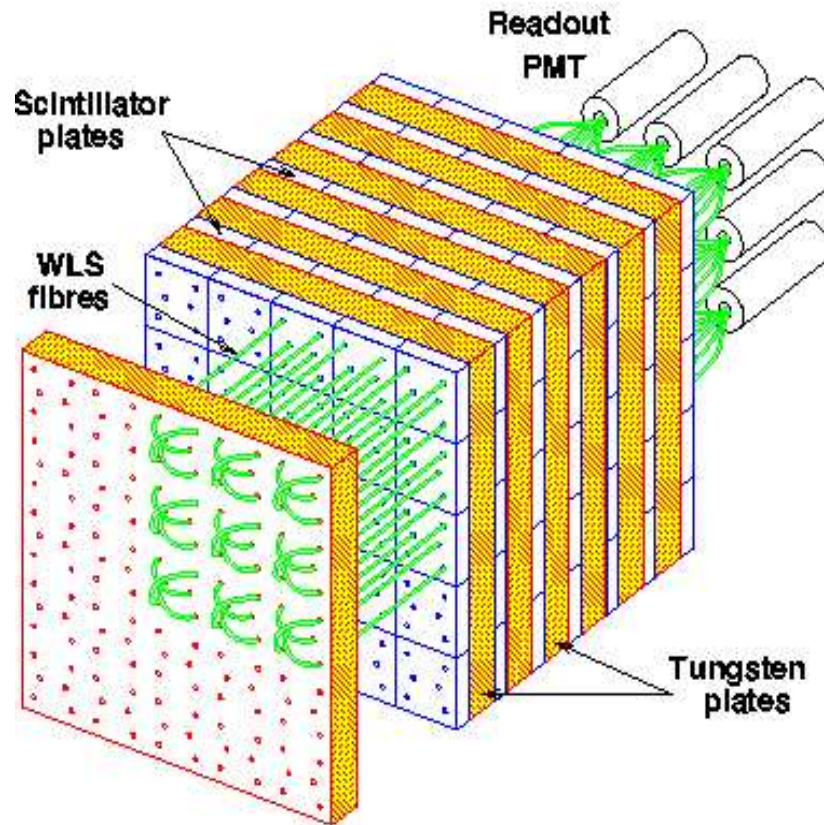


Figure 2.12: Schematic view of one ECAL inner module

2.9.1 Di-lepton trigger

The di-lepton trigger is divided into several stages, which reduce the event rate from 10.4 MHz down to the capacity of the data storage system of 1000 events per second. In the pre-trigger stage a search for two high p_T leptons is performed. The muon pre-trigger searches the last two chambers of the muon system for a signature of high p_T muons, while the electron pre-trigger searches for two clusters in the ECAL with sufficiently high transverse energy deposited. The candidates, which match either the first or the second pre-trigger requirement, are passed to the first level trigger. The first level trigger tries to trace back the tracks of the high p_T leptons by searching for hits in the tracking system in the defined search regions. The tracks are traced back to the magnet and a first rough estimation of the track's momenta are made. If a lepton pair is found and its invariant mass is in the J/ψ region, the event is forwarded to the second level trigger, if not, the event is rejected. The rejection factor of the first level trigger is about 200, so the input rate to the second level trigger is about 50kHz.

The second level trigger runs on a farm of 240 computers. To form the two tracks the hit information of all detector layers is used and the tracks are propagated through the magnet into the vertex detector. If a common vertex can be formed, the event is accepted and written to the

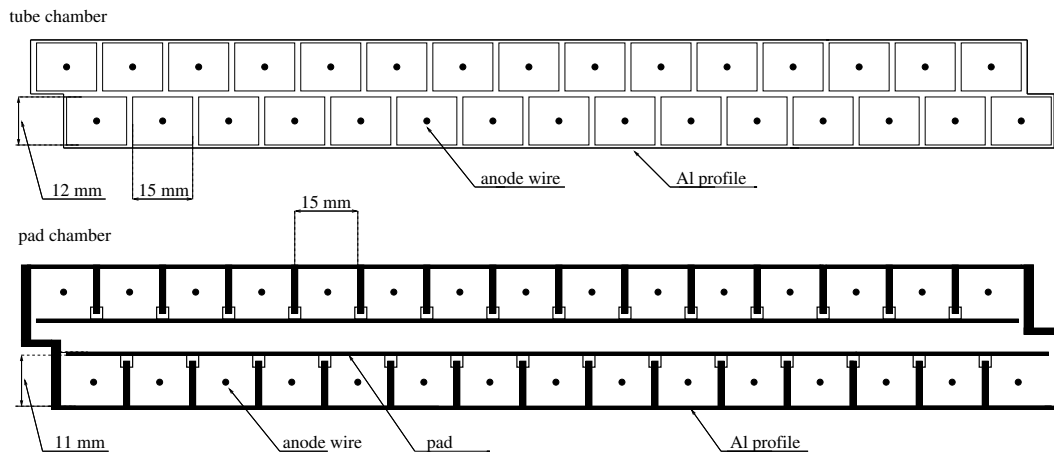


Figure 2.13: Schematic view of a tube chamber and a pad chamber construction

tape.

The designed third level trigger was unused in the data taking period 2002/2003 while the fourth-level trigger was used to make an online reconstruction of part of the events. These events were used for the online data quality monitoring. No events were rejected in this trigger level.

2.9.2 Random Trigger

About 5% of the events were taken with a random trigger, which operates simultaneously with other triggers. With the random trigger the events were accepted randomly, regardless of the state of the detector. Most of the recorded data triggered by the random trigger were empty events. The events taken with this trigger were used for luminosity measurements.

2.9.3 Interaction trigger

The interaction trigger was used to reject empty events. The requirements of this trigger are at least 20 hits in the RICH or minimum energy (1 GeV) deposited in the ECAL. With these requirements no final states are enhanced and such data allows a wide range of physics studies. The trigger efficiency, which is used for luminosity determination and therefore enters the calculation of cross sections, was evaluated using Monte Carlo simulation. Due to the soft threshold the efficiency of triggering on a single interaction is about 99% and depends slightly on the target material. For two or more interactions per event the efficiency rises to 100% for all target materials. The data used in this analysis was taken with the interaction trigger.

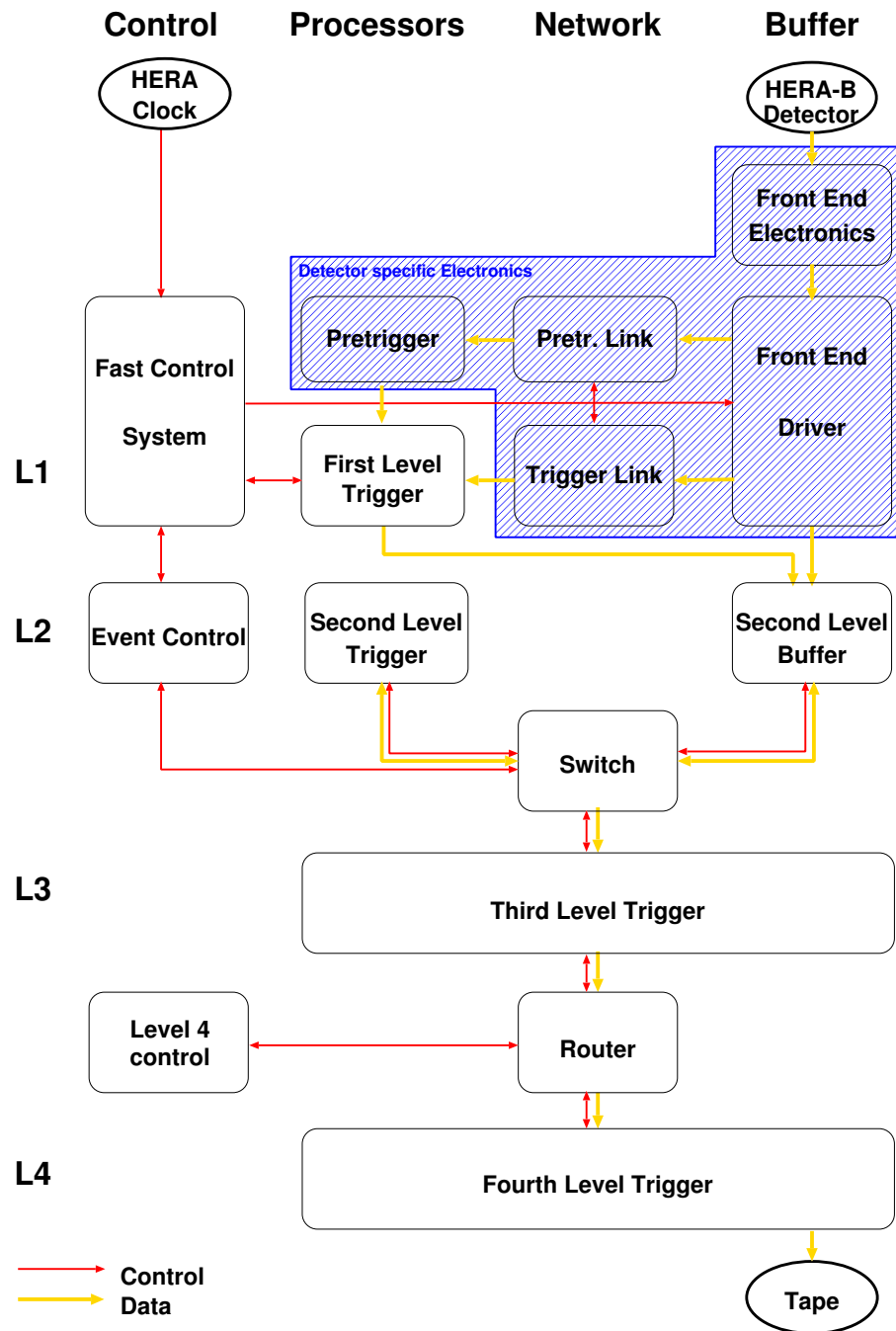


Figure 2.14: Data acquisition scheme and triggering system architecture

2.10 Luminosity determination

The integrated luminosity is determined from the number of interactions N and the corresponding cross section σ :

$$\mathcal{L} = \frac{N}{\sigma} \quad (2.1)$$

The method for luminosity measurement at HERA-B [38] is based on the determination of the average number of interactions per bunch crossing, λ_{tot} , and on the knowledge of the total interaction cross section σ_{tot} :

$$\mathcal{L} = \frac{N_{BX} \lambda_{tot}}{\sigma_{tot}} \quad (2.2)$$

where N_{BX} is the number of bunch crossings. λ_{tot} was evaluated on run-by-run basis by using a small fraction of events acquired with a random trigger in parallel to the interaction trigger. With the assumption that the number of interactions per filled bunch can be described by a single Poissonian distribution for all bunch crossings

$$P(n, \lambda_{tot}) = \frac{\lambda_{tot}^n e^{-\lambda_{tot}}}{n!}, \quad (2.3)$$

and the trigger efficiency for n interactions given by

$$(\epsilon_{tot})_n = 1 - (1 - \epsilon_{tot})^n, \quad (2.4)$$

where ϵ_{tot} is the trigger efficiency for a single interaction, the total number of recorded triggers resulting from interactions in the target, N_{IA} , is given by:

$$N_{IA} = N_{BX} \cdot \sum_{n=0}^{\infty} P(n, \lambda_{tot}) \cdot (\epsilon_{tot})_n = N_{BX} \cdot (1 - e^{-\epsilon_{tot} \cdot \lambda_{tot}}) \quad (2.5)$$

The total cross section σ_{tot} can be divided into elastic and inelastic contributions. The inelastic part is composed of the minimum bias cross section (σ_{mb}) and a diffractive part. Since mostly minimum bias interactions are recorded because for the other contributions either the production cross section is low or the detector acceptance is small, the number of interactions, N_{IA} , can also be expressed using minimum bias quantities, λ_{mb} and ϵ_{mb} :

$$N_{IA} = N_{BX} \cdot \sum_{n=0}^{\infty} P(n, \lambda_{mb}) \cdot (\epsilon_{mb})_n = N_{BX} \cdot (1 - e^{-\epsilon_{mb} \cdot \lambda_{mb}}) \quad (2.6)$$

By comparing Eq. 2.5 and Eq. 2.6 the relation $\lambda_{tot} \epsilon_{tot} = \lambda_{mb} \epsilon_{mb}$ can be found. N_{IA} can be further expressed as a function of the total number of recorded triggers, N_{tape} , and the number of background events, N_{bkg} :

$$N_{IA} = N_{tape} - N_{bkg} = N_{tape} (1 - f_{bkg}) \quad (2.7)$$

where f_{bkg} is evaluated using information from the random trigger. Using Eq. 2.6 and Eq. 2.7

the variables in Eq. 2.2 can be expressed as:

$$N_{BX} = \frac{N_{tape}(1 - f_{bkg})}{(1 - e^{-\lambda_{mb}\epsilon_{mb}})} \quad (2.8)$$

$$\frac{\lambda_{tot}}{\sigma_{tot}} = \frac{\lambda_{mb}}{\sigma_{mb}} \cdot K_A \quad (2.9)$$

with

$$K_A = \frac{\sigma_{mb}\epsilon_{mb}}{\sigma_{tot}\epsilon_{tot}} \quad (2.10)$$

Setting Eqs. 2.8 and Eq. 2.9 into Eq. 2.2 the integrated luminosity reads:

$$\mathcal{L} = \frac{N_{tape}(1 - f_{bkg}) \cdot \lambda_{mb}}{(1 - e^{\epsilon_{mb}\lambda_{mb}}) \cdot \sigma_{mb}} \cdot K_A \quad (2.11)$$

The measured quantities are N_{tape} , f_{bkg} and λ_{mb} . The total and the inelastic cross sections were taken from published experimental data ([38] and references therein); the efficiencies were determined from Monte Carlo simulation.

The average number of interactions per bunch crossing, λ_{mb} , is obtained from Eq. 2.6

$$\lambda_{mb}(X) = -\frac{1}{\epsilon_{mb}(X)} \cdot \ln\left(1 - \frac{N_{IA}(X)}{N_{BX}}\right) \quad (2.12)$$

by combining the information from a variety of subdetectors, where $N_{IA}(X)$ is the number of events with observable X and $\epsilon(X)$ is the corresponding efficiency evaluated from Monte Carlo. The observables X were the number of hits in the RICH, the total energy deposition in the ECAL (separately for the different regions and separately for the total energy), the number of reconstructed clusters in the ECAL, the number of cells hit in the ECAL and the number of reconstructed tracks in the VDS and OTR. For the final value of λ_{mb} the average of the measured $\lambda_{mb}(X)$ was taken.

The systematic uncertainties of the measurement come from the efficiency determination ϵ_{tot} , from the possible non-Poissonian behavior of the HERA bunch structure, from the error of the total cross section σ_{tot} and from the estimation of the number of background interactions. The individual relative errors on the integrated luminosity are 3.9%, 4.2% and 2.9% for the carbon, titanium and tungsten wires respectively and a common scaling error is 3%.

20166	20168	20169	20170	20171	20172	20195	20198
20199	20339	20340	20341	20388	20464	20466	20467
20468	20469	20474	20478	20479	20480	20507	20653
20663	20668	20669	20670	20671	20675	20676	20677
20678	20679	20680	20682	20693	20695	20700	20701
20703	20704	20705	20706	20711	20723	20724	20725
20726	20728	20734	20735	20736	20737	20738	20739
20740	20742	20743	20744	20746	20747	20749	20764
20766	20767	20768	20769	20770	20771	20772	20773

Table 3.1: Run numbers of the real data used in the analysis

3 Data sample

The analysis is based on the minimum bias sample, recorded during November and December 2002 and reconstructed with the “reprocessing 5”. This data sample was taken with the interaction trigger. It consists of about 180 million events, distributed among four different targets operated in a single wire mode: below1 (C), inner1 (W), below2 (Ti), and inner2 (C). The working frame for the analysis code was ARTE-04-01-r5 [39].

3.1 Selected runs

Run numbers of the runs used in this analysis are given in Table 3.1 and a summary of the data statistics and the integrated luminosities is given in Table 3.2. Runs with the numbers from 20653 to 20773 which were taken during a short period in December (from 9 to 21 December) represent almost 80% of the statistics used in this analysis. This sample is referred to as the *Golden MB data*.

3.2 Monte Carlo samples

For the efficiency determination and for the cut optimizations we used the Monte Carlo (MC) simulated data. The D mesons were generated with the PYTHIA 5.7 generator [10], and the FRITIOF generator [40] was used for the rest of the proton interaction inside the nucleus. The

Target	A	events [$\times 10^6$]		\mathcal{L}_i [μb^{-1}]	
		full sample	Golden sample	full sample	Golden sample
b1 (C)	12.01	68.8	65.1	276.565	257.246
i1 (W)	183.84	67.6	54.8	35.884	28.478
b2 (Ti)	47.88	24.7	22.9	30.904	28.697
i2 (C)	12.01	20.5	0	97.970	0
Sum		182	143	12575	9698

Table 3.2: Summary of the data statistics and the integrated luminosities used in the analysis. In the last row a weighted sum $\sum A_i \mathcal{L}_i$ is given for the integrated luminosity.

MC sample	No of runs	run numbers (run09_)
$D^+ \rightarrow K^- \pi^+ \pi^+$	8	1633, 1683 - 1689
$D^0 \rightarrow K^- \pi^+$	8	1692 - 1699
$D_s^+ \rightarrow \phi \pi^+ \rightarrow (K^- K^+) \pi^+$	8	1712 - 1719
$D^{*+} \rightarrow D^0 \pi^+ \rightarrow (K^- \pi^+) \pi^+$	8	1702 - 1709
$c\bar{c}$	16	411, 413-416, 418-428

Table 3.3: Run numbers of the MC sample

detector response was generated with the standard HBGEANT package [41]. A realistic detector geometry description was used. Detector resolutions and maskings were simulated to the best possible knowledge. During the reconstruction, the signal MC events were mixed with inelastic MC events to account for a Poissonian distribution of the number of interactions. The average measurement rates were well simulated by the mixing. The same ARTE code as for the real data was also used for the reconstruction of the MC data samples.

In the analysis we used the latest MC samples which are tuned at the generator level to achieve a better agreement of event multiplicities with the real data. Besides the signal MC samples, we also used $c\bar{c}$ Monte Carlo samples for the description of the charm background in the D^0 analysis. This MC sample was generated with the older generator settings and does not describe the event multiplicities well.

In Table 3.3 we provide the run numbers of MC samples used in the analysis and in Table 3.4 a summary of the MC statistics.

$D^+ \rightarrow K^- \pi^+ \pi^+$			
wire	Material	No. of decays	$-0.15 < x_F < 0.05$
b1	C	355110	162786
i1	W	452737	207036
b2	Ti	224748	103270
i2	C	205168	94505
Total		1237763	567597
$D^0 \rightarrow K^- \pi^+$			
wire	Material	No. of decays	$-0.15 < x_F < 0.05$
b1	C	369638	168980
i1	W	424867	191012
b2	Ti	207661	94150
i2	C	207146	94040
Total		1209312	548182
$D_s^+ \rightarrow \phi \pi^+ \rightarrow (K^- K^+) \pi^+$			
wire	Material	No. of decays	$-0.15 < x_F < 0.05$
b1	C	137051	64983
i1	W	164110	78770
b2	Ti	83308	39853
i2	C	52599	26746
Total		437168	210352
$D^{*+} \rightarrow D^0 \pi^+ \rightarrow (K^- \pi^+) \pi^+$			
wire	Material	No. of decays	$-0.15 < x_F < 0.05$
b1	C	445166	196224
i1	W	664394	293158
b2	Ti	234493	103450
i2	C	225131	99019
Total		1569184	691851
$c\bar{c}$ events			
wire	Material	No. of events	
b1	C	1106452	
i1	W	2137418	
b2	Ti	702533	
i2	C	738840	
Total		4685243	

Table 3.4: Summary of the Monte Carlo statistics used for the analysis.

4 Data selection

At the HERA-B energy the charm production cross section is expected to be 2-3 orders of magnitude smaller than the inelastic cross section. Taking into account also relatively small branching ratios for the decay modes into 2 or 3 charged final state particles and a limited acceptance of the detector, one could expect huge backgrounds, if strict data selection criteria were not used. Particle identification, for example, is not sufficient to extract signals. However, the large boost of the center-of-mass system of HERA-B ($\gamma = 22$), causing D mesons to decay several millimeters from the target, combined with a good vertex resolution (≈ 0.5 mm) provides a possibility to distinguish D meson candidates from the particles originating at the primary interaction point. The data selection thus required a detached secondary vertex, formed by tracks not coming from the primary interaction point, as well as the identification of kaons and pions.

4.1 Reconstruction of D mesons

Since the detached vertex is required for the ground state D mesons, only events with at least one reconstructed primary vertex were selected. The reconstruction was done in the following stages:

Track selection The reconstructed charged tracks were selected with the following requirements:

- at least 5 hits in the VDS and 10 hits in the OTR
- the track is not a clone
- the momentum is smaller than 250 GeV/c
- the $\chi^2/n.d.f$ of a track fit is below 10

Particle identification From the selected tracks, lists of positive and negative pions and kaons were formed with the following selection criteria for the RICH likelihood probabilities (L_e, L_μ, L_π, L_K represent the likelihood probabilities for the electron, muon, pion and kaon hypothesis):

- for pions in D^0, D^+ and D_s^+ reconstruction: $L_e + L_\mu + L_\pi > 0.05$

- for slow pions in D^{*+} reconstruction: no particle identification was required
- for kaons in D^0 reconstruction: $L_K > 0.5$
- for kaons in D^+ and D_s^+ reconstruction: $L_K > 0.33$

Primary vertex The reconstructed primary vertices were taken without any requirement. Since the proton interaction point is inside the target wire, which is known with much better accuracy than the primary vertex in the coordinates transverse to the wire, we replaced those two with the reconstructed target position. The replacement is done also for the corresponding diagonal elements of the primary vertex covariance matrix, which were replaced with the wire dimensions divided by $\sqrt{12}$. The non diagonal elements of the covariance matrix were set to 0.

Combinations The lists were combined into D^0 , D^+ and D_s^+ candidates providing that the tracks forming a combination were different and that each combination was taken only once. The invariant masses of the combinations were calculated and only the candidates with invariant mass in the interval of ± 0.5 GeV around the D meson nominal mass were taken in the further analysis stages. For the D_s^+ candidates, an additional cut was applied on the invariant mass of the K^+K^- pairs: only the candidates with $m(K^+, K^-)$ in the interval of ± 20 MeV around the ϕ nominal mass were accepted. The D^{*+} candidates were combined from the D^0 candidates and the slow pions after the vertex fit to D^0 . Both combinations were made, the right sign (D^0, π^+) and the wrong sign (\bar{D}^0, π^+). The wrong sign combinations were used for the combinatorial background estimation in the right sign channel.

Vertex fit A common vertex of each track combination was fitted with the Grover vertexing package [42]. The unconstrained fit was used. The combination was accepted, if the fit was successful and if its χ^2 probability was greater than 0.1%. To reduce the cpu time in the next stages, a cut on the distance *significance*[§] of the vertex to the wire was applied: the candidate was accepted, if its vertex position was at least 4 sigma downstream of the wire.

Primary vertex association The candidate was then associated with the primary vertex. In the case of events with multiple reconstructed primary vertices, the one with the smallest impact parameter significance of the D meson candidate was chosen.

Primary vertex refit To avoid a possible bias in the primary vertex position due to tracks from the D meson candidate, the tracks from the D meson candidate were excluded from the associated primary vertex and the primary vertex was refitted. The geometrical fit from Grover, function *GeoFit* was used, since the original fit was also done with this function.

[§]With the *significance* we mean the quantity divided by its estimated error given by the covariance matrix

4.2 Analysis cuts

To select the most appropriate variables for discriminating the processes under study (signal events) from the background events, and to determine the optimal cut values in these variables, two data samples were used. For the signal events, we used MC generated events, while for the background, the side bands in the corresponding invariant mass were used, as described in the next section.

The main source of the background arises from combinations of particles emerging from the primary interaction point. This background can be reduced by the following three requirements: (1) the secondary vertex is detached, (2) the tracks forming the secondary vertex did not come from the primary interaction point and (3) the D meson candidate came from the primary interaction point. To fulfill these criteria we used the cuts on the following variables:

- $d(D)$ the distance significance of the secondary vertex to the primary interaction point given by the associated primary vertex
- $b(K)$, $b(\pi)$ the impact parameter significance of a pion or a kaon to the associated primary vertex
- $b(D)$ the impact parameter significance of a D meson candidate to the associated primary vertex

Here the significance of a certain variable refers to the value of the variable divided by its error as estimated in the reconstruction of the event.

Due to high interaction rates more than one primary vertex was found in about 10% of events. In this case, a good detached vertex could be fitted also from two or three tracks coming from different primary vertices. To suppress this kind of background, we used the impact parameter significance to the closest primary vertex $b_m(K)$ or $b_m(\pi)$ instead of impact parameter significance to the associated primary vertex $b(K)$ or $b(\pi)$ ¶.

We found that for the three body decay of D^+ , a more effective cut than the cuts on single impact parameter significances of daughter tracks is the cut on their product $b_m(K)b_m(\pi_1)b_m(\pi_2)$. The distributions for the background in real data sidebands and for the MC signal are shown in Fig. 4.1. This cut also includes implicitly a cut on the distance significance of a secondary vertex, thus the latter is not needed^{||}. For two body decays the situation is opposite.

By studying the correlation between the cut on the product of impact parameter significances and the proper life time we found that we could improve the signal significance, if we also applied a cut of the form: $\sqrt[3]{b_m(K)b_m(\pi_1)b_m(\pi_2)} > 4(t - t_0)$, as shown in Fig. 4.2 by the red line. The proper life time t is in units of the D meson mean life time.

¶Note that for events with exactly one primary vertex, b and b_m are the same

^{||}In the preselection of the D^+ we used a cut $d(D^+) > 7$ to reduce the ntuple size. The result does not depend on this cut, because the product-cut on the impact parameters selects events with larger distance significances only

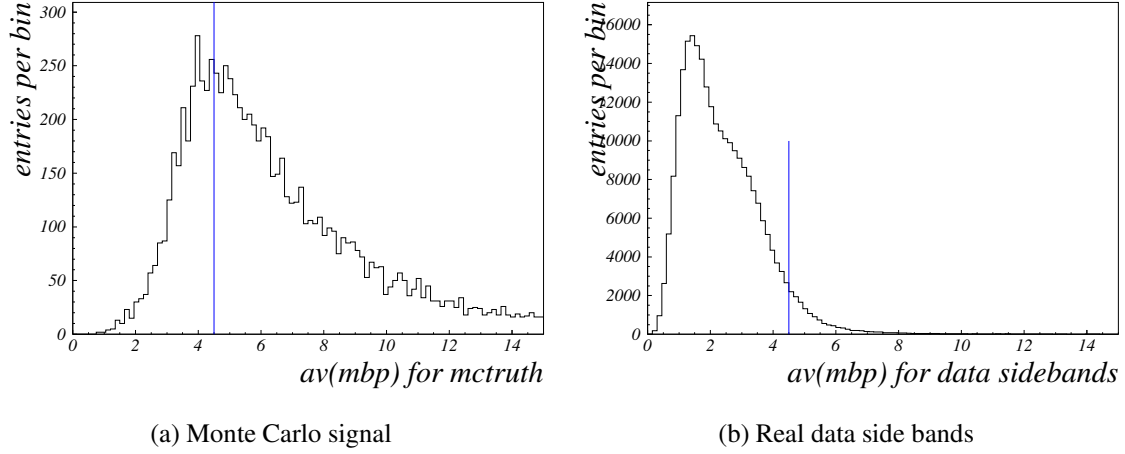


Figure 4.1: Distribution of $\sqrt[3]{b_m(K)b_m(\pi_1)b_m(\pi_1)}$ for the Monte Carlo simulated signal (left) and background from real data sidebands (right). The blue line indicates a possible cut.

The cuts on the p_T of daughter tracks were also studied and we found that the cut on the product of the D meson momentum and the transverse momenta of daughter tracks $p_{pT} = p(D)\prod_i p_T(i)$ is more effective than the cuts on single variables. This kind of cut, when used in addition to the detached vertex cuts, improves the signal significance, but also changes the shape of the background at invariant masses below the signal peak. It is harder to find the appropriate function to describe the shape of the background. The comparison of the p_{pT} distributions of the MC signal and the background in the real data side bands is shown in Fig. 4.3.

4.3 Optimization of analysis cuts

For each decay mode the optimal cuts were determined by maximizing the signal significance $S/\sqrt{S+B}$ with S being the number of signal events and B the number of background events in a $\pm 3\sigma$ window centered at the D meson nominal mass (signal window). The signal S was taken from the Monte Carlo simulation and was scaled to the luminosity of real data by dividing it by the scaling constant f :

$$S = \frac{S_{MC}}{f} \quad (4.1)$$

The number of the Monte Carlo signal events S_{MC} surviving the cuts was determined by counting the events in the signal window and subtracting the counts in the side bands. The scaling factor f was calculated by:

$$f = \frac{N_{MC}}{N_{data}} \quad (4.2)$$

where N_{MC} is the number of generated decays in the Monte Carlo simulation and $N_{data} = \sigma Br \sum A_i \mathcal{L}_i$ is the estimation for the number of decays in the real data. For the latter we obtained the estimation for the production cross sections σ from fits to the published D meson

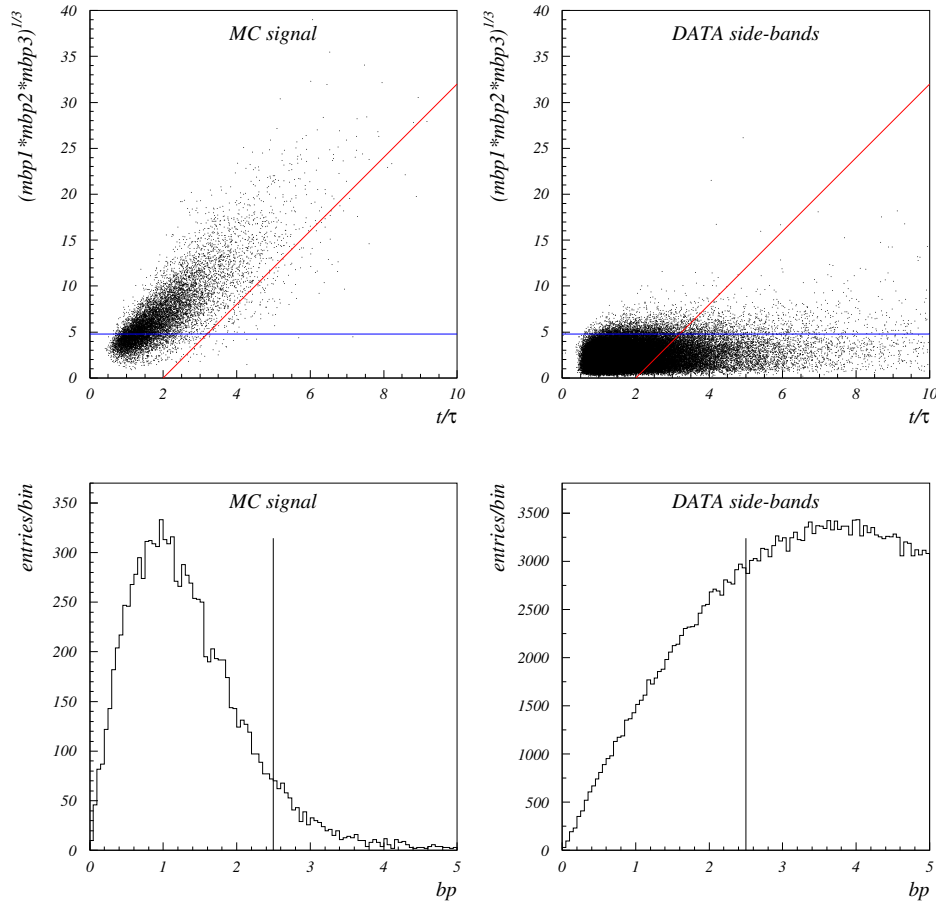


Figure 4.2: The correlations between geometrical average of the impact parameter significances of the D^+ daughter tracks $\sqrt[3]{b_m(K)b_m(\pi_1)b_m(\pi_1)}$ and the proper life time t/τ (top). The distributions of the D^+ impact parameter significance $b(D)$ (bottom). Diagrams on the left are for Monte Carlo signal and on the right are for real data side bands. Possible cuts are indicated by the lines.

cross sections, Table 1.3. For the D_s^+ we estimated the cross section by taking, according to a prediction based on experimental results [1], 20% of the sum of D^0 and D^+ cross sections from Table 1.3.

In the case of ground state D mesons, the number of background events B was estimated from the real data side bands. A linear extrapolation was used. For the D_s^+ a mass region $|\Delta m_{D^+}| < 50 \text{ MeV}$, where a peak of the decay $D^+ \rightarrow \phi\pi^+$ is expected, was excluded from side bands. To reduce the sensitivity to statistical fluctuations, the side bands chosen were larger than the signal window, thus another scale factor s was introduced, equal to the ratio between the widths of the side band and the signal windows. Similar to Eq. 4.1:

$$B = \frac{B_{sb}}{s} \quad (4.3)$$

with B_{sb} being the event counts in the side bands.

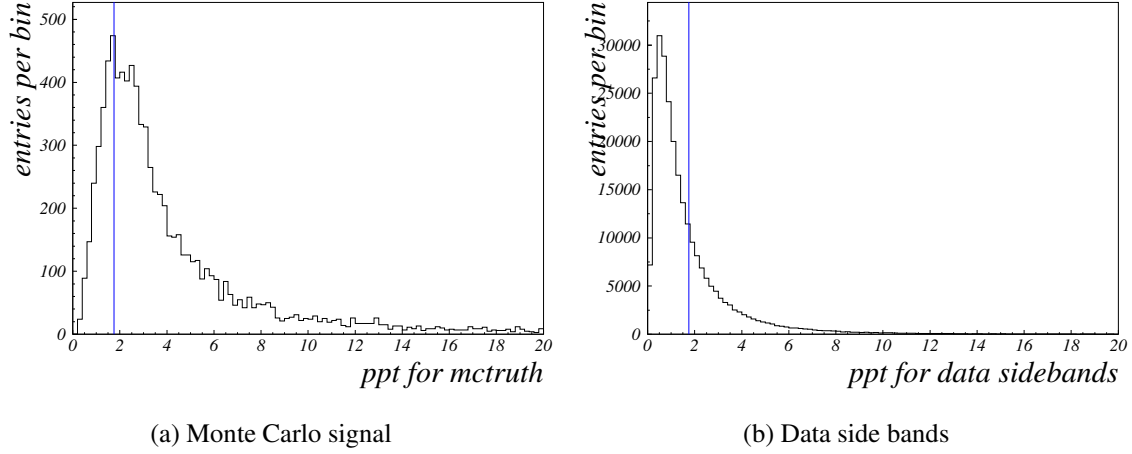


Figure 4.3: Distribution of the p_{pT} for the Monte Carlo simulated signal (left) and for the background from real data sidebands (right). The lines indicate a possible cut.

meson	signal window [MeV]	side bands [MeV]	f	s
D^0	$ \Delta m < 75$	$75 < \Delta m < 150$	56	1
D^+	$ \Delta m < 50$	$50 < \Delta m < 300$	35	5
D_s^+	$ \Delta m < 45$	$45 < \Delta m < 450$	129	7.9
D^{*+}	$ \Delta q < 2.5$		232	1

Table 4.1: Window sizes and scale factors used in the cut optimization.

In the case of the D^{*+} the wrong sign combinations from real data were used to estimate the background in the signal window. As is usually done for this decay, the signal was reconstructed in the mass difference $q = m(K, \pi, \pi_{slow}) - m(K, \pi) - m_\pi$ rather than in the invariant mass of the K, π, π_{slow} combinations. The window sizes and the scaling factors are given in Table 4.1

Two methods were used to find the maximum:

Iterative method A loop over cuts is performed. The cuts were treated as independent and were optimized sequentially. The optimum for a given cut was searched in a reasonable interval by calculating the signal significance in 1000 points. For each cut, the cut value with the highest significance was used in the further calculations. This procedure ran iteratively. Typically three iterations were sufficient to find the maximum.

3D Optimization This procedure was used for the optimization of three cuts. First, a sufficiently large region of interest was chosen. This region was divided into a matrix of $10 \times 10 \times 10$ equally spaced points and the signal significance for each point was calculated. Then the position of the maximum was determined. In the second stage, the region of interest was decreased by factor of 5 in each dimension and centered at the position of maximum from the first stage,

and the maximum finding procedure was repeated.

The analysis cuts are summarized in Table 4.2. Not all have been optimized: the particle identification, because there is a small discrepancy between the real data and the MC sample; the cuts on the invariant mass of the intermediate state, because the peak widths are narrower in the MC samples; and the cosine of the angle between K and π in the rest frame of the ϕ . The latter one was chosen so that it cuts $1/2$ of the background while keeping $7/8$ of the signal **.

In addition to the analysis cuts, the cut on the accessible phase space was also applied. As shown in section 6.3, the acceptance in p_T is not limited and the limitation comes only from the acceptance in x_F . We defined the visible range in x_F by the interval, where the acceptance is larger than approximately 10% of its maximum value. The HERA-B visible range is:

$$-0.15 < x_F < 0.05 \quad (4.4)$$

After applying the selection cuts, the remaining data was scanned for events with more than one D-meson candidate. For D^0 , D^+ and D_s^+ the candidate with the largest decay distance significance $d(D)$ was kept. For the D^{*+} first the candidates were selected, where the intermediate D^0 had the largest decay distance significance. If more combinations used the same D^0 candidate in combination with a different π_{slow} then the candidate with the highest vertex probability was kept.

**Because ϕ is a vector while initial and final state particles are scalars, the distribution is proportional to $\cos^2 \theta_{K\pi}$.

$D^0 \rightarrow K^- \pi^+$	$D^+ \rightarrow K^- \pi^+ \pi^+$
not optimized	
$L_K(K) > 0.5$ $L_e(\pi) + L_\mu(\pi) + L_\pi(\pi) > 0.05$	$L_K(K) > 0.33$ $L_e(\pi) + L_\mu(\pi) + L_\pi(\pi) > 0.05$ $d(D^+) > 7$
optimized	
$d(D^0) > 6.1$ $b(D^0) < 2.4$ $b_m(K) > 3.4$ $b_m(\pi) > 3.7$	$b(D^+) < 2.5$ $b_m(K)b_m(\pi_1)b_m(\pi_2) > 146$ $\sqrt[3]{b_m(K)b_m(\pi_1)b_m(\pi_2)} > 4(t - t_0), t_0 = 1.68$
$D_s^+ \rightarrow \phi \pi^+ \rightarrow K^- K^+ \pi^+$	$D^{*+} \rightarrow D^0 \pi^+ \rightarrow K^- \pi^+ \pi^+$
not optimized	
$L_K(K) > 0.33$ $L_e(\pi) + L_\mu(\pi) + L_K(\pi) > 0.05$ $ \Delta m_\phi < 10 \text{ MeV}$ $ \cos \theta_\phi > 0.5$	$L_K(K) > 0.5$ $L_e(\pi) + L_\mu(\pi) + L_K(\pi) > 0.05$ $L_e(\pi_{slow}) + L_\mu(\pi_{slow}) + L_K(\pi_{slow}) \geq 0$ $ \Delta m_{D^0} < 75 \text{ MeV}$
optimized	
$d(D_s^+) > 5.3$ $b(D_s^+) < 2.11$ $b_m(K^-)b_m(K^+)b_m(\pi) > 28.7$ $\sqrt{b_m(\phi)b_m(\pi)} > 0.75(t - t_0), t_0 = 1.0$	$b(D^0) < 2.4$ $b_m(K) > 2.1$ $b_m(\pi) > 1.7$ $p_{pT}(D^0) > 17.7$

Table 4.2: Analysis cuts

4.4 Data signals

The invariant mass distributions that result from combining the particles and applying the selection criteria discussed above are shown in Figs. 4.5, 4.6, 4.7 and 4.8. Besides the total data sample, the invariant mass distributions for the following subsamples are also presented: particle and anti-particle, the C, W and Ti target materials and the golden and non-golden data samples.

The signals were fitted by a Gaussian function while for the background different shapes were used since the shape depends on the type of the D meson. For the D^+ and D_s^+ the background was fitted by an exponential function. The background in the D^0 reconstruction is more complicated and consists of a combinatorial part, fitted by an exponential and a background from partially reconstructed charm decays. This background appears to the left of the D^0 peak. We took the shape of the charm background from the $c\bar{c}$ Monte Carlo simulation after applying the analysis cuts to the events. The histogram was smoothed and normalized to its sum equal to 1 (Fig. 4.4). The normalization constant was a free parameter in the fit.

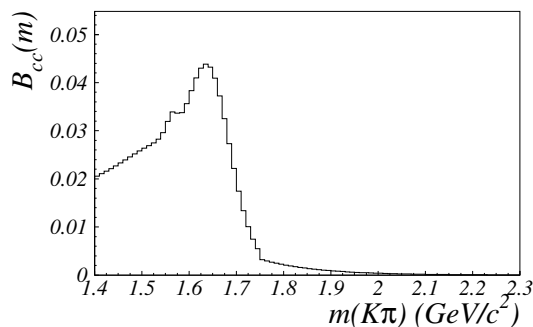


Figure 4.4: The shape of the $c\bar{c}$ background

In the D_s^+ invariant mass distribution, the Cabibbo suppressed decay of $D^+ \rightarrow \phi\pi^+$ is also seen (the peak left of the D_s^+ peak). We included this peak in the fit function as an additional Gaussian with its position fixed and the normalization as a free parameter. The position was fixed to the value from the fit to $D^+ \rightarrow K^-\pi^+\pi^+$ invariant mass distribution, while the width was a free parameter but shared with the gaussian, which was used to describe the Cabibbo favored peak $D_s^+ \rightarrow K^-K^+\pi^+$.

The background in the D^{*+} reconstruction was parameterized as $a(q^{1/2} + bq^{3/2})$ with parameters a and b being free in the fit to the total data sample. In the fits to subsamples, the shape was fixed by taking the value of b from the fit to total data sample and only the normalization parameter a was left free.

To ensure the stability of the fitting procedure, the subsamples of all D meson invariant mass distributions were fitted with a fixed signal position and width, both taken from the fit to total data samples.

The fitted positions and widths are summarized in Table 4.3. The peak positions are within one standard deviation from the corresponding world average value [11], with the exception of

	DATA		MC		world average
meson	m_0 [MeV]	σ_m [MeV]	m_0 [MeV]	σ_m [MeV]	mass [MeV]
D^0	1863 ± 2	21.4 ± 2	1868 ± 0.2	17.0 ± 0.2	1865
D^+	1869 ± 2	17.4 ± 2	1872 ± 0.2	13.8 ± 0.2	1869
D_s^+	1961 ± 4	10.1 ± 3	1971 ± 0.4	12.2 ± 0.4	1968
	q_0 [MeV]	σ_q [MeV]	q_0 [MeV]	σ_q [MeV]	Δmass [MeV]
D^{*+}	6.0 ± 0.2	1.0 ± 0.2	5.99 ± 0.01	0.68 ± 0.01	5.85

Table 4.3: The fitted positions and widths of the signal peaks in real data and in the Monte Carlo simulation. For comparison, the world average [11] is also given.

sample	D^0	D^+	D_s^+	D^{*+}
total	174.8 ± 16.8	148.2 ± 15.6	11.4 ± 4.0	61.3 ± 13.0
particle	75.9 ± 10.9	54.9 ± 9.4	4.9 ± 2.6	21.0 ± 6.6
anti-particle	99.0 ± 11.9	92.8 ± 11.3	6.7 ± 2.9	40.6 ± 8.3
C	66.1 ± 9.6	52.9 ± 8.4	4.2 ± 2.2	26.6 ± 6.4
W	92.3 ± 11.7	78.8 ± 10.9	6.7 ± 3.0	24.8 ± 7.5
Ti	17.4 ± 5.7	16.7 ± 5.3	0.4 ± 1.0	9.6 ± 4.0
gold	133.7 ± 14.1	116.5 ± 13.1	7.5 ± 3.3	55.6 ± 9.9
non gold	41.2 ± 7.8	31.7 ± 6.8	3.7 ± 2.0	6.2 ± 3.9

Table 4.4: Number of reconstructed D mesons in the real data.

D_s^+ , which deviates by two sigma. Fits to Monte Carlo signals show slightly larger deviations and in the opposite direction compared to the real data. The widths of the signal peaks are about 30% larger when compared to the Monte Carlo simulation. It becomes true also for the D_s^+ signal, if we take the large error into account. Similar discrepancies were observed also for the widths of signal peaks of the reconstructed $J/\psi \rightarrow \mu^+\mu^-$ and $K_S^0 \rightarrow \pi^+\pi^-$ decays.

The numbers of reconstructed D mesons are summarized in Table 4.4. In total we reconstructed 175 D^0 , 148 D^+ , 11 D_s^+ and 61 D^{*+} decays. The signals in all subsamples were also found and successfully fitted.

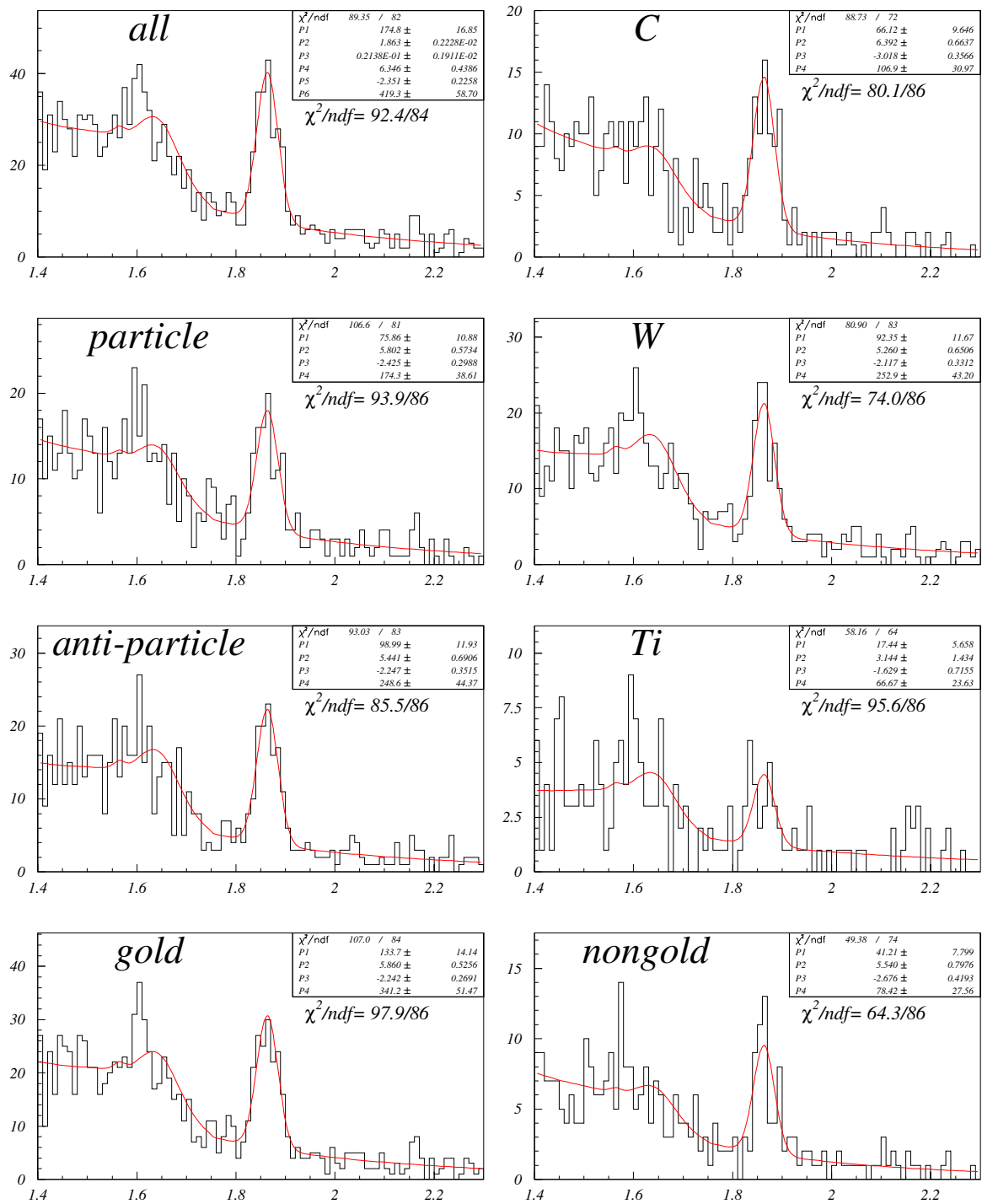


Figure 4.5: Invariant mass distributions for $D^0 \rightarrow K^- \pi^+$ in the real data for total sample (all) and for seven subsamples. The subsamples were fitted with the peak position and width fixed from the fit to the total sample. Below the statistics box the Pearson's χ^2 of the fit is printed.

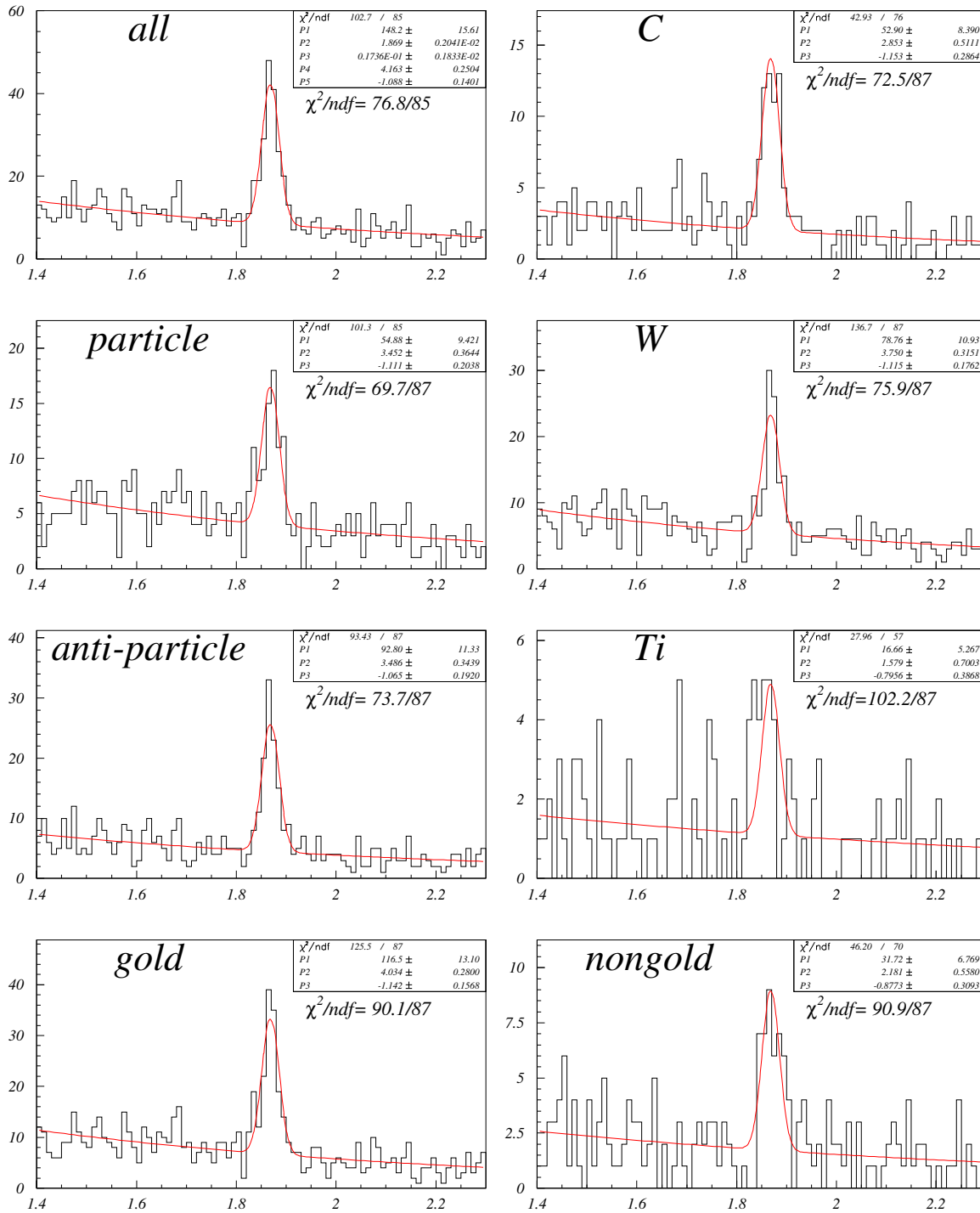


Figure 4.6: Invariant mass distributions for $D^+ \rightarrow K^- \pi^+ \pi^+$ in the real data for total sample (all) and for seven subsamples. The subsamples were fitted with the peak position and width fixed from the fit to the total sample. Below the statistics box the Pearson's χ^2 of the fit is printed.

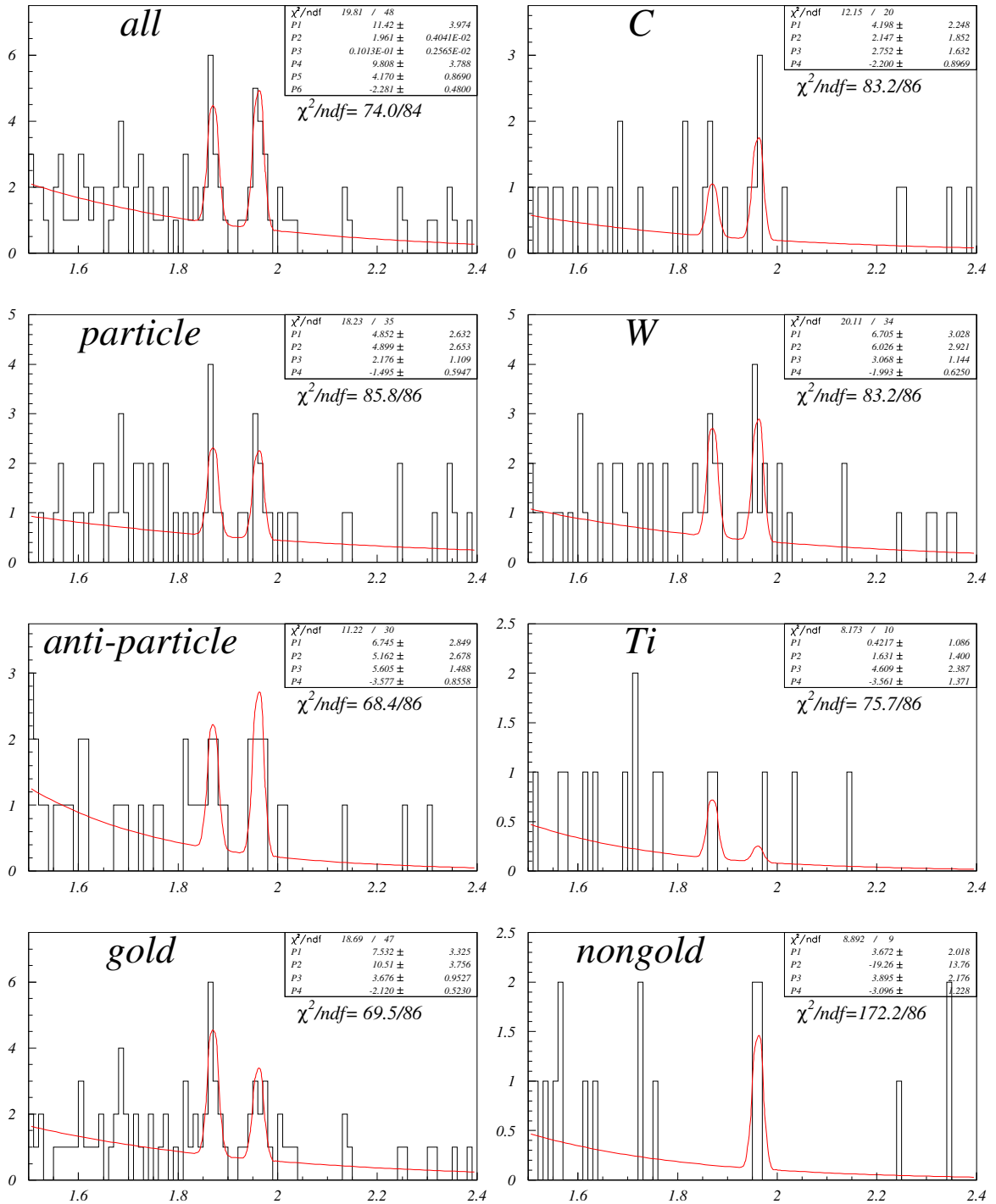


Figure 4.7: Invariant mass distributions for $D_s^+ \rightarrow \phi\pi^+ \rightarrow (K^-K^+)\pi^+$ in the real data for total sample (all) and for seven subsamples. Besides the D_s^+ peak at 1.96 GeV the D^+ peak at 1.87 GeV is also seen, corresponding to the Cabibbo suppressed decay $D^+ \rightarrow \phi\pi^+$. The subsamples were fitted with the peak position and width fixed from the fit to the total sample. Below the statistics box the Pearson's χ^2 of the fit is printed.

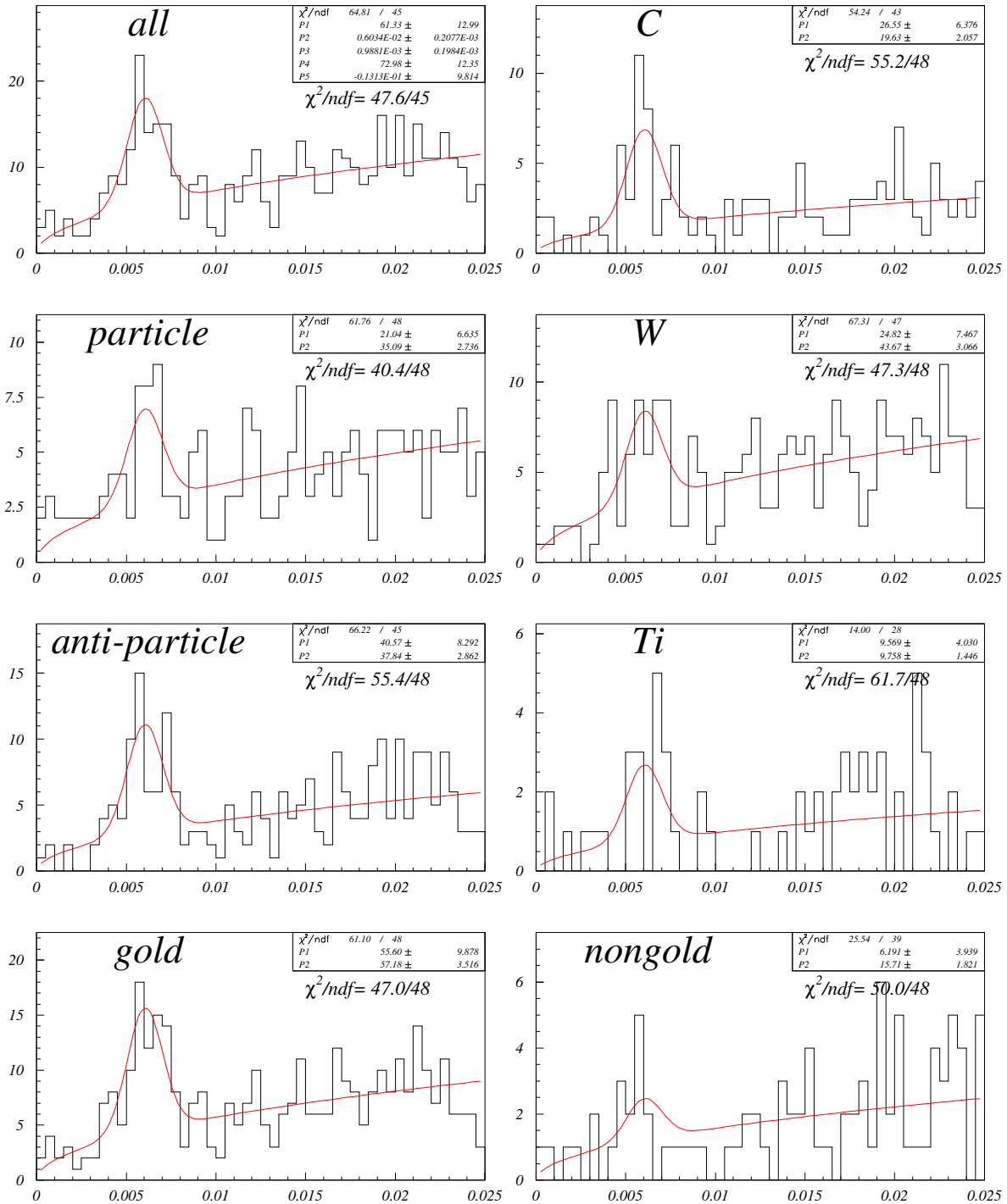


Figure 4.8: Invariant mass differences for $D^{*+} \rightarrow D^0 \pi^+ \rightarrow (K^- \pi^+) \pi^+$ in the real data for total sample (all) and for seven subsamples. The subsamples were fitted with the peak position and width and with background shape fixed from the fit to the total sample. Below the statistics box the Pearson's χ^2 of the fit is printed.

4.5 D meson life times

For the signal consistency checks we measured the D meson proper time distributions. We checked whether the acceptance corrected distributions were exponential and whether the fitted life times were in agreement with the world average [11]. We used a simultaneous maximum likelihood fit of events in the signal window and in the side bands. The side bands were chosen to be the same size as the signal window. The assumption was, that the sidebands contain background events only, whereas the signal window contains signal and background events. The shape of the signal was parameterized as

$$S(t) = \left(\frac{N_D}{\tau_D} \cdot e^{-t/\tau_D} \right) \cdot \epsilon(t) \quad (4.5)$$

and the shape of the background as

$$B(t) = \left(\frac{N_{bg}}{\tau_{bg}} \cdot e^{-t/\tau_{bg}} + C \right) \cdot \epsilon(t) \quad (4.6)$$

where $\epsilon(t)$ describes the acceptance of the D meson as a function of proper time t and N_D , τ_D , N_{bg} and τ_{bg} are free parameters of the fit. The constant C was set to zero for D^+ and D_s^+ fits while, in the case of the D^0 life time fit, it was a free parameter. We assumed the same acceptance both for signal and background events and exponential distribution of proper time also for the background.

The acceptance was determined from the Monte Carlo simulation separately for each target wire and particle anti-particle species, then averaged over particle/anti-particle and over the wires as explained in section 5.2. The acceptances are plotted in Fig. 4.9.

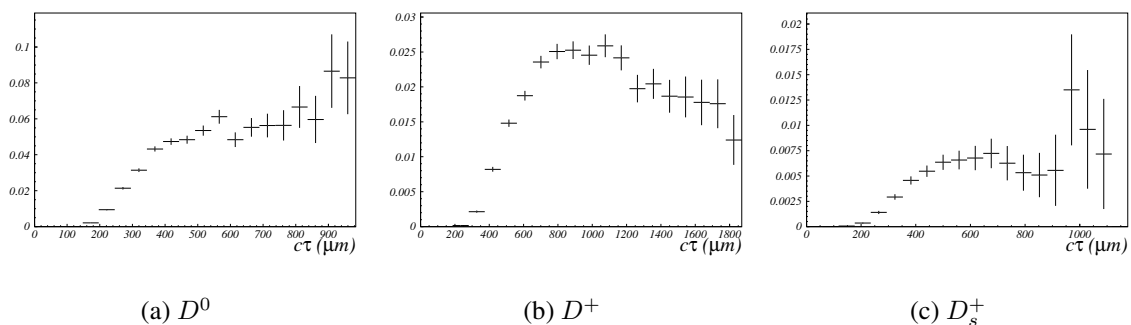


Figure 4.9: Acceptance in proper life time for (a) D^0 , (b) D^+ , (c) D_s^+ .

We fitted simultaneously the signal window distribution with $S(t) + B(t)$ and the sidebands distribution with $B(t)$. The number of free parameters was four in the cases of D^+ and D_s^+ and five for D^0 . The results of fits are shown in Figs. 4.10, 4.11 and 4.12. Four histograms are shown in each figure: at the top the acceptance uncorrected distributions for signal window and for side bands and at the bottom the acceptance corrected distributions for the signal

meson	measured $c\tau$ [μm]	$\chi^2/n.d.f$	world average $c\tau$ [μm]
D^+	302 ± 33	36/19	311.8
D^0	120 ± 13	36/24	122.9
D_s^+	165 ± 52	6.2/7	149.9

Table 4.5: Measured D meson life times

(=signal window with side bands subtracted) and the background (=side bands). The acceptance corrected distributions for the signals (bottom left plots) are in good agreement with the exponential distribution.

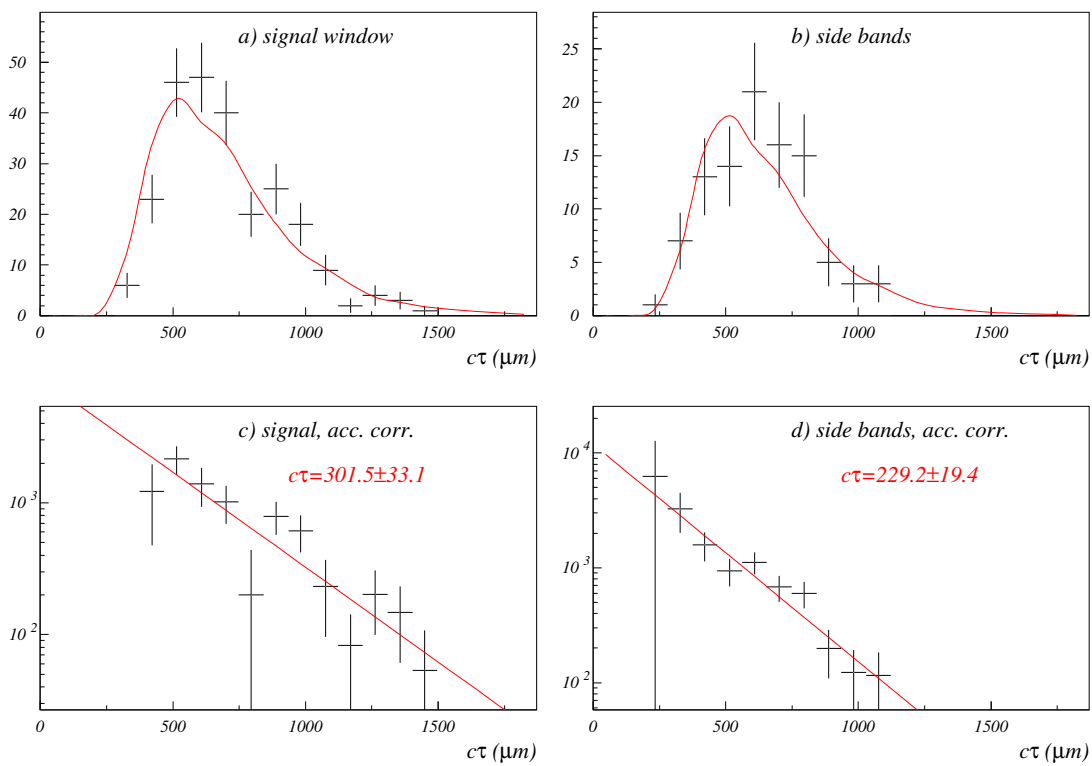


Figure 4.10: Simultaneous maximum likelihood fit to the D^+ proper time distributions

Our measurement of the life times, the χ^2 of the simultaneous fit and the world average [11] of the life times are summarized in Table 4.5. The results for all three mesons are in good agreement with the world average.

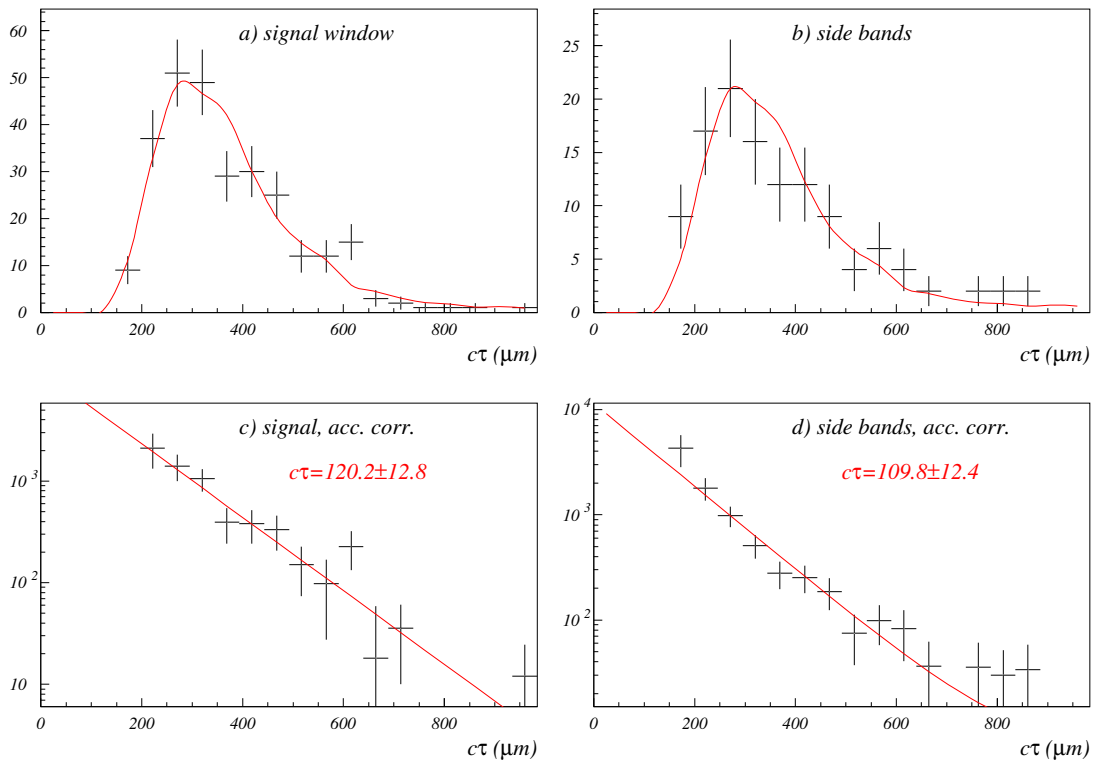


Figure 4.11: Simultaneous maximum likelihood fit to the D^0 proper time distributions

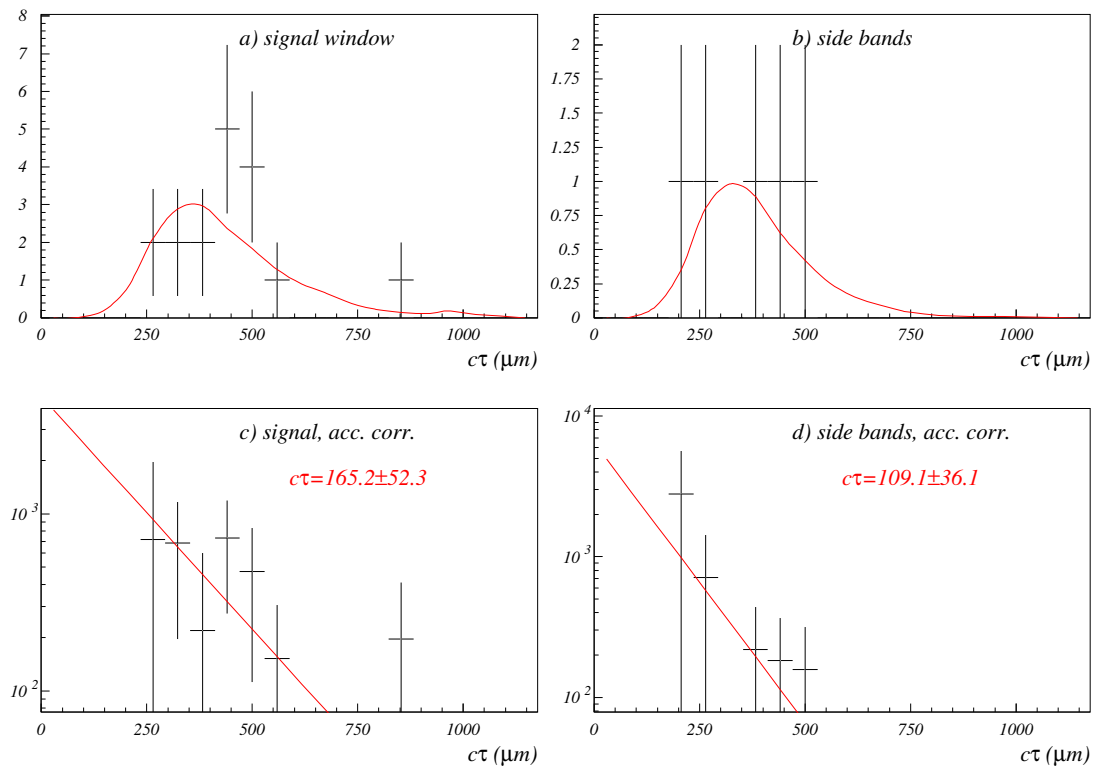


Figure 4.12: Simultaneous maximum likelihood fit to the D_s^+ proper time distributions

4.6 Other consistency checks

The D_s^+ and D^{*+} are reconstructed in the decays via intermediate states ϕ and D^0 respectively. Intermediate states should be visible in the corresponding invariant mass distributions, when the signal region in the initial state invariant mass distribution is selected, and the fit to the intermediate state invariant mass distribution should give the number of events consistent with the number in the initial state peak^{††}. The invariant mass distributions are shown in Fig. 4.13. Both intermediate states can be clearly seen.

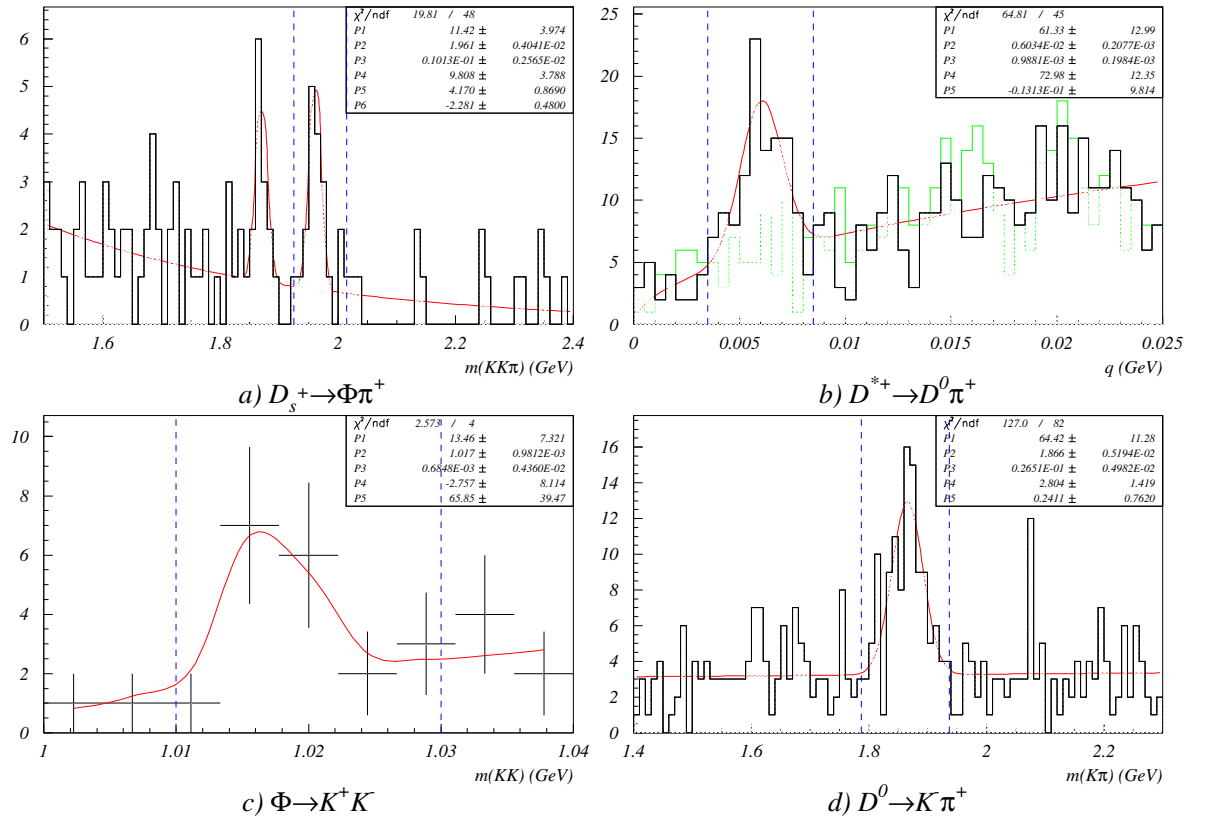


Figure 4.13: Invariant mass distributions for initial (top) and intermediate states (bottom): (a) $D_s^+ \rightarrow \phi \pi^+$, (b) $D^{*+} \rightarrow D^0 \pi^+$, (c) $\phi \rightarrow K^- K^+$, events within D_s^+ peak and (d) $D^0 \rightarrow K^- \pi^+$, events within D^{*+} peak. The signal regions used for the complementary plots are marked with vertical dashed lines. In (b) the wrong sign combinations (\bar{D}^0, π^+) are also plotted (in green).

In the case of D_s^+ the fit gives 13.5 ± 7.3 decays $\phi \rightarrow K^+ K^-$, while in the D_s^+ peak we have 11.4 ± 4.0 events. The numbers are in good agreement. We fitted the ϕ invariant mass with a Bright-Wigner equation convoluted with a Gaussian plus a background of the form

^{††}It could be slightly larger, since a fraction of the background in the initial state signal region is due to random combinations of the intermediate state and a pion from some other sources

$a \cdot \sqrt{m - 2m_K} + b \cdot (m - 2m_K)$, where m_K is the kaon mass. The position of the Breit-Wigner equation and the width of the Gaussian were also free parameters of the fit.

Good agreement was also found for the D^{*+} : 64.4 ± 11.3 events in the D^0 peak and 61.3 ± 12.9 events in the D^{*+} peak. The D^0 background was fitted with a linear function.

Two other checks were done for the D_s^+ signal: the angular distribution of pions with respect to kaons in the rest frame of the ϕ and the consistency of the $D^+ \rightarrow \phi\pi^+$ peak. The angular distribution is shown in Fig. 4.14. It agrees well with the theoretically required $\cos^2 \theta_{K\pi}$ dependence. A similarly good agreement was found also for the D^+ peak. The data points were obtained by fitting the invariant mass distribution of $K^-K^+\pi^+$ combinations in three bins of $|\cos \theta_{K\pi}|$. The position and the width of the signal were fixed.

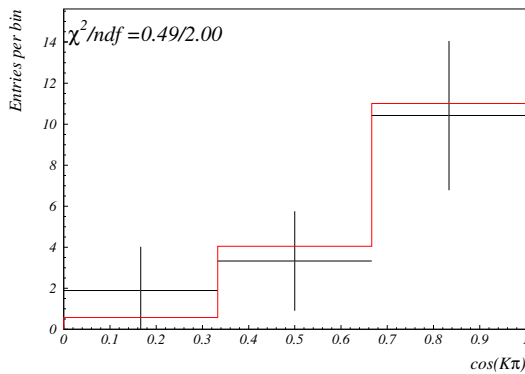


Figure 4.14: The angular distribution of pions with respect to kaons in the rest frame of ϕ for D_s^+ signal events. The $\cos^2 \theta_{K\pi}$ dependence of the $dN/d\cos \theta_{K\pi}$ distribution is plotted in red and is normalized to the same number of events as the data. The χ^2 is also given.

The consistency of the $D^+ \rightarrow \phi\pi^+$ signal was tested by estimating the number of reconstructed decays from the measured D^+ cross section in the $D^+ \rightarrow K^-\pi^+\pi^+$ decay channel given in Table 5.4 of section 5.3. The efficiency was determined from the $c\bar{c}$ Monte Carlo simulation and amounts to $0.99 \pm 0.25\%$. By taking the branching fraction of $0.32 \pm 0.03\%$ [11] and the luminosities from Table 3.2 we estimated the number to 4.2 ± 1.2 . The fit to data gives 9.8 ± 3.8 , which is in reasonable agreement with the estimated number (the χ^2 probability is 16%).

5 Total visible production cross sections

In this section the total visible production cross sections are evaluated from the selected D meson data samples discussed in the previous section. The efficiencies are determined from the signal Monte Carlo simulation, without any corrections to the generated kinematical distributions. The corrections are made later in section 8, after discussion of the kinematical distributions.

5.1 Basic formulae

The visible cross section per nucleus, i.e. the cross section measured in the HERA-B visible range of $-0.15 < x_F < 0.05$ is given by

$$\Delta\sigma_{pA} = \frac{N_i}{Br \cdot \epsilon_i \cdot \mathcal{L}_i} \quad (5.1)$$

where N_i is the number of reconstructed D mesons, ϵ_i and \mathcal{L}_i are the efficiency and integrated luminosity for a particular target and Br the branching ratio for a specific decay channel. The cross section for D meson production on a nuclear target of atomic number A is parameterized as

$$\sigma_{pA} = \sigma_{pN} \cdot A^\alpha \quad (5.2)$$

Since the statistics of the D meson data samples is relatively poor, we fitted invariant mass distributions for the total D meson data samples and extracted the production cross sections per nucleon $\Delta\sigma_{pN}$ in the following way. From Eqs. 5.1 and 5.2 we get for the D meson yield of the target i

$$N_i = Br \cdot \epsilon_i \cdot \mathcal{L}_i \cdot \Delta\sigma_{pN} \cdot A_i^\alpha \quad (5.3)$$

By summing Eq. 5.3 over all targets and solving it for the production cross section we get

$$\Delta\sigma_{pN} = \frac{N}{Br \cdot \sum_i \epsilon_i \mathcal{L}_i A_i^\alpha} \quad (5.4)$$

where $N = \sum_i N_i$ is the measured D meson yield of the total data sample. The sum in the denominator of Eq. 5.4 can be rewritten by introducing the average efficiency ϵ , defined by the

weighted sum:

$$\epsilon = \sum_i p_i \epsilon_i, \quad p_i = \frac{A_i^\alpha \mathcal{L}_i}{\sum_k A_k^\alpha \mathcal{L}_k} \quad (5.5)$$

Then Eq. 5.4 reads

$$\Delta\sigma_{pN} = \frac{N}{Br \cdot \epsilon \cdot \sum_i \mathcal{L}_i A_i^\alpha} \quad (5.6)$$

Alternatively, we can calculate the cross sections per nucleon individually for each target and then calculate the weighted average by using measurement errors. It can be shown (see ref. [43]) that Eq. 5.6 is a result of the Poissonian likelihood fit to the target subsamples while the weighted average corresponds to the least square fit. In this respect the results obtained with Eq. 5.6 are statistically more correct than the weighted average.

Since there is no experimental clue for nuclear effects, we assumed a linear A dependence of the production cross sections and set $\alpha = 1$ in Eqs. 5.5 and 5.6.

5.2 Efficiency determination

The efficiencies were determined from the signal Monte Carlo simulation. The events were processed with the same code and analyzed using the same analysis cuts as for the real data. The efficiencies were calculated separately for particles and anti-particles and for each target wire by

$$\epsilon_i^{+/-} = \frac{n_i^{+/-}}{N_i^{+/-}} \quad (5.7)$$

where $n_i^{+/-}$ and $N_i^{+/-}$ are the numbers of reconstructed and generated decays respectively in the visible x_F range for the target wire i and particle (+) or anti-particle (-). The generated decays were counted by identifying the D meson decays in the corresponding data structure of a simulated event* Thus the numbers given in Table 3.4 are for a few percent larger than the numbers of generated events, because they also include the decays of the charge conjugate particles into the channel of interest.

The reconstructed decays were counted by fitting the invariant mass distributions with a Gaussian for the signal and a constant (D^0 , D_s^+) or a linear function (D^+) for the background. The background in the Monte Carlo simulation is much smaller than in the real data. The fit range was limited to 150 MeV around the nominal mass to reduce the systematics due to background parameterization. The exception was D^{*+} where we used the same background

*the table MTRA and using the ARTE relations between mother and daughter particles.

meson	b1 (C)	i1 (W)	b2 (Ti)	i2 (C)
D^0	1.324 ± 0.045	1.363 ± 0.040	1.385 ± 0.060	1.265 ± 0.056
\bar{D}^0	1.336 ± 0.037	1.452 ± 0.039	1.609 ± 0.055	1.354 ± 0.051
D^+	1.121 ± 0.042	1.139 ± 0.038	1.288 ± 0.058	1.089 ± 0.055
D^-	1.171 ± 0.037	1.151 ± 0.033	1.299 ± 0.048	1.144 ± 0.047
D_s^+	0.432 ± 0.040	0.412 ± 0.038	0.381 ± 0.051	0.537 ± 0.092
D_s^-	0.400 ± 0.033	0.365 ± 0.028	0.469 ± 0.045	0.352 ± 0.043
D^{*+}	1.345 ± 0.042	1.318 ± 0.035	1.379 ± 0.059	1.293 ± 0.058
D^{*-}	1.560 ± 0.038	1.575 ± 0.032	1.735 ± 0.056	1.488 ± 0.053

Table 5.1: Reconstruction efficiencies in % for individual targets

sample	D^0	D^+	D_s^+	D^{*+}
total	1.388 ± 0.017	1.160 ± 0.016	0.405 ± 0.015	1.456 ± 0.016
particle	1.346 ± 0.025	1.147 ± 0.024	0.426 ± 0.025	1.330 ± 0.023
anti-particle	1.431 ± 0.024	1.173 ± 0.021	0.385 ± 0.018	1.581 ± 0.021
C	1.325 ± 0.024	1.138 ± 0.023	0.423 ± 0.023	1.436 ± 0.023
W	1.407 ± 0.028	1.145 ± 0.025	0.389 ± 0.023	1.447 ± 0.024
Ti	1.497 ± 0.041	1.294 ± 0.038	0.425 ± 0.034	1.557 ± 0.041
golden	1.396 ± 0.019	1.166 ± 0.017	0.403 ± 0.016	1.464 ± 0.017
non-golden	1.364 ± 0.021	1.139 ± 0.019	0.415 ± 0.024	1.428 ± 0.020

Table 5.2: Reconstruction efficiencies in % for different data samples

parameterization as in the real data and fitted in the same range. For all distributions a maximum likelihood fit was used.

The efficiencies per targets are summarized in Table 5.1. The efficiencies for the total sample and the subsamples, summarized in Table 5.2, were calculated from the efficiencies per targets (Table 5.1) by using Eqs. 5.5 with $\alpha = 1$ and the luminosity data from Table 3.2. For the samples, where the charge state of a meson was not distinguished, we took the average of charge conjugate efficiencies for the efficiency of a target ϵ_i in Eq. 5.5

$$\epsilon_i = \frac{\epsilon_i^+ + \epsilon_i^-}{2} \quad (5.8)$$

5.3 Cross sections

Visible cross sections per nucleon $\Delta\sigma_{pN}$ were calculated with Eq. 5.6, by setting $\alpha = 1$, from the number of reconstructed events N given in Table 4.4, known branching fractions Br (Table 5.3), reconstruction efficiencies ϵ (Table 5.2) and integrated luminosities \mathcal{L}_i summed over

Branching fractions [%]			
$D^0 \rightarrow K^- \pi^+$	$D^+ \rightarrow K^- \pi^+ \pi^+$	$D_s^+ \rightarrow \phi \rightarrow K^+ K^- \pi^+$	$D^{*+} \rightarrow D^0 \rightarrow K^- \pi^+ \pi^+$
3.80 ± 0.07	9.51 ± 0.34	2.16 ± 0.28	2.57 ± 0.05

Table 5.3: Branching fractions [11]

$\Delta\sigma_{pN}$ [μb]				
sample	D^0	D^+	D_s^+	D^{*+}
total	26.3 ± 2.5	10.7 ± 1.1	10.4 ± 3.6	13.0 ± 2.8
particle	11.8 ± 1.7	4.0 ± 0.7	4.2 ± 2.3	4.9 ± 1.5
anti-particle	14.5 ± 1.7	6.6 ± 0.8	6.4 ± 2.7	7.9 ± 1.6
C	29.2 ± 4.3	10.9 ± 1.7	10.2 ± 5.5	16.0 ± 3.8
W	26.2 ± 3.3	11.0 ± 1.5	12.1 ± 5.5	10.1 ± 3.0
Ti	20.7 ± 6.7	9.2 ± 2.9	3.1 ± 7.6	16.2 ± 6.8
gold	26.0 ± 2.7	10.8 ± 1.2	8.9 ± 3.9	15.2 ± 2.7
non-gold	27.6 ± 5.2	10.2 ± 2.2	14.3 ± 7.8	5.9 ± 3.7

Table 5.4: Visible production cross sections per nucleon (uncorrected) with statistical errors from the fits to real data invariant mass distributions.

nucleons $\sum_i \mathcal{L}_i A_i$ (Table 3.2). The results are summarized in Table 5.4. In Fig. 5.1 we plot the cross sections of five subsamples (C, Ti, W, golden and non-golden) and compare them to the cross section of the total sample, represented by the dashed line. With the exception of the non-golden subsample of D^{*+} , for which the cross section is for two standard deviations smaller, all other subsample cross sections agree within one standard deviation with the cross section of the total sample.

5.4 Leading to non-leading particle asymmetries

The leading particle is defined as the one which has a light quark in common with the beam particle. Thus the leading particles are anti- D mesons \bar{D}^0 , D^- and D^{*-} , while both charge conjugates of the D_s^+ are, according to the definition, the non-leading particles. The leading to non-leading particle asymmetry is defined as a relative difference of the cross sections

$$A = \frac{\sigma_{LP} - \sigma_{nonLP}}{\sigma_{LP} + \sigma_{nonLP}} \quad (5.9)$$

The asymmetry depends on the fragmentation mechanism. The PYTHIA version with the settings used for the $c\bar{c}$ Monte Carlo simulation predicts slightly positive values for the asymmetry in the full phase space (9% for D^0 and 6% for D^+ or D^{*+}). PYTHIA also generates different shapes of the x_F distributions: narrower for anti-particles and wider for particles (see

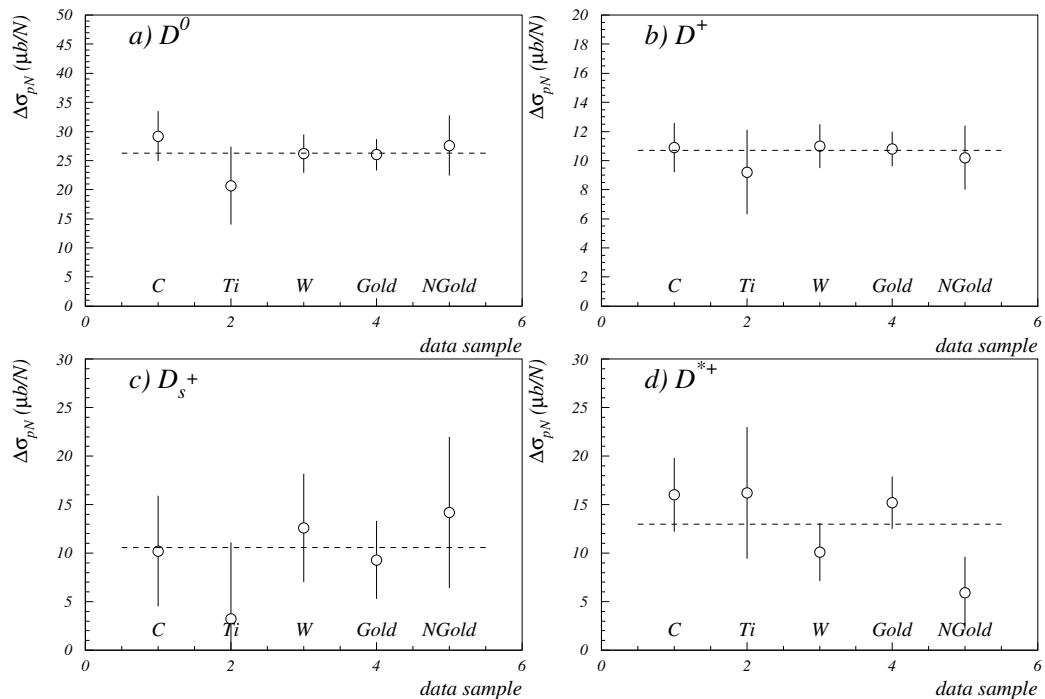


Figure 5.1: Comparison of the cross sections of the subsamples (points with error bars) with the cross section of the total sample (dashed line).

section 6.2). Thus the asymmetries measured in a limited x_F range are shifted to even more positive values. Note that for D_s^+ , where we only have non-leading particles, we use the same prescription for the above formula, and take its anti-particle D_s^- to be the leading particle. In this case the asymmetry is larger and negative (-25%), and reduces to -6% for the limited x_F range.

Our measurements determined from the cross sections given in Table 5.4 and PYTHIA predictions are summarized in Table 5.5. The predictions and the measurements are in good agreement. The weighted average of the D^0 , D^+ and D^{*+} asymmetries is 0.18 ± 0.06 ($\chi^2/n.d.f=1.4/2$), i.e. three standard deviations above the zero value and within one standard deviation of the PYTHIA prediction.

	D^0	D^+	D^{*+}	D_s^+
Measurement	0.10 ± 0.09	0.25 ± 0.10	0.24 ± 0.18	0.21 ± 0.33
PYTHIA	0.24	0.22	0.23	-0.06

Table 5.5: Leading to non-leading particle asymmetries in the range of $-0.15 < x_F < 0.05$. For the D_s^+ the anti-particle cross section was used for σ_{LP} in Eq. 5.9

$\Delta\sigma_{pA}$ [mb]				
target	D^0	D^+	D_s^+	D^{*+}
C	0.35 ± 0.05	0.13 ± 0.02	0.12 ± 0.07	0.19 ± 0.05 (0.23 ± 0.07)
Ti	0.99 ± 0.32	0.44 ± 0.14	0.15 ± 0.36	0.77 ± 0.33 (1.04 ± 0.54)
W	4.81 ± 0.61	2.02 ± 0.28	2.23 ± 1.01	1.86 ± 0.56 (2.30 ± 0.92)

Table 5.6: Visible cross sections per nucleus (uncorrected). Numbers in parenthesis of the last column are for the subsamples of D^{*+} with D^0 daughter not common to the D^0 samples of the first column.

5.5 A-dependence of cross sections

The dependence on the atomic number A of the target material is parameterized with Eq. 5.2. Since we reconstructed the D meson decays in the data samples of three different target materials, we could measure the exponent α in Eq. 5.2. We used two fitting methods: the least square fit of Eq. 5.2 to the cross sections per nucleus $\Delta\sigma_{pA}$ and the simultaneous maximum likelihood fit to the invariant mass distributions of individual material data samples. When we calculated the weighted average of parameter α for all four D meson samples, we took only those D^{*+} , for which the D^0 daughter particle was not reconstructed in the D^0 sample. In this case the number of reconstructed D^{*+} was 46 ± 12 and the visible cross-section $\Delta\sigma_{pN}=16.9\pm 4.6$ μb .

Least square fits Eq. 5.2 was fitted to the measured visible cross sections per nucleus $\Delta\sigma_{pA}$, calculated with Eq. 5.1 and summarized in Table 5.6. The data for N_i , Br , ϵ_i and \mathcal{L}_i in Eq. 5.1 with i being C, Ti or W was taken from Tables 4.4, 5.3, 5.2 and 3.2 respectively. The fitting was done in PAW [44] with the option “e”. The fits are shown in Fig. 5.2.

Simultaneous maximum likelihood fits With this method the invariant mass histograms for C, Ti and W data samples were fitted simultaneously using the binned maximum likelihood fit (option “le” in PAW). The signals were parameterized with a Gaussian, normalized to the number of events N_i given by Eq. 5.3

$$S_i(m) = \frac{Br \cdot \epsilon_i \cdot \mathcal{L}_i \cdot \Delta\sigma_{pN} \cdot A_i^\alpha}{\sqrt{2\pi}\sigma_m} e^{-\frac{(m-m_0)^2}{2\sigma_m^2}}, \quad i = C, Ti, W \quad (5.10)$$

The free parameters are the exponent α , the cross section $\Delta\sigma_{pN}$, the peak position m_0 and the width σ_m , and are common to all three data samples. The branching ratio Br , the three efficiencies ϵ_i , integrated luminosities \mathcal{L}_i and the atomic numbers A_i were taken from Tables 5.3, 5.2 and 3.2 respectively.

The backgrounds were parameterized similarly to the fits of total data samples. For D^0 , D^+ and D_s^+ the combinatorial backgrounds were parameterized by an exponential

$$B_i^{exp}(m) = e^{a_i+b\cdot m}, \quad i = C, Ti, W \quad (5.11)$$

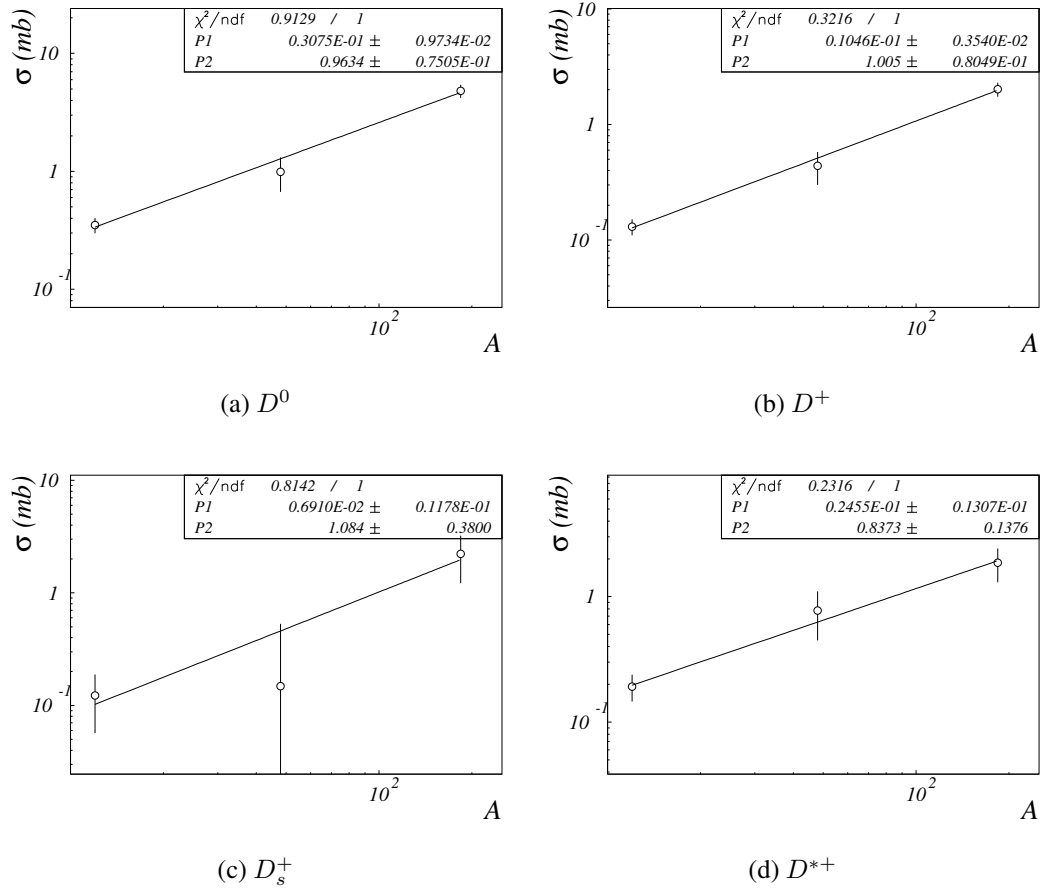


Figure 5.2: A-dependence least square fits to cross sections per nucleus from Table 5.6

with free parameters a_C , a_{Ti} , a_W describing the normalization and b describing the shape of the background. The parameter b is common to all three samples. The charm background in the D^0 invariant mass was parameterized as

$$B_i^{cc}(m) = \epsilon_i^{cc} \cdot \mathcal{L}_i \cdot \sigma_{cc} \cdot A_i^\alpha \cdot B_{cc}(m) , \quad i = C, Ti, W \quad (5.12)$$

with the free parameter σ_{cc} common to all three subsamples and α the same as in Eq. 5.10. The efficiencies ϵ_i^{cc} were determined from the $c\bar{c}$ Monte Carlo simulation as well as the normalized shape $B_{cc}(m)$ of this background.

The peak of the D^+ in the D_s^+ invariant mass was parameterized with the Gaussian of fixed position and width (1.869 GeV, 15 MeV) and with the normalization

$$N_i^{D^+} = \epsilon_i \cdot \mathcal{L}_i \cdot s \cdot A_i^\alpha , \quad i = C, Ti, W \quad (5.13)$$

where the free parameter s is common to all three subsamples and the α same as in Eq. 5.10.

Particle	α	
	least square	likelihood
D^0	0.963 ± 0.075	0.969 ± 0.057
D^+	1.005 ± 0.080	1.005 ± 0.078
D_s^+	1.084 ± 0.380	1.168 ± 0.210
D^{*+}	0.837 ± 0.138	0.832 ± 0.138
	(0.849 ± 0.179)	(0.847 ± 0.185)
Average	0.975 ± 0.052	0.982 ± 0.044

Table 5.7: A-dependency parameter α from the least square and from the simultaneous maximum likelihood fits and a weighted average for all four D mesons. For the weighted average the numbers in parenthesis of the fifth row were used. These numbers are for the subsample of D^{*+} with D^0 daughter not common with the D^0 sample.

The parameter s is proportional to the D^+ cross section. Unfortunately, the statistics of the $c\bar{c}$ Monte Carlo simulation is too low for the determination of $D^+ \rightarrow \phi\pi^+$ efficiencies ϵ_i . We approximated them with the values for the D_s^+ decay obtained from the signal Monte Carlo simulation.

The background in D^{*+} invariant mass was parameterized as

$$B_i(q) = a_i(q^{1/2} + bq^{3/2}) \quad , \quad i = C, Ti, W \quad (5.14)$$

again with free parameters a_C, a_{Ti}, a_W and parameter b common to all three samples.

To summarize, the number of free parameters was 8 for D^+ and D^{*+} ($\alpha, \Delta\sigma_{pN}, m_0, \sigma_m, a_C, a_{Ti}, a_W, b$), and 9 for D^0 and D_s^+ ($\alpha, \Delta\sigma_{pN}, m_0, \sigma_m, a_C, a_{Ti}, a_W, b, \sigma_{cc}$ or s). The fits are shown in Fig. 5.3.

The results from both methods are summarized in Table 5.7. Both methods gave very similar results, but the errors from the maximum likelihood fits are smaller. Our result, $\alpha = 0.98 \pm 0.04$ is compatible with a linear dependence of cross sections and also with the result of E789 [17], $\alpha = 1.02 \pm 0.03 \pm 0.02$.

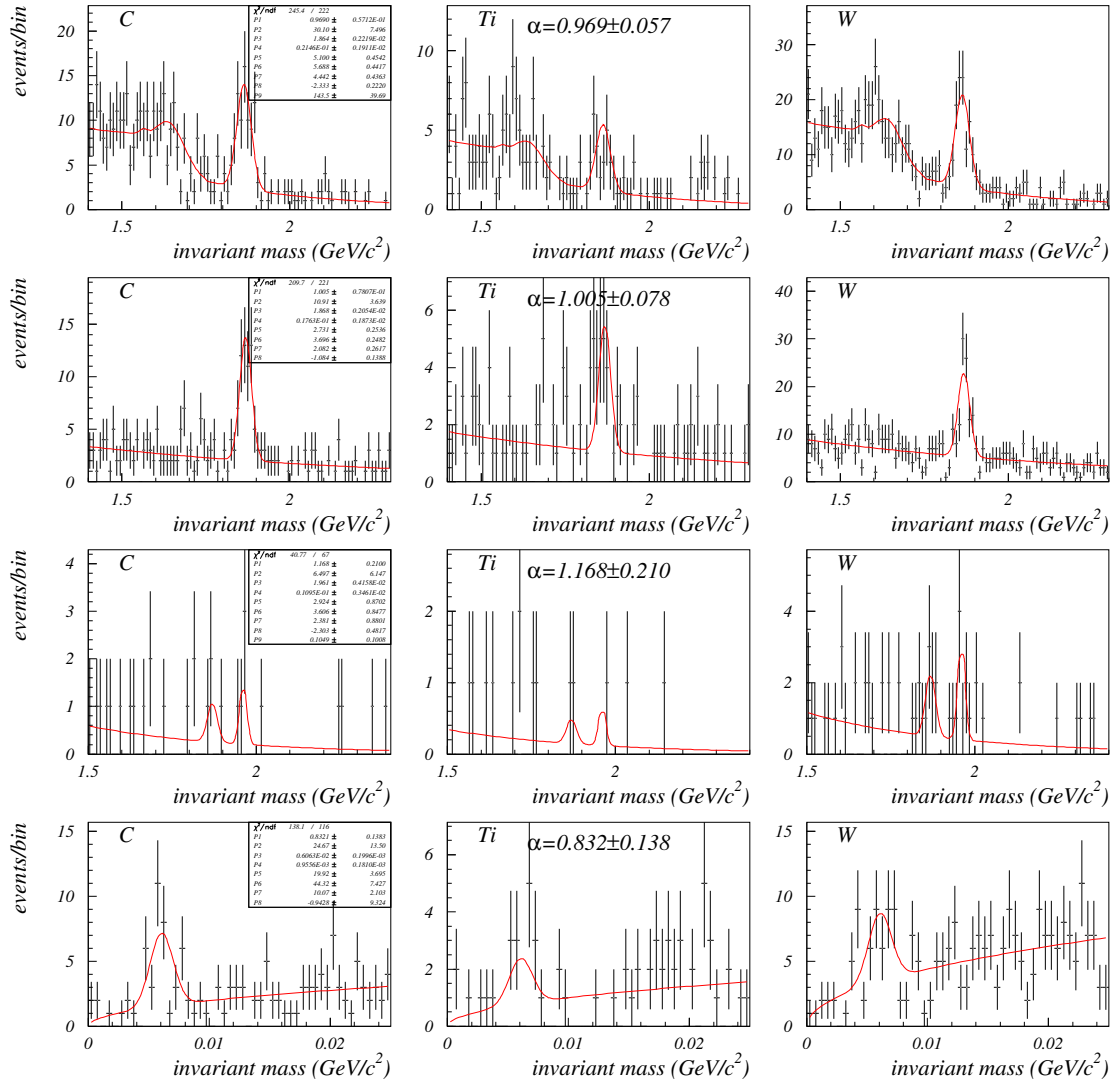


Figure 5.3: A-dependence simultaneous maximum likelihood fits. From top to bottom: invariant masses of C (left), Ti (middle) and W (right) samples for D^0 , D^+ , D_s^+ and D^{*+} mesons.

6 Kinematical distributions

With the statistics of about 400 reconstructed D mesons we are not able to measure the two dimensional distribution in momentum space, $d^2\sigma/\pi dp_T^2 dx_F$, but only its projections $d\sigma/dp_T^2$ and $d\sigma/dx_F$. Furthermore the phase space (p_T, x_F) is limited by the detector acceptance to the band along p_T with the width of $-0.15 < x_F < 0.05$. This band contains, according to PYTHIA, about 45% of D mesons.

6.1 Parameterization of distributions

6.1.1 Transverse momentum

For the transverse momentum distribution the following parameterizations have been found in the literature

$$\frac{d\sigma}{dp_T^2} \propto e^{-bp_T^2} \quad (6.1)$$

$$\frac{d\sigma}{dp_T^2} \propto e^{-b'p_T} \quad (6.2)$$

$$\frac{d\sigma}{dp_T^2} \propto (\alpha m_c^2 + p_T^2)^{-\beta} \quad (6.3)$$

The exponential parameterization in p_T^2 (Eq. 6.1) was used by most experiments, but was found by E769 [12] to describe the measurements well only for transverse momenta below 1 GeV/c. Above 1 GeV/c the distribution becomes more like exponential in p_T (Eq. 6.2). The last parameterization by Eq. 6.3 was introduced by Frixione [1] and fits the data of E769 well over the entire p_T range. The mass of the c quark m_c in Eq. 6.3 is usually set to 1.5 GeV and the other two parameters α and β are being free in a fit. We found that the errors of the parameters α and β given by the fit are highly correlated and large. The parameterization by Eq. 6.3 can be rewritten in the form used by the HERA-B vector meson analysis [46]: $(1 + (\frac{p_T}{p_0})^2)^{-\beta}$. Also in this parameterization the correlation between parameters p_0 and β remains large. By replacing p_0 with the mean transverse momentum of the distribution $\langle p_T \rangle$ the parameterization reads

$$\frac{d\sigma}{dp_T^2} \propto [1 + (\frac{\sqrt{\pi} \Gamma(\beta - \frac{3}{2}) p_T}{2 \Gamma(\beta - 1) \langle p_T \rangle})^2]^{-\beta} \quad (6.4)$$

With this parameterization the correlation between the errors of $\langle p_T \rangle$ and β is small. The Eq. 6.4 is more suitable for fitting the data than Eq. 6.3.

Eq. 6.4 with the fixed exponent $\beta = 6$ is usually used for the parameterization of the J/ψ transverse momentum distribution and reads

$$\frac{d\sigma}{dp_T^2} \propto [1 + (\frac{35\pi p_T}{256\langle p_T \rangle})^2]^{-6} \quad (6.5)$$

It could easily be shown that for large exponents ($\beta \rightarrow \infty$) Eq. 6.4 limits towards Eq. 6.1 with parameters $\langle p_T \rangle$ and b related by $b = \frac{\pi}{4} \frac{1}{\langle p_T \rangle^2}$.

6.1.2 Feynman's x variable

Usually the x_F distribution is parameterized with a power-law function:

$$\frac{d\sigma}{dx_F} \propto (1 - |x_F|)^n \quad (6.6)$$

When compared to the predictions from next-to-leading order QCD calculations this function does not reproduce the central region well [18]. The experimental observation made by E791 [45] in 500 GeV π -A collisions using high statistics of 80k reconstructed D^0 also shows a similar discrepancy. They fitted their data with a function which is an extension of Eq. 6.6 and which uses a power-law function in the tail region and a Gaussian in the central region [†]

$$\frac{d\sigma}{dx_F} = \begin{cases} Ae^{-\frac{x_F^2}{2\sigma_g^2}} & , |x_F| < x_b \\ A'(1 - |x_F|)^n & , |x_F| \geq x_b \end{cases} \quad (6.7)$$

To ensure a continuity of the function and its first derivative at $|x_F| = x_b$, the parameters σ_g and the ratio A/A' are related by

$$\sigma_g = \sqrt{\frac{x_b(1 - x_b)}{n}} \quad (6.8)$$

$$\ln \frac{A}{A'} = n \left(\frac{x_b}{2(1 - x_b)} + \ln(1 - x_b) \right) \quad (6.9)$$

Thus the parameterization by Eq. 6.7 has two free parameters, the exponent n and the boundary variable x_b . The experiment E791 [45] measurement for the boundary variable is $x_b = 0.062 \pm 0.013$.

[†]Since in the p-A collisions the distribution should be symmetrical, we omitted the offset parameter from their original parameterization

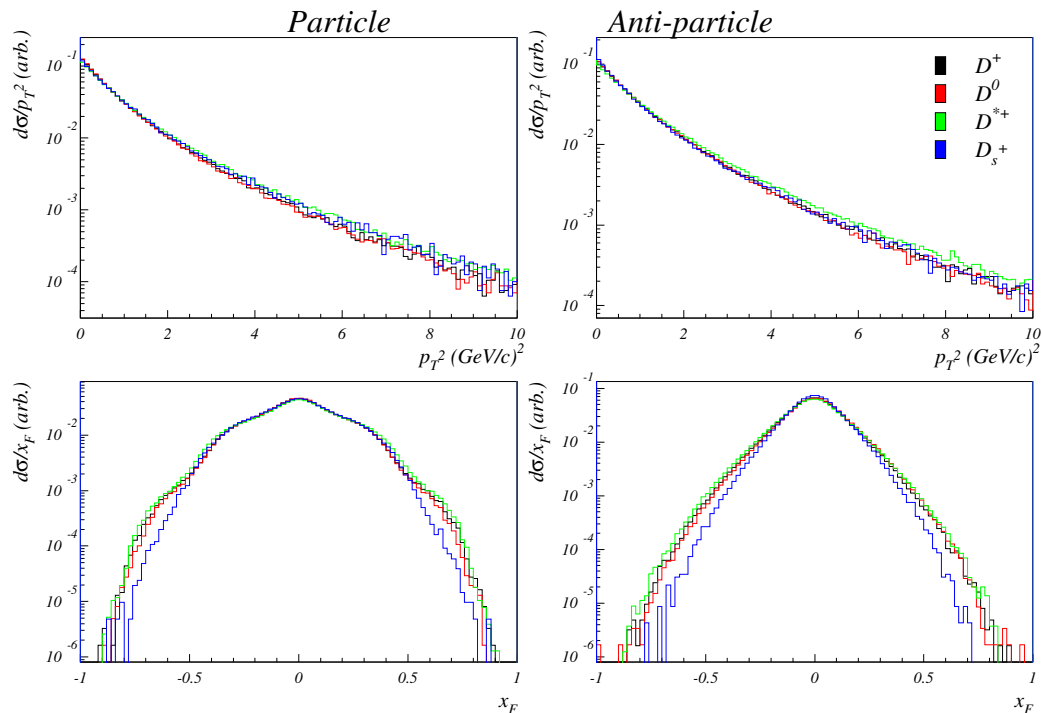


Figure 6.1: Comparison of kinematical distributions of D mesons in the Monte Carlo simulation.

6.2 Generated distributions with the Monte Carlo simulation

We compared the kinematical distributions from the Monte Carlo simulation, looking for possible differences between different D mesons, their charge conjugate states and the target materials on which they are produced. We found no difference between the distributions for different targets and only a small difference between distributions for D mesons of equal charge (see Fig. 6.1). The only noticeable is the narrower distribution in x_F for the D_s^+ .

The differences are larger between the charge conjugate states. The largest are the differences in the x_F distributions, which for anti-particles are narrower and smoother. Different also are the mean p_T values, which are larger for anti-particles by 8%.

The parameterizations from the previous section were fitted to kinematical distributions obtained from the Monte Carlo simulation. The p_T distribution of events within $-0.15 < x_F < 0.05$ is best fitted by the parameterization with $\langle p_T \rangle$ and β given by Eq. 6.4 and the worst with the exponential form of Eq. 6.1. The fits are shown in Fig. 6.2. Also shown is the parameterization of Eq. 6.2 which fits well only for $p_T > 1$ GeV/c and the parameterization with $\langle p_T \rangle$ and the exponent $\beta = 6$, which would fit low statistics data reasonably well.

The x_F distributions obtained from the Monte Carlo simulation were fitted with Eqs. 6.6 and 6.7. The fits are shown in Fig. 6.3. The power-law parameterization, Eq. 6.6 does not reproduce the central region well, while the extended parameterization Eq. 6.7 fits it well. The boundary parameter value from the fit is $x_b = 0.055$ and is consistent with $x_b = 0.062 \pm 0.013$ measured

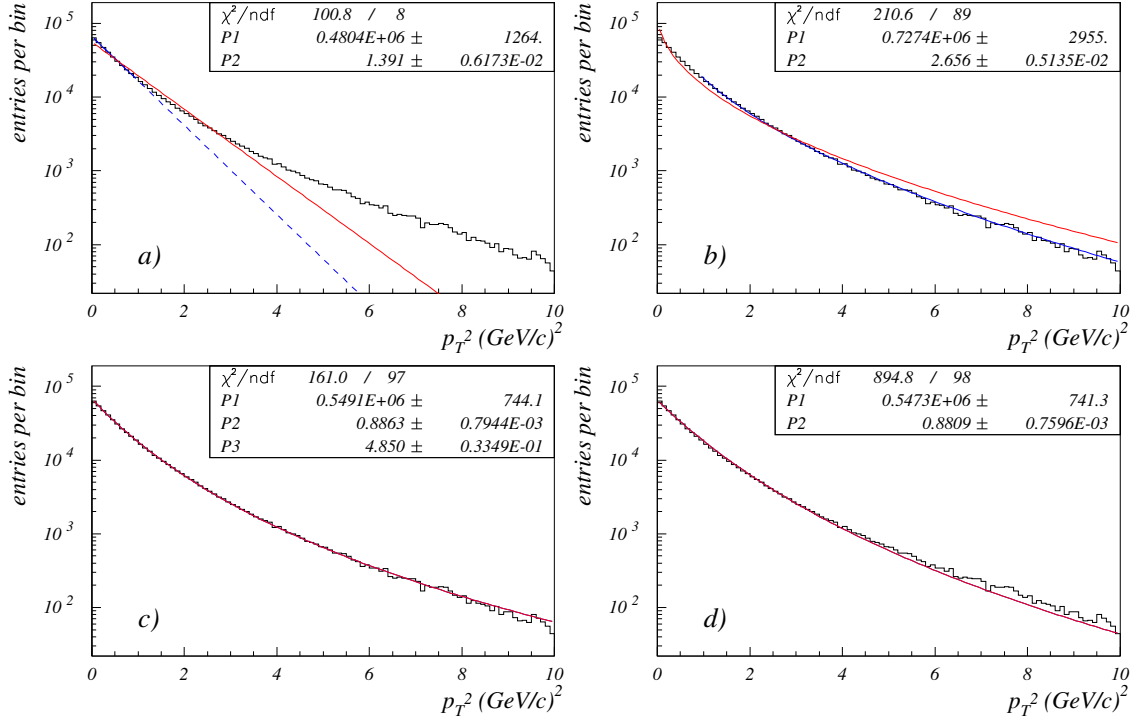


Figure 6.2: Fits of p_T^2 distribution from D^+ the Monte Carlo simulation with different parameterizations: a) Eq. 6.1, b) Eq. 6.2, c) Eq. 6.4 and d) Eq. 6.5. With blue curves in a) and b) fits in the ranges $p_T^2 < 1 \text{ GeV/c}$ and $p_T^2 > 1 \text{ GeV/c}$ respectively are shown.

$d\sigma/dp_T^2$		$d\sigma/dx_F$	
$\langle p_T \rangle$	β	n	x_b
0.898	4.80	5.42	0.052

Table 6.1: Fitted parameters for D meson mixtures.

by E791.

With the parameterization of Eq. 6.7 we fitted separately the distributions for both charge conjugate states of D^+ (Fig. 6.4). The fitted exponent n is quite different. The values are 4.4 for particles and 7.1 for anti-particles. The distributions for particles also show “shoulders” at $x_F = \pm 0.3$, which are not modelled with the parameterization.

We also checked the fitting in the range of $-0.10 < x_F < 0.05$. The boundary parameter was fixed to $x_b = 0.062$ of E791, since the fitting range is too small for having this parameter free. The fit resulted in $n = 5.6$ while the result in the wide range of $-0.6 < x_F < 0.6$ is $n = 5.4$. The fit with the power-law gave a considerably smaller value of $n = 4.4$.

Finally we fitted the distributions for a mixture of D mesons, corresponding to that in the real data for the measurements of $d\sigma/dp_T^2$ and $d\sigma/dx_F$. Fits with Eq. 6.4 for the p_T^2 and with Eq. 6.7 for the x_F distributions are shown in Fig. 6.5. The parameter values from the fits are summarized in Table 6.1.

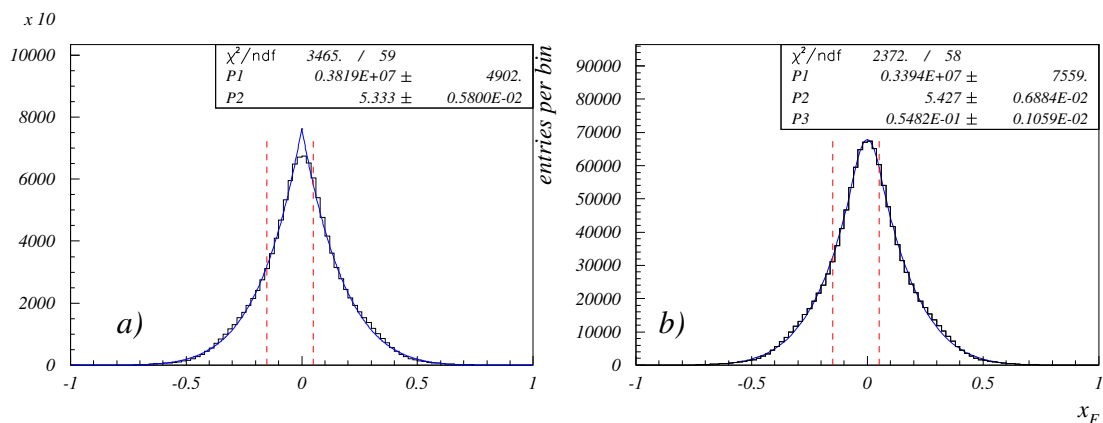


Figure 6.3: Fits of x_F distribution from D^+ the Monte Carlo simulation with different parameterizations: a) Eq. 6.6 and b) Eq. 6.7, both fitted in the range $-0.6 < x_F < 0.6$. With vertical dashed lines the visible range is indicated.

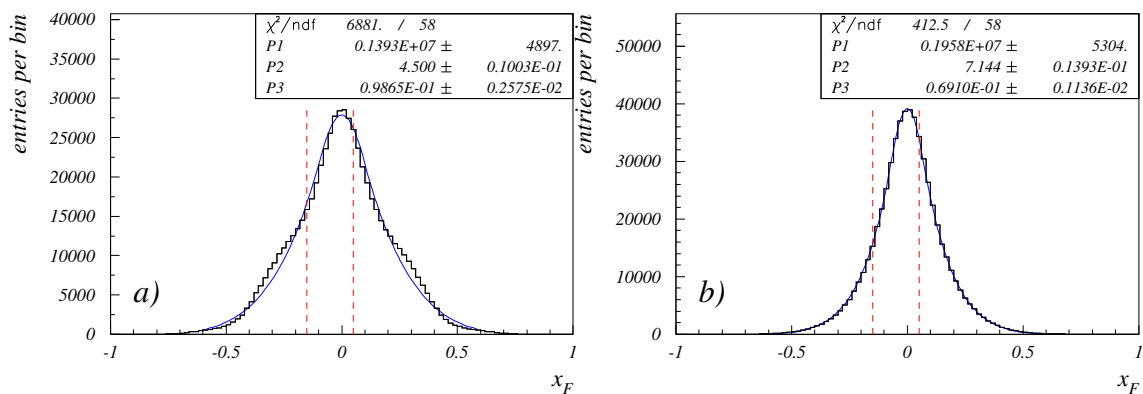


Figure 6.4: Fits of x_F distribution from D^+ the Monte Carlo simulation for a) D^+ and b) D^- mesons. Fitted with Eq. 6.7 in the range $-0.6 < x_F < 0.6$. With vertical dashed lines the visible range is indicated.

6.3 Acceptances

The acceptances were determined in bins of p_T^2 and x_F from the signal Monte Carlo simulation with the method explained in section 5.2. The only difference was in the method of counting the reconstructed decays, where we did not fit the invariant mass distributions, but instead counted the events in the signal window and subtracted the counts in side bands, or for D^{*+} subtracted the wrong sign combinations in the signal window.

The acceptances in p_T^2 , presented in Fig. 6.6, show a quadratic dependence for D^0 and D_s^+ , a linear for D^+ , while the acceptance of D^{*+} is slightly more complicated. We fitted it with the 3rd order polynomial. Since the acceptances are not constant in p_T , the total cross section measurements clearly depend on the assumed shape of the p_T distribution.

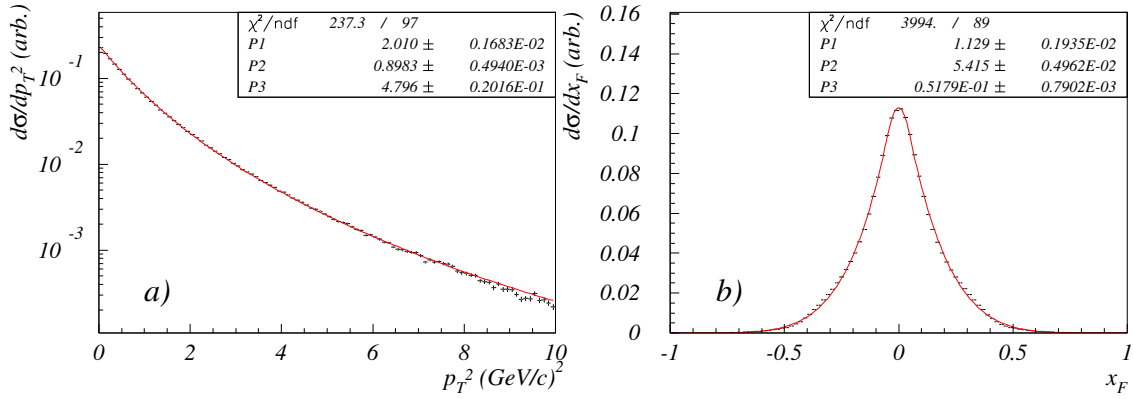


Figure 6.5: Fits to the normalized distributions of the mixture of D mesons: a) $d\sigma/dp_T^2$ for $D^0/D^+/D^{*+}$ mixture fitted with Eq. 6.4 and b) $d\sigma/dx_F$ for D^0/D^+ mixture fitted with Eq. 6.7.

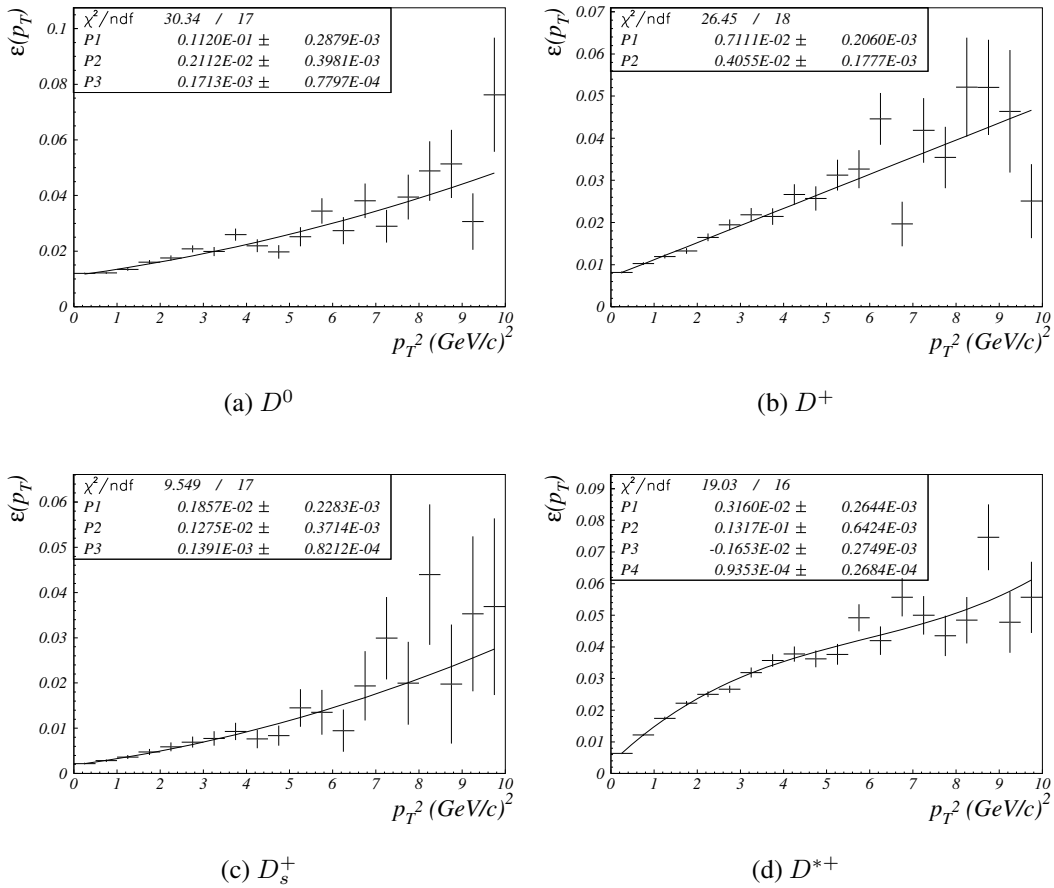
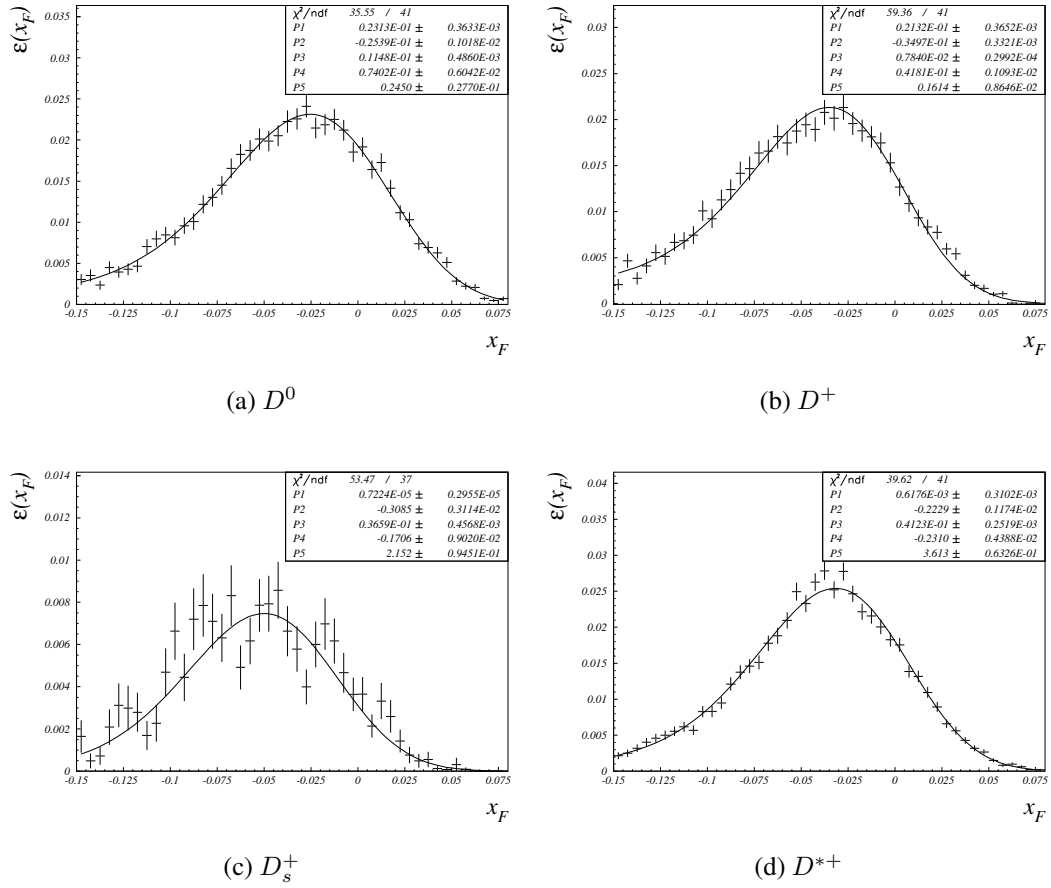


Figure 6.6: Acceptance in p_T^2

Figure 6.7: Acceptance in x_F

The acceptances in x_F are shown in Fig. 6.7. The data points were fitted with a function

$$\epsilon(x) = C e^{\frac{(x-x_0)^2}{2\sigma^2}}(A+Bx) \quad (6.10)$$

Contrary to the p_T^2 , the acceptances in x_F are limited to a relatively small central region, which is slightly shifted to the negative values of x_F . The maxima are at -0.03, except for the D_s^+ with the maximum at -0.05. For the visible range the interval of $-0.15 < x_F < 0.05$ was chosen for all four D mesons.

For the determination of $d\sigma/dp_T^2$ and $d\sigma/dx_F$ we used the fitted functions and not the data from bins.

6.4 Measurement of $d\sigma/dp_T^2$

To extract the parameters of a given parameterization of the $d\sigma/dp_T^2$ distributions we used a simultaneous maximum likelihood fit of events in the signal window and in the side bands. We fitted separately the D^0 , D^+ and D^{*+} data samples, as well as all three data samples simultaneously. The D_s^+ data sample was excluded, because of its low statistics. We fitted all four parameterizations, given by Eqs. 6.1, 6.2, 6.4 and 6.5.

The procedure was the same as that used for the life time fits in section 4.5. The events in the invariant mass signal window and the events in the side bands [‡] were first histogrammed in p_T^2 and then the histograms were simultaneously fitted. We had two histograms per D meson data sample: one for the events in the signal window and the other for the events in the side bands. The side bands were of the same size as the signal window and the size chosen was wide enough to include all signal events: ± 75 MeV for D^0 , ± 50 MeV for D^+ and ± 3 MeV for D^{*+} .

The number of D mesons in a given p_T^2 bin is according to Eq. 5.4 by taking $\alpha = 1$

$$N_D(p_T^2) = Br \cdot \epsilon(p_T^2) \cdot \sum_i \mathcal{L}_i A_i \cdot \frac{d\sigma}{dp_T^2} \Delta p_T^2 \quad (6.11)$$

where $\epsilon(p_T^2)$ is the acceptance, determined in the previous section from the Monte Carlo simulation, Δp_T^2 the bin size of the histograms and

$$\frac{d\sigma}{dp_T^2} = \Delta\sigma_{pN} P(p_T) \quad (6.12)$$

the parameterization of the differential cross section with one of the normalized functions of Eq. 6.1, 6.2, 6.4 or 6.5. The $\Delta\sigma_{pN}$ is the visible cross section and was also a free parameter in the fit. The normalization constants of the parameterizations can be easily calculated. The normalized parameterizations are:

$$P(p_T) = b \cdot e^{-bp_T^2} \quad (6.13)$$

$$P(p_T) = \frac{b'^2}{2} \cdot e^{-b'p_T} \quad (6.14)$$

$$P(p_T) = (\beta - 1)A^2 \cdot [1 + (A p_T)^2]^{-\beta}, \quad A = \frac{\sqrt{\pi} \Gamma(\beta - \frac{3}{2})}{2 \Gamma(\beta - 1) \langle p_T \rangle} \quad (6.15)$$

$$P(p_T) = 5A^2 \cdot [1 + (A p_T)^2]^{-6}, \quad A = \frac{35\pi}{256 \langle p_T \rangle} \quad (6.16)$$

Our default parameterization was the one with $\langle p_T \rangle$ and β given by Eq. 6.15, which fits the Monte Carlo simulation very well and was proven by E769 to fit the data in their entire p_T range.

[‡]for D^{*+} : wrong sign combinations in the signal window

No.	Function $N_{bgr}(p_T^2)$
1	$e^{A+Bp_T^2}$
2	$e^{A+Bp_T^2}\epsilon(p_T^2)$
3	$e^{A+Bp_T^2}(1 + Cp_T^2)$
4	$e^{A+Bp_T^2+Cp_T^4}$
5	$A(1 + Bp_T^2)^{-6}$
6	$A(1 + Bp_T^2)^{-6}\epsilon(p_T^2)$
7	$A(1 + Bp_T^2)^{-6}(1 + Cp_T^2)$
8	$A(1 + Bp_T^2)^{-C}$

Table 6.2: Parameterizations for the p_T distribution of background events

data sample	$\langle p_T \rangle$ [GeV/c]	β	χ^2/ndf	$\langle p_T \rangle, \beta = 6$	χ^2/ndf
D^0	1.03 ± 0.09	3.3 ± 1.1	0.59	1.03 ± 0.07	0.67
D^+	1.07 ± 0.06	30 ± 76	0.83	1.04 ± 0.06	0.78
D^{*+}	1.03 ± 0.11	8.7 ± 10.1	1.13	1.02 ± 0.11	1.10
$D^0/D^+/D^{*+}$	1.03 ± 0.04	6.4 ± 2.8	0.82	1.03 ± 0.04	0.81

Table 6.3: Fitted parameters on real data samples.

The distribution of background events $N_{bgr}(p_T^2)$ was assumed to be the same in shape and normalization for the signal window and side bands. Several parameterizations, listed in Table 6.2, were fitted first to the distributions of the events from side bands. They all fitted well. We chose the one among those with 2 free parameters which gave the smallest χ^2/ndf . These were function No.1 for D^0 and D^+ and function No.2 for D^{*+} .

Finally we fitted simultaneously the events in the signal window with a function $N_D(p_T^2) + N_{bgr}(p_T^2)$ and the events in the side bands with a function $N_{bgr}(p_T^2)$. The free parameters with the default parameterization, when we fitted D meson data samples separately, were $\langle p_T \rangle$, β , $\Delta\sigma_{pN}$ for the signal and A and B for the background. With the simultaneous fit to all three data samples, the parameters $\langle p_T \rangle$ and β were common, while the σ_{pN} , A and B were used for each D meson data sample individually, thus the number of free parameters was 11.

The simultaneous fit of all three D meson data samples with default parameterization (Eq. 6.15) is shown in Fig. 6.8. The resulting parameters $\langle p_T \rangle$ and β are summarized in Table 6.3 together with a χ^2 of the fits. Fits to all data samples gave good χ^2 . Compared to the Monte Carlo simulation (Table 6.1), the $\langle p_T \rangle$ is significantly larger on real data, while β is within one standard deviation equal to the value obtained from the Monte Carlo simulation. The statistics of individual D meson data samples is slightly too low for fitting with both parameters $\langle p_T \rangle$ and β being free, and resulted in a large error of the parameter β . We repeated the fit with the fixed value of $\beta = 6$. As one can see from Table 6.3, the parameter $\langle p_T \rangle$ has not changed much.

By subtracting the histograms of side band events from the histograms of signal window

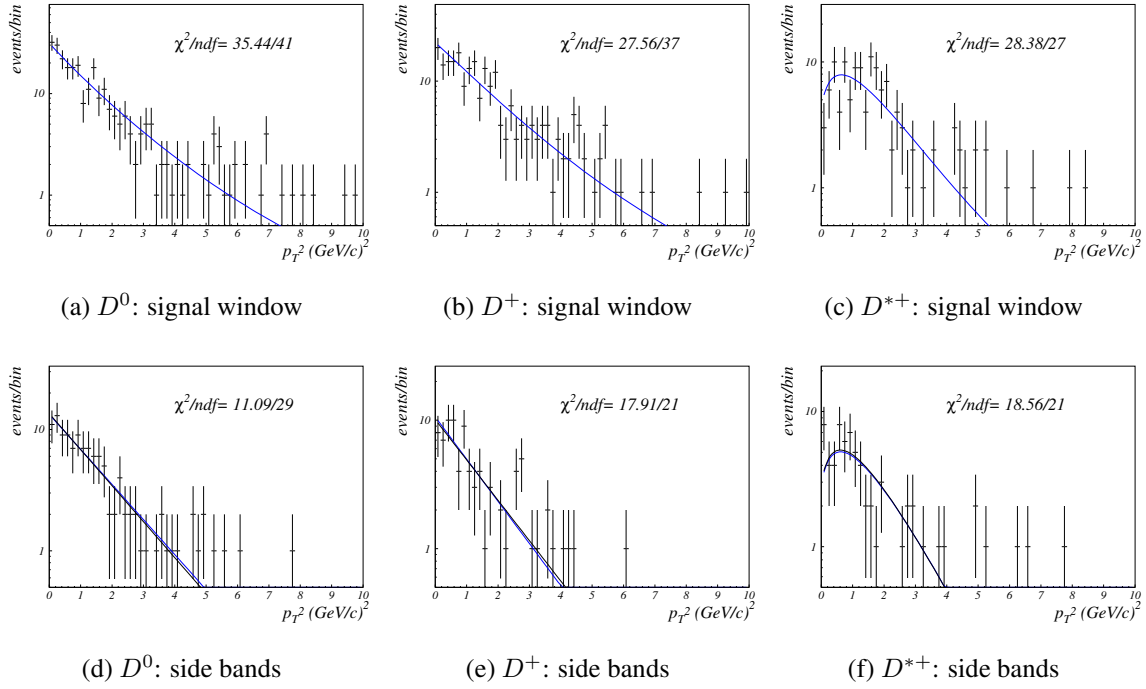


Figure 6.8: Simultaneous maximum likelihood fit of all three data samples.

events we determined the visible differential cross sections. From Eq. 5.6 we derived

$$\frac{d\sigma}{dp_T^2} = \frac{\frac{\Delta N}{\Delta p_T^2}}{Br \cdot \epsilon(p_T^2) \cdot \sum_i \mathcal{L}_i A_i} \quad (6.17)$$

where ΔN is the number of signal events in a bin at p_T^2 and of the size Δp_T^2 and $\epsilon(p_T^2)$ is the acceptance for that bin. The differential cross sections are plotted in Fig. 6.9. The fit of Eq. 6.15 is also shown.

The total visible cross sections can be determined in three ways: (1) by summing the data points of Fig. 6.9 and multiplying the sum with the bin size, (2) from the simultaneous likelihood fit, since $\Delta\sigma_{pN}$ is a free parameter in the fit and (3) by determining the new efficiencies from the re-weighted Monte Carlo simulation and correcting the cross sections from Table 5.4 accordingly, as is explained in section 6.6. The cross sections determined in the three different ways are summarized in Table 6.4. The results of all three methods are in reasonable agreement. The smallest statistical error has the cross sections determined with the method (3) because the background was fitted in the wide invariant mass range. On the other hand the results obtained with the method (1) are independent of the parameterization of the distribution.

The exponential parameterizations in p_T^2 (Eq. 6.13) and in p_T (Eq. 6.14) have also been fitted to the data (Fig. 6.10). The result of the fit with Eq. 6.13 depends on the fit range, as one can see from Fig. 6.10. This fact is important when comparing this result with the results

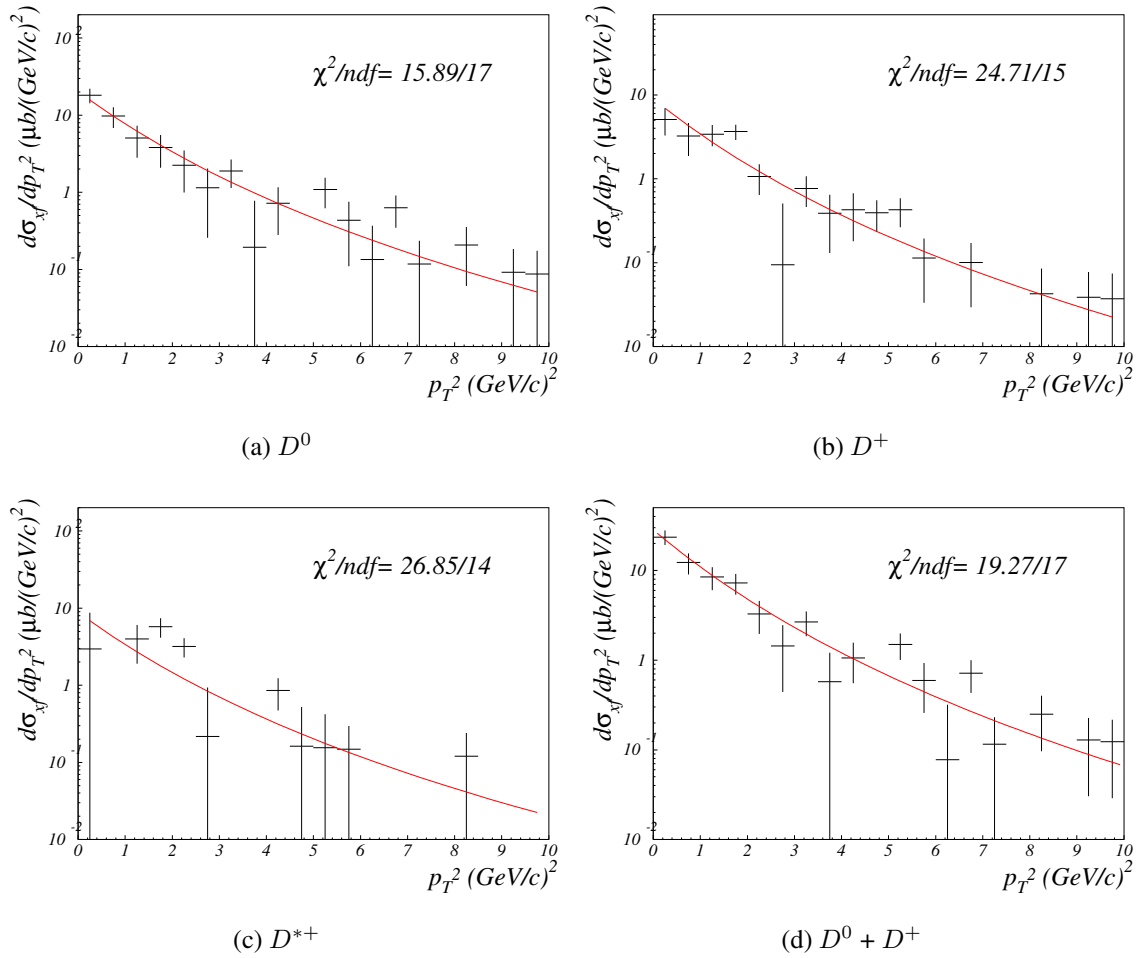


Figure 6.9: Differential visible cross sections $d\sigma/dp_T^2$, with the fit of eq. 6.15 performed simultaneously on all three D meson data samples. The cross section (d) is a sum of (a) and (b).

	$\Delta\sigma_{pN} [\mu\text{b}]$		
	(1) by sum	(2) from fit	(3) re-weighted
D^0	22.6 ± 3.0	22.9 ± 2.9	24.7 ± 2.4
D^+	9.4 ± 1.3	9.5 ± 1.3	9.8 ± 1.0
D^{*+}	8.2 ± 3.7	10.5 ± 2.5	11.2 ± 2.4

Table 6.4: Visible cross sections determined with three different methods (see text).

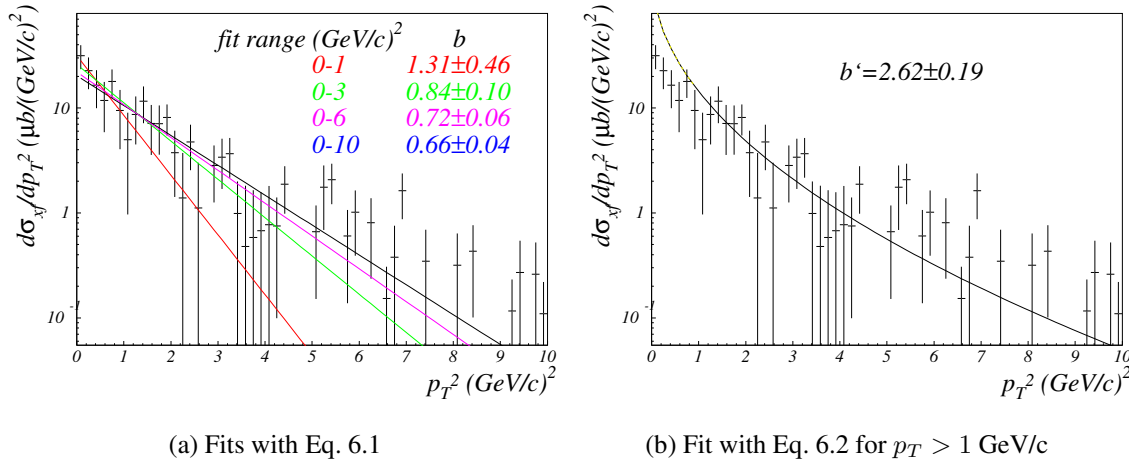


Figure 6.10: Fits with exponential parameterizations.

of other experiments, because the p_T ranges were different. By restricting the fitting range to $p_T^2 < 3 (\text{GeV}/c)^2$ this result of $b = 0.84 \pm 0.10$ is in good agreement with the measurements of the three experiments at 800 GeV listed in Table 1.4, which measured the distribution up to 3-4 $(\text{GeV}/c)^2$.

6.5 Measurement of $d\sigma/dx_F$

The simultaneous maximum likelihood fit of the events in the signal window and sidebands was also used for the fits to the $d\sigma/dx_F$ distribution. The background was parameterized with the same function as had been used for the parameterization of acceptances and is given with Eq. 6.10. We fitted this function first to the data points of the side band events and got the values of parameters x_0 , σ , A and B . Then in the simultaneous fit only the normalization parameter C was free.

The distribution of signal events was parameterized with the extended power law parameterization given by Eq. 6.7. The boundary parameter x_b was fixed to the value measured by E791 ($x_b = 0.062$), because the range of $-0.15 < x_F < 0.05$ is too small to have this parameter free. By multiplying this parameterization by the acceptance $\epsilon(x_F)$, determined from the Monte Carlo simulation and shown in Fig. 6.7, we constructed the function for fitting the distribution of reconstructed signal events $N_D(x_F)$. Similarly to the fits in the previous section, we fitted simultaneously the events in the signal window with the function $N_D(x_F) + N_{bgr}(x_F)$ and the events in the side bands with the function $N_{bgr}(x_F)$, parameterized by Eq. 6.10.

We fitted simultaneously D^0 and D^+ data samples. The free parameters were the exponent n , the two signal normalizations A_{D^0} and A_{D^+} and the two background normalizations C_{D^0} and C_{D^+} . The fit is shown in Fig. 6.11. The fitted exponent n is 7.5 ± 3.2 and agrees well with the results of E653 and E743 summarized in Table 1.4, but is consistent also with the value from

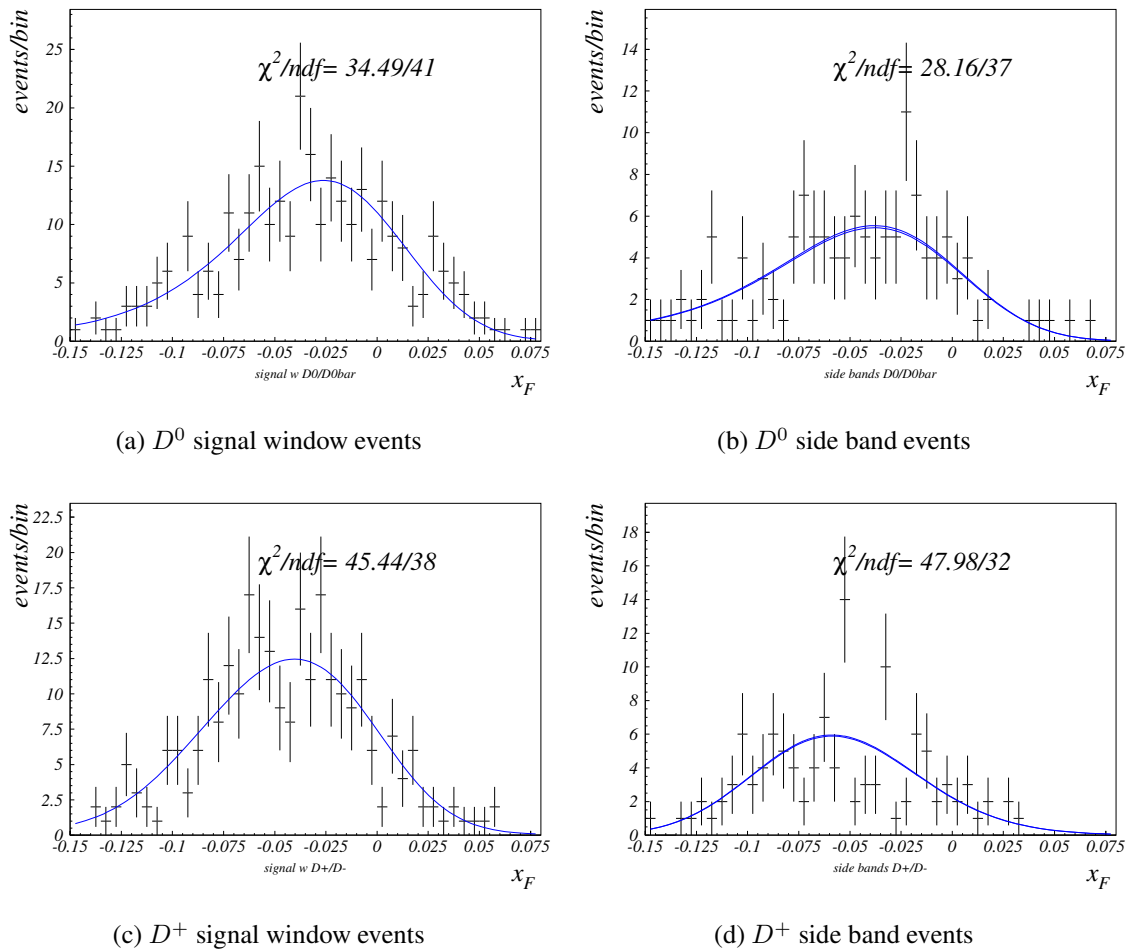


Figure 6.11: Simultaneous maximum likelihood fit of D^0 and D^+ data samples.

the Monte Carlo simulation of 5.4.

We fitted the data sets also at different boundary parameters x_b . As expected, the exponent is quite sensitive to the choice of the boundary parameter (see Table 6.5). Unfortunately, the x_F range of this data sets is too small to be competitive in this measurement with the other experiments.

With the expression similar to Eq. 6.17 we determined the differential cross section $d\sigma/dx_F$ in several bins in the accessible range. The plots are shown in Fig. 6.12 together with the fits with different values of x_b .

6.6 Re-weighting of Monte Carlo events

The x_F distribution measured by E653 and E743 and the p_T distribution determined from this data differ from the distributions generated with PYTHIA. Since the acceptance depends on

x_b	n	χ^2/ndf
0.000	4.6 ± 2.2	0.95
0.040	6.1 ± 2.7	0.94
0.050	6.7 ± 2.9	0.94
0.062	7.5 ± 3.2	0.94
0.070	8.0 ± 3.5	0.93
0.100	10.4 ± 4.4	0.94

Table 6.5: Fitted exponent n at different values of the parameter x_b

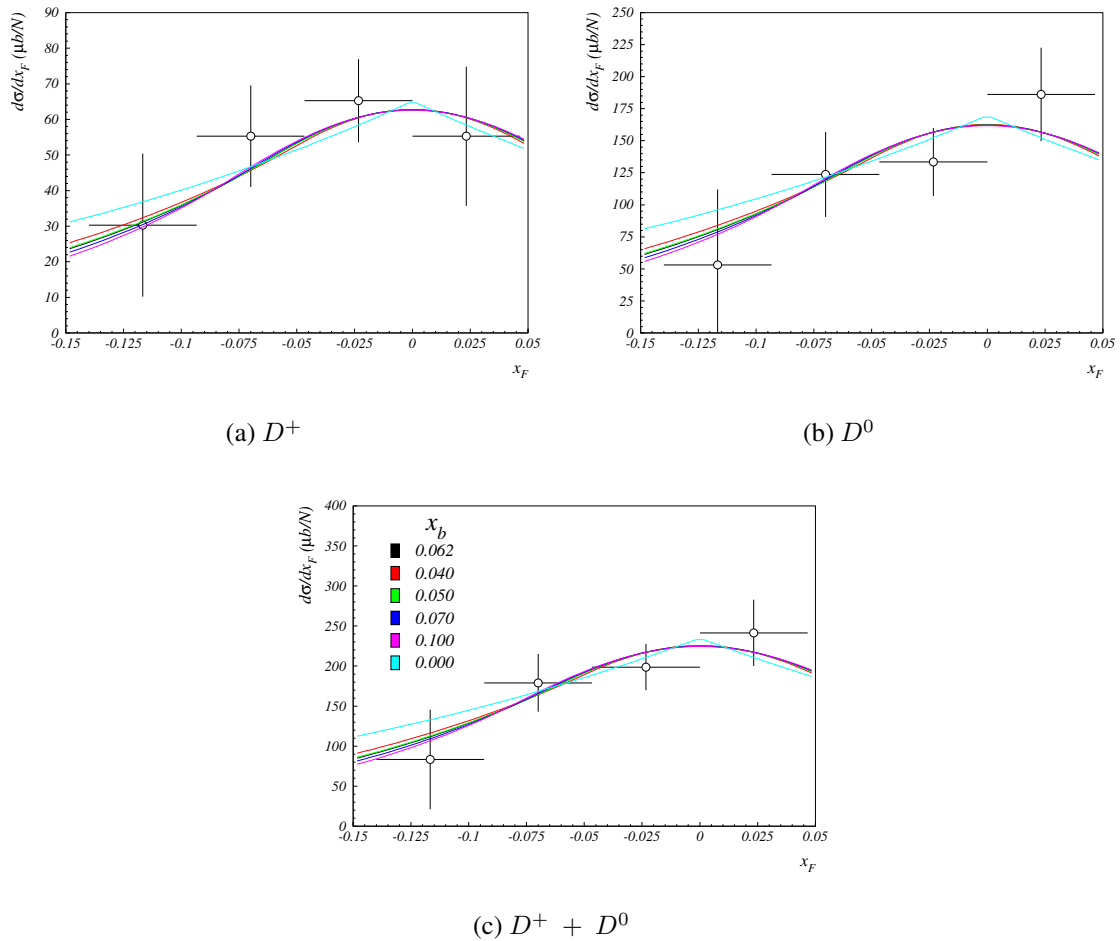


Figure 6.12: Differential cross sections $d\sigma/dx_F^2$ with fits for different values of boundary parameter x_b .

	$\langle p_T \rangle$	β	n	x_b
MC sample	0.898	4.80	5.42 (5.33)	0.052
real data sample	1.03 ± 0.04	6.4 ± 2.8	7.7 ± 1.4	0.062

Table 6.6: Parameter values used for the determination of weights. The value for n written in parenthesis was used with the power law parameterization Eq. 6.6.

both kinematical variables, the kinematical distributions in the signal Monte Carlo simulation have to be re-weighted in order to determine the efficiencies correctly.

The weights were determined from the normalized distributions for the real data and for the Monte Carlo events $P_{DATA}(x)$ and $P_{MC}(x)$ respectively with $x \equiv p_T$ or $x \equiv x_F$. We used the same parameterizations for the Monte Carlo simulation and the real data distributions. For the p_T distributions the parameterization with Eq. 6.15 was used, while for the x_F distributions to study the systematics both parameterizations were taken; the power law parameterization, given with Eq. 6.6, and the extended one with Eq. 6.7. The errors on the measured parameters were used for the estimation of the systematic error.

The weights were calculated as the ratio of normalized distributions

$$w(x) = \frac{P_{DATA}(x)}{P_{MC}(x)} \quad (6.18)$$

The parameter values for P_{MC} were taken from fits to the mixture of D mesons (Table 6.1) and the values for P_{DATA} from the measurements. The parameters are summarized in Table 6.6 and the weights are plotted in Fig. 6.13. Note that the weights are the same for all D meson samples. In this respect small differences in distributions between different D mesons and their charge conjugate states remain after re-weighting. We think that this is more appropriate than to re-weight all Monte Carlo generated D meson samples to the same distribution, since no measurements exist which would prove that the distributions are the same.

To determine the efficiency correction factors we calculated the efficiencies from the un-weighted and from the weighted Monte Carlo simulation by following the same procedure as explained in section 5.2. The difference was in the counting procedure of reconstructed decays: we used the side band subtraction method and not a fit to the invariant mass distribution. The number of reconstructed and the number of generated decays in Eq. 5.7 was, in the case of the re-weighted Monte Carlo simulation, obtained by summing the weights of the D mesons.

The efficiency correction factors were summarized in Table 6.7. The errors were obtained by calculating the factors for the particular parameter at the values shifted by one standard deviation up and down from its central value and taking the half of the resulting difference. The errors resulting from variation of $\langle p_T \rangle$ and β were added in quadrature.

The difference between correction factors for both charge conjugate states as well as the difference between different wire samples are negligible compared to the estimated errors, thus the same correction factors can be used for all subsamples of a particular D meson.

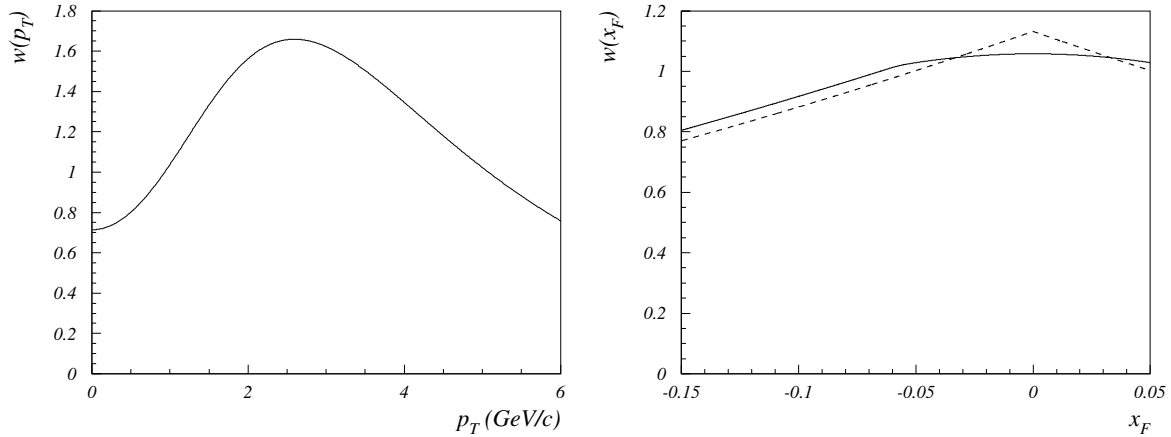


Figure 6.13: Weights for the p_T distribution (left) and weights for the x_F distribution (right). The dashed curve are the weights calculated from the power law parameterization Eq. 6.6.

meson	p_T	x_F (Eq. 6.7)	x_F (Eq. 6.6)
D^0	1.063 ± 0.025	1.023 ± 0.015	1.032 ± 0.018
D^+	1.107 ± 0.038	1.017 ± 0.010	1.020 ± 0.011
D_s^+	1.178 ± 0.090	1.006 ± 0.002	1.003 ± 0.001
D^{*+}	1.165 ± 0.050	1.023 ± 0.015	1.030 ± 0.017

Table 6.7: Correction factors obtained from re-weighting of distributions in p_T and x_F .

D^0	D^+	D_s^+	D^{*+}
1.087 ± 0.032	1.126 ± 0.040	1.185 ± 0.091	1.192 ± 0.055

Table 6.8: Overall efficiency correction factors from re-weighting of kinematical distributions.

The difference arising from the two parameterizations of the x_F distribution is also small compared to the errors, as one can see from Table 6.7. We have chosen the correction factors obtained with the extended power law parameterization Eq. 6.7 and added the difference in quadrature to the error. The products of both correction factors, e.g. the overall correction factors for efficiencies, are summarized in Table 6.8.

6.7 Visible fraction

In order to extrapolate the measurements to the full phase space we needed to determine the fraction of D mesons in the visible range defined by $-0.15 < x_F < 0.05$. By using the measured value of the exponent $n = 7.7 \pm 1.4$ we calculated the visible fraction from both parameterizations. The visible fractions obtained from the power law parameterization Eq. 6.6 and from the

extended power law parameterization Eq. 6.7 are 0.558 ± 0.051 and 0.542 ± 0.048 respectively. The difference is small compared to the error, estimated from the error of parameter n . For the extrapolation we decided to use the average of both numbers:

$$f_{vis} = 0.55 \pm 0.05 \quad (6.19)$$

For comparison, the visible fractions given by the signal Monte Carlo simulation are 0.45, 0.44, 0.46 and 0.43 for D^0 , D^+ , D_s^+ and D^{*+} respectively.

7 Systematic errors

In this section the systematic uncertainties are determined for the following measurements: total visible production cross sections, cross section ratios, A-dependence parameter α and leading to non-leading particle asymmetries.

7.1 Total visible cross sections

The total systematic uncertainties according to Eq. 5.6 are composed of contributions from event counting, branching fractions, integrated luminosity and reconstruction efficiency. Furthermore, the uncertainty of the reconstruction efficiency can be divided into contributions from Monte Carlo statistics, track reconstruction efficiency, particle identification efficiency, analysis cuts and the contribution from the reweighting of kinematical distributions.

7.1.1 Event counting

A source of the systematic uncertainty is the parameterization of the combinatorial background. We used the exponential shape for D^0 , D^+ and D_s^+ , but a linear or a quadratic function could also be fitted well. The number of fitted events with the three different parameterizations are presented in Table 7.1. The systematic error of the event counting was estimated as a maximal deviation of the number of events and amounts to 3.4%, 2.6% and 6% for the D^0 , D^+ and D_s^+ respectively.

For the D^{*+} the estimation of the counting error was done by fitting the wrong sign events with the same parameterization as for the background in the right sign events and using the resulting shape in a fit to the right sign events. The systematic uncertainty was estimated to 9.7%.

Meson	exp.	linear	quadratic	rel. error
D^0	174.8	168.9	173.4	3.4%
D^+	148.2	144.4	145.1	2.6%
D_s^+	11.4	12.4	10.9	6.0%

Table 7.1: Fitted number of events with exponential, linear or quadratic parameterizations of the combinatorial background.

7.1.2 Branching fractions

The uncertainties of the branching fractions (Table 5.3) are 1.8%, 3.6%, 13% and 1.9% for the D^0 , D^+ , D_s^+ and D^{*+} , respectively.

7.1.3 Integrated luminosities

The individual relative errors on the integrated luminosities for C, Ti and W are 3.9%, 4.2% and 2.9%, respectively and a common scaling error is 3% [38]. With the standard error propagation and assuming that the individual errors are uncorrelated, we obtained an error of 2.1% on the integrated luminosities summed over nucleons $\sum_i A_i \mathcal{L}_i$. By adding in quadrature a common scaling error of 3% we estimated the systematic uncertainty to 3.7%.

7.1.4 Efficiency

Monte Carlo Statistics The systematic uncertainties due to Monte Carlo statistics were calculated from the first row of Table 5.2 and amount to 1.2%, 1.3%, 3.7% and 1.1% for the D^0 , D^+ , D_s^+ and D^{*+} respectively.

Track reconstruction efficiency The track reconstruction efficiency was tested separately for VDS and OTR using $K_s^0 \rightarrow \pi^+\pi^-$ decays. One of the pions was reconstructed from VDS (or OTR) and ECAL information only. Applying the same procedure to Monte Carlo data, we obtained an uncertainty of the track reconstruction efficiency of 1.5% per track. The systematic uncertainties are 3% for D^0 and 4.5% for D^+ , D_s^+ and D^{*+} .

Particle identification Particle identification efficiencies were tested by using the reconstructed decays of K_s^0 , ϕ and $\Lambda(\bar{\Lambda})$ as sources of pions, kaons and protons. The same procedure was applied on the real data and on the inelastic Monte Carlo simulation. Only the tracks within the acceptance of the RICH were considered. The momentum dependent identification efficiencies are shown in Fig 7.1. The real data efficiencies are about 5% lower compared to the Monte Carlo efficiencies, regardless of particle type and likelihood cuts. The same discrepancy was also obtained for protons. We investigated this discrepancy further. Larger event multiplicities on the real data are not the reason. By reweighting the Monte Carlo events to the multiplicity of real data the efficiencies decreased by only 0.5%. We attributed the lower efficiency on the real data to the angular resolutions of the track segments in the OTR, which seem to be underestimated by the Monte Carlo simulation. Oppositely, the track segments in the VDS are well modelled by the Monte Carlo simulation (see next paragraph).

We calculated the momentum dependent correction factors to the particle identification efficiency as the ratio of the efficiencies extracted from the real data and on the Monte Carlo simulated data, i.e. as the ratios of the histograms shown in Fig. 7.1. These correction factors were then used to determine the correction factors of the reconstruction efficiency for each

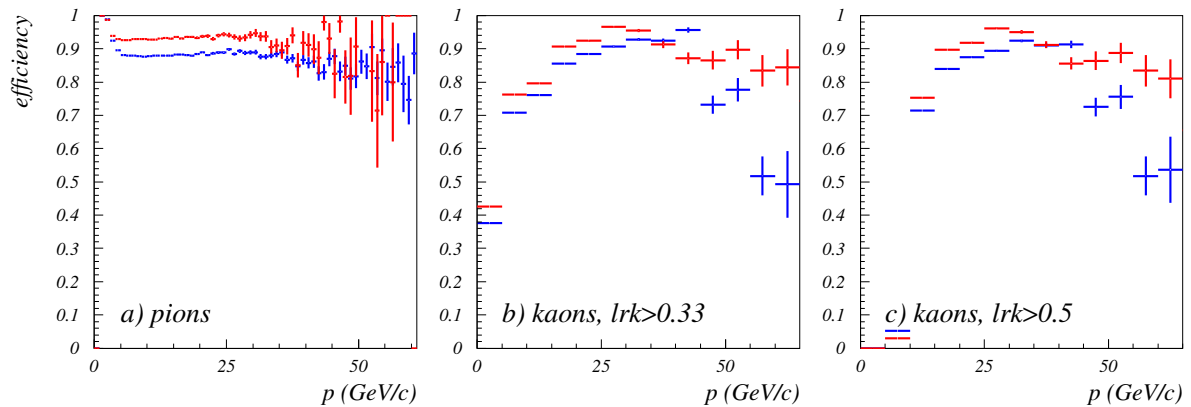


Figure 7.1: Comparison of the particle identification efficiencies between real data (blue) and the Monte Carlo simulation (red) for pions from K_s^0 and kaons from ϕ decays.

D^0	D^+	D_s^+	D^{*+}
0.90	0.86	0.86	0.90

Table 7.2: Correction factors for the reconstruction efficiencies due to particle identification efficiency mismatch.

of the D mesons. From the momentum distributions of pions and kaons obtained from signal Monte Carlo simulation after the analysis cuts, we calculated the average correction factors for pions and kaons from different D mesons. We obtained nearly the same value (within 0.5%) of 0.95 per identified particle. We corrected the D meson reconstruction efficiencies by using the above factor and assigned a systematic uncertainty of 2% per identified particle. The correction factors are summarized in Table 7.2.

Analysis cuts The stability of analysis cuts is discussed in Appendix A. By the determination of cross sections in a relatively wide range around the optimal cuts we obtained the cross section variations of 9%, 5%, 11% and 17% for the D^0 , D^+ , D_s^+ and D^{*+} , respectively. These variations when compared to the statistical errors of 10%, 11%, 34% and 22% are all smaller. Since the data samples at different cuts are not the same, the variations include statistical fluctuations as well. In such a case it is not easy to disentangle statistical fluctuations from possible systematic effects. We decided not to use the above numbers for the estimation of systematic uncertainties.

Since the analysis cuts were performed on the significances, the two quantities have to be well reproduced with the Monte Carlo simulation: the track resolutions, when extrapolated to the targets and the estimated track errors given by a covariance matrix. We studied both on samples of 100k pion candidates each and from several runs. The pion candidates were selected with the same criteria as used in the analysis. Both quantities were compared to the inelastic Monte Carlo simulation (runs 09_302 and 09_304).

VDS	20199 (C)	20653 (C)	20768 (C)	20341 (W)	20680 (W)	average	smeared
1	0.97	0.99	0.95	1.07	0.98	0.99	1.05
2	1.05	1.03	1.09	1.05	1.09	1.06	1.04
3	1.03	1.05	1.05	1.04	1.04	1.04	1.03
4	0.99	1.00	1.00	0.98	0.98	0.99	1.05
5	1.01	1.01	1.00	1.02	1.01	1.01	1.04
6	1.02	1.00	1.02	1.01	1.03	1.02	1.04

Table 7.3: Ratio between DATA and MC of impact parameters to the reconstructed wire, the average and the effect of smearing the parameters tx and ty by 10%. The last column refers to the ratio of the smeared and the original Monte Carlo simulation.

The track resolutions were studied on the basis of their impact parameters with respect to the reconstructed wire. Deviations of several percents were observed. The largest were for the tracks starting at the VDS superlayers 2 and 3 (Table 7.3). Similar deviations for superlayers 2 and 3 were obtained, if we smeared the track parameters tx and ty on the Monte Carlo simulation by 10% of the corresponding covariance matrix element *. We estimate that the Monte Carlo simulation describes the track resolutions to better than 10% accuracy.

By smearing the tracks in the signal Monte Carlo simulation by 10% and by comparing the efficiencies of un-smeared and the smeared Monte Carlo simulation, we estimated this contribution to the systematic uncertainty of the cross section to 2.8% for the D^0 , 2.2% for the D^+ , 4.4% for D_s^+ and 2.6% for D^{*+} .

The estimated track errors were studied on the basis of their impact parameter errors, calculated from the covariance matrices of the track and of the primary vertex. The distributions from the inelastic Monte Carlo simulation were compared to the distributions from real data for each VDS super-layer and in 10 inverse momentum bins in the range 0 - 0.5 (GeV/c) $^{-1}$. A very good agreement was found. The mean of the distributions deviated by less than 1%. The systematic uncertainty of the cross sections was estimated by changing the values of all significances (d, b, b_m) on which we cut by $\pm 1\%$ and taking for the error the half of the difference in resulting reconstruction efficiency. The contributions to the systematic uncertainties are 1.6%, 1.6%, 2.0% and 0.1% for the D^0, D^+, D_s^+ and D^{*+} respectively.

In addition, we studied the impact of the event multiplicity. With the old Monte Carlo simulation, where the multiplicities were considerably lower (40% for the hits in RICH and 15% for the number of long tracks), the efficiencies were higher by about 1%. With the new Monte Carlo simulation, which was used for this analysis, the event multiplicities agree with the ones observed on the real data much better (see Appendix B), thus we consider this contribution to be negligible.

The total systematic uncertainty of cross sections arising from analysis cuts is estimated to

*A gaussian random number with sigma equal to 46% of the covariance matrix element was added.

Source	D^0	D^+	D_s^+	D^{*+}
Monte Carlo statistics	1.2%	1.3%	3.7%	1.1%
Track reconstruction	3.0%	4.5%	4.5%	4.5%
Particle identification	4.0%	6.0%	6.0%	4.0%
Analysis cuts	3.2%	2.7%	4.8%	2.6%
Re-weighting	2.9%	3.6%	7.7%	4.6%
Total	6.7%	8.8%	12.3%	8.1%

Table 7.4: Summary of systematic uncertainties of reconstruction efficiency.

Source	D^0	D^+	D_s^+	D^{*+}
Event counting	3.4%	2.6%	6.0%	9.7%
Branching fractions	1.8%	3.6%	13%	1.9%
Luminosity	3.7%	3.7%	3.7%	3.7%
Efficiency	6.7%	8.8%	12.3%	8.1%
Total	9%	11%	19%	13%

Table 7.5: Summary of systematic uncertainties of visible cross sections

be 3.2%, 2.7%, 4.8% and 2.6% for the D^0 , D^+ , D_s^+ and D^{*+} , respectively.

Reweighting of kinematical distributions The systematic uncertainties due to re-weighting of kinematical distributions were estimated in section 6.6 by varying the parameter values according to their errors. The results are given in Table 6.8. The uncertainties were estimated to be 2.9%, 3.6%, 7.7% and 4.6% for the D^0 , D^+ , D_s^+ and D^{*+} , respectively.

7.1.5 Summary of systematic uncertainties

The systematic uncertainties of the reconstruction efficiencies are summarized in Table 7.4 and the uncertainties of visible cross sections in Table 7.5. The systematic uncertainties of visible production cross sections are estimated to be 8%, 11%, 19% and 13% for the D^0 , D^+ , D_s^+ and D^{*+} respectively.

7.2 Cross section ratios

The following effects contribute to the systematic errors of the cross-section ratios: uncertainties in event counting and branching ratios, the error due to the finite Monte Carlo statistics and systematic errors from the analysis (track reconstruction, particle identification, analysis cuts and re-weighting), while the error in luminosity cancels. The errors due to the uncertainties in the track reconstruction and particle identification efficiencies cancel only partially, because of

Source	D^+/D^0	D^{*+}/D^0	$D_s^+/(D^0 + D^+)$
Event counting	4.3%	10.0%	6.3%
Branching ratio	4.0%	0.5%	13%
Monte Carlo statistics	1.8%	1.6%	3.7%
Track reconstruction	1.5%	1.5%	1.0%
Particle identification	2.0%	0.0%	1.4%
Analysis cuts	0.6%	1.4%	1.7%
Re-weighting	1.0%	2.0%	4.5%
Total	6%	11%	16%

Table 7.6: Summary of systematic uncertainties of cross section ratios.

the different number of particles in the final state. We note that in the case of the ratio D^{*+}/D^0 there is no contribution from particle identification because we applied no identification requirements for the slow pion in the decay of the D^{*+} . The uncertainty in track reconstruction and particle identification efficiency for the ratio $D_s^+/(D^0 + D^+)$ was estimated with a toy Monte Carlo simulation.

The effect of the analysis cuts was determined in a way, similar way to that for the cross sections (see section 7.1.4 for details) by calculating the ratio of efficiencies with the smeared Monte Carlo simulation to the ratio determined with original efficiencies. The effect of the uncertainty in the covariance matrix was estimated by a simultaneous $\pm 1\%$ variation of all significances on which we cut. In the same way the effect of the re-weighting of the kinematical distributions was evaluated by changing the re-weighting factors by $\pm 1\sigma$.

The resulting contributions are summarized in Table 7.6, and amount in total to 6%, 11% and 16% for the cross section ratios for D^+/D^0 , D^{*+}/D^0 and $D_s^+/(D^0 + D^+)$ respectively.

7.3 A-dependence parameter α

Only two sources contribute to the measurement of the A-dependence parameter α : the luminosity per wire and the Monte Carlo statistics in the calculation of the efficiency. For the calculation of this systematic error the cross section per nucleus was calculated with a toy Monte Carlo simulation, using Eq. 5.1. To estimate the contribution of the error on α , the efficiency for each target was smeared with the statistical errors given in Table 5.2. The resulting cross sections per nucleus for the three target materials were then fitted with Eq. 5.2 to get the value of the parameter α for each meson. A weighted average was calculated for the four values to get the common value of α .

This procedure was repeated 10000 times. The values for the parameter α of those fits was then fitted with a gaussian. The standard deviation of the gaussian was taken as the contribution to the systematic error on α . The same procedure was repeated also by smearing the luminosities of the targets by their errors given in chapter 7.1.3. The contributions to the systematic error on

Source	D^0	D^+	D^{*+}	D_s^+	total
Monte Carlo Statistics	1.0%	1.1%	0.8%	3.3%	0.6%
Luminosity	2.2%	2.1%	2.3%	2.2%	2.2%
Total	2.4%	2.4%	2.4%	4.0%	2.3%

Table 7.7: Summary of the systematic uncertainties for the A-dependence parameter α

α are summarized in Table 7.7

7.4 Leading to non-leading particle asymmetries

The only contribution to the systematic uncertainty comes from Monte Carlo statistics. From the definition of leading to non-leading particle asymmetry with Eq. 5.9 we calculated the error by the standard error propagation method. The absolute systematic uncertainties of the asymmetries are 0.01, 0.01, 0.01 and 0.04 for the D^0 , D^+ , D^{*+} and D_s^+ , respectively.

8 Results

8.1 Corrected cross sections

By using the correction factors from the re-weighting of the kinematical distributions (Sec. 6.6) in the Monte Carlo simulation and for the efficiency of the RICH (Sec. 7.1.4) we can derive the final values of the cross sections. The two correction factors are extracted from Table 6.8 and Table 7.2, and their products, the final correction factors, are listed in Table 8.1.

D^0	D^+	D_s^+	D^{*+}
0.98	0.97	1.02	1.07

Table 8.1: Final correction factors for the reconstruction efficiencies.

From the cross sections from Table 5.4 the final cross sections in the visible range are calculated by dividing these values with the correction factors. The cross sections per nucleon (in μb) are: $26.8 \pm 2.6 \pm 2.4$, $11.0 \pm 1.1 \pm 1.2$, $10.2 \pm 3.5 \pm 1.9$ and $12.1 \pm 2.6 \pm 1.6$ for the D^0 , D^+ , D_s^+ and D^{*+} respectively. The extrapolation to the full x_F range was calculated using the factor $f_{vis} = 0.55 \pm 0.05$ from Eq. 6.19. The error on the factor was added to the systematic errors from Table 7.5. The corresponding total cross sections per nucleon (in μb) are: $48.7 \pm 4.7 \pm 6.2$, $20.0 \pm 2.0 \pm 2.9$, $18.5 \pm 6.4 \pm 3.9$ and $22.0 \pm 4.7 \pm 3.5$. The results are summarized in Table 8.2.

These results can be compared to previous experimental studies. Figure 8.1 shows the comparisons for all the four D-mesons. The fit has been performed with the formula given in Eq. 1.35. The parameter p_3 was set to 0.35 as suggested in [4] for proton beams, while the other parameters depend on the selected PDF. The only parameter left free in these fits to data points was the normalization. All our results agree well: D^0 and D^{*+} are within one standard

	$\sigma[\mu\text{b}]$			
	D^0	D^+	D_s^+	D^{*+}
visible range	$26.8 \pm 2.6 \pm 2.4$	$11.0 \pm 1.1 \pm 1.2$	$10.2 \pm 3.5 \pm 1.9$	$12.1 \pm 2.6 \pm 1.6$
full x_F	$48.7 \pm 4.7 \pm 6.2$	$20.0 \pm 2.0 \pm 2.9$	$18.5 \pm 6.4 \pm 3.9$	$22.0 \pm 4.7 \pm 3.5$

Table 8.2: Cross sections per nucleon in the visible x_F range and extrapolated to full phase space

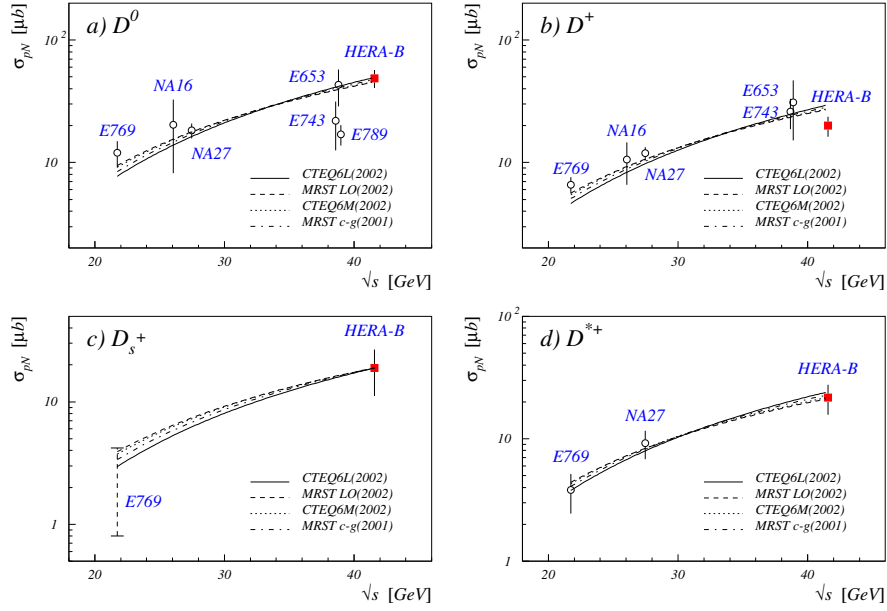


Figure 8.1: Comparison of the results with previous experiments.

deviation, D^+ is 1.8 standard deviations below the value from the fit. The measured cross section for D_s^+ production is in good agreement with the 90% confidence level limit published by the experiment E769, and also with the unpublished measured point from the same experiment (PhD thesis [47])[†].

8.2 Cross section for the charm quark pair production

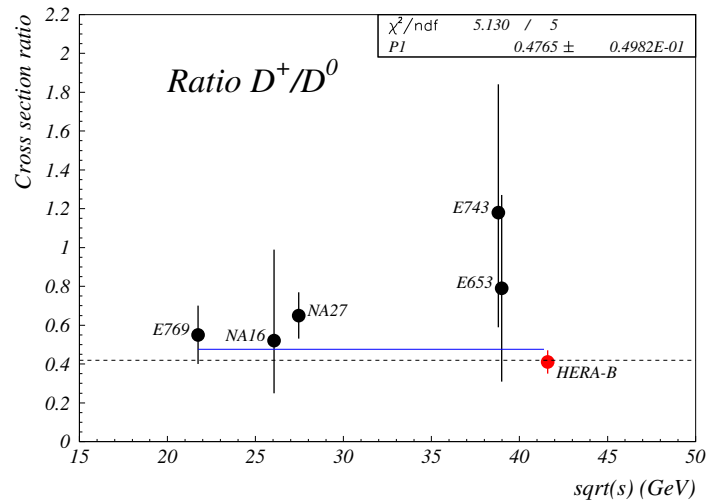
The sum of the D -meson cross sections per nucleon $\sigma(D^0) + \sigma(D^+) + \sigma(D_s^+) = 87.2 \pm 8.2 \pm 11.6 \mu\text{b}$ accounts for $(89.1 \pm 4.1)\%$ of the charm cross section [11]. The resulting cross section per nucleon from the charm quark pair production is $\sigma(c\bar{c}) = 48.9 \pm 4.6 \pm 6.9 \mu\text{b}$. The systematic uncertainty was estimated with a toy Monte Carlo simulation and due to correlations it is slightly larger than the value, which one would get by adding in quadrature the individual contributions.

8.3 Cross section ratios

The cross section ratios calculated from the results in Table 8.2 are summarized in Table 8.3, a comparison with previous experiments is presented in Fig. 8.2. The value for the ratio $\sigma(D^+)/\sigma(D^0) = 0.41 \pm 0.06 \pm 0.02$ is the most precise measurement of this quantity in

[†]To compare the D_s^+ -results we scaled the E769 cross sections with the factor $\frac{1.77}{2.16}$ to account for the different branching fraction of the decay $D_s^+ \rightarrow \phi\pi^+$ used by E769

D^+/D^0	D^{*+}/D^0	$D_s^+/(D^+ + D^0)$
$0.41 \pm 0.06 \pm 0.02$	$0.45 \pm 0.11 \pm 0.05$	$0.28 \pm 0.10 \pm 0.05$

Table 8.3: Cross section ratios**Figure 8.2:** Cross section ratio $R = D^+/D^0$, comparison with previous experiments. The dotted line at $R = 0.42$ shows the prediction of the isospin model with $P_V = 0.6$ [4].

proton-nucleus collisions and is in agreement with the world average in hadron-nucleon collisions 0.41 ± 0.03 [4]. The ratio $\sigma(D^{*+})/\sigma(D^0) = 0.45 \pm 0.11 \pm 0.05$ is in good agreement with the results of E769 and NA27. Both ratios are also in agreement with the predictions of the simple isospin model. Our result for the ratio $\sigma(D_s^+)/(\sigma(D^0) + \sigma(D^+)) = 0.28 \pm 0.10 \pm 0.05$ is in agreement within one standard deviation with the predicted value of 0.20 [1] and within 1.6 standard deviations with the world average value of 0.10 ± 0.02 of measurements in e^+e^- collisions[11].

8.4 Fraction of vector mesons

From a polarization state counting the fraction of vector mesons in the charm meson production is expected to be $P_V = 3/4$ [1]. The world average measured in e^+e^- collisions is different, $P_V = 0.59 \pm 0.01$ [4]. The difference comes probably from the fact that charmed vector mesons are heavier than the corresponding pseudo-scalar particles and therefore the available phase space enhances the production of ground state mesons.

P_V can be determined from the production cross sections of the scalar and vector charged and neutral mesons

$$P_V = \frac{\sigma(D^{*0}) + \sigma(D^{*+})}{\sigma(D^0) + \sigma(D^+)} \quad (8.1)$$

because all the vector mesons decay into ground state pseudo-scalar mesons.

If the isospin invariance is assumed, the same number of charged and neutral particles is expected from the hadronisation and two cross sections in combination with the known branching fractions are sufficient to extract the value of P_V . From our cross section measurements P_V can be extracted in three, although not statistically independent ways:

$$R_1 = \frac{\sigma(D^+)}{\sigma(D^0)} \quad P_V = \frac{1 - R_1}{(1 + R_1) Br_{(D^{*+} \rightarrow D^0)}} = 0.62 \pm 0.08 \pm 0.04 \quad (8.2)$$

$$R_2 = \frac{\sigma(D^{*+})}{\sigma(D^0)} \quad P_V = \frac{R_2}{1 - R_2 \cdot Br_{(D^{*+} \rightarrow D^0)}} = 0.65 \pm 0.22 \pm 0.10 \quad (8.3)$$

$$R_3 = \frac{\sigma(D^{*+})}{\sigma(D^+)} \quad P_V = \frac{R_3}{1 + R_3 \cdot Br_{(D^{*+} \rightarrow D^0)}} = 0.63 \pm 0.09 \pm 0.05 \quad (8.4)$$

The errors were calculated from the uncertainties on the ratios by using the standard error propagation method. It is interesting to see, that the error, when P_V is determined from R_2 is much higher than when it is determined from R_3 , although the precision of the measurement of $\sigma(D^+)$ is about the same as for the measurement of $\sigma(D^0)$. The values of P_V determined in three different ways (Eqs. 8.2–8.4) are in good agreement with the world average from e^+e^- colliders, $P_V = 0.59 \pm 0.01$ [4].

8.5 Leading to non-leading particle asymmetries

The leading to non-leading particle asymmetries are presented in Table 8.4 together with the predictions of PYTHIA. The PYTHIA values for all D-mesons are in good agreement with the measured results.

	D^0	D^+	D^{*+}	D_s^+
Measurement	$0.10 \pm 0.09 \pm 0.01$	$0.25 \pm 0.10 \pm 0.01$	$0.24 \pm 0.18 \pm 0.01$	$0.20 \pm 0.33 \pm 0.04$
PYTHIA	0.24	0.22	0.23	-0.06

Table 8.4: Leading to non-leading particle asymmetries in the range of $-0.15 < x_F < 0.05$. For the D_s^+ the anti-particle cross section was used for σ_{LP} in Eq. 5.9

8.6 A-dependence parameter α

The result for the A-dependence is $\alpha = 0.98 \pm 0.04 \pm 0.03$. The only previously published measurement in pA reactions is the result of E789, $\alpha = 1.02 \pm \pm 0.03 \pm 0.02$. Our value is of about the same accuracy and is in good agreement with this result. It is also in agreement with the assumption of linear dependence of cross sections, $\alpha = 1$.

9 Summary

We measured the total and single differential cross sections σ , $d\sigma/dp_T^2$ and $d\sigma/dx_F$, the A-dependence of the cross sections and the leading to non-leading particle asymmetries for the production of D^0 , D^+ , D_s^+ and D^{*+} mesons in pA collisions at a proton energy of 920 GeV.

The total cross sections per nucleon (in μb) are: $48.7 \pm 4.7 \pm 6.2$, $20.0 \pm 2.0 \pm 2.9$, $18.5 \pm 6.4 \pm 3.9$ and $22.0 \pm 4.7 \pm 3.5$ for the D^0 , D^+ , D_s^+ and D^{*+} respectively, in good agreement with previous measurements. The total cross section for the charm quark pair production is $\sigma(c\bar{c}) = 48.9 \pm 4.6 \pm 6.9 \mu\text{b}$.

The measured values for the ratio $\sigma(D^+)/\sigma(D^0) = 0.41 \pm 0.06 \pm 0.02$ and $\sigma(D^{*+})/\sigma(D^0) = 0.45 \pm 0.11 \pm 0.05$ are in agreement with the average of the previous experiments, and match also the predictions of the simple isospin model. Our result for the ratio $\sigma(D_s^+)/(\sigma(D^0) + \sigma(D^+)) = 0.28 \pm 0.10 \pm 0.05$ is in agreement within one standard deviation with the prediction of 0.2 [1] and within 1.6 standard deviations with the world average value of 0.10 ± 0.02 of measurements in e^+e^- collisions [11].

The fraction of vector mesons, determined in three different ways, is $P_V(D^+, D^0) = 0.62 \pm 0.08 \pm 0.04$, $P_V(D^{*+}, D^0) = 0.65 \pm 0.22 \pm 0.10$ and $P_V(D^{*+}, D^+) = 0.63 \pm 0.09 \pm 0.05$ and is also in good agreement with the measurements in e^+e^- collisions.

The result for the A-dependence, $\alpha = 0.98 \pm 0.04 \pm 0.03$, is again in good agreement with the previous measurement, as well as with the assumption of a linear dependence of cross sections, $\alpha=1$. The measured leading to non-leading particle asymmetries are in good agreement with the predictions derived from PYTHIA.

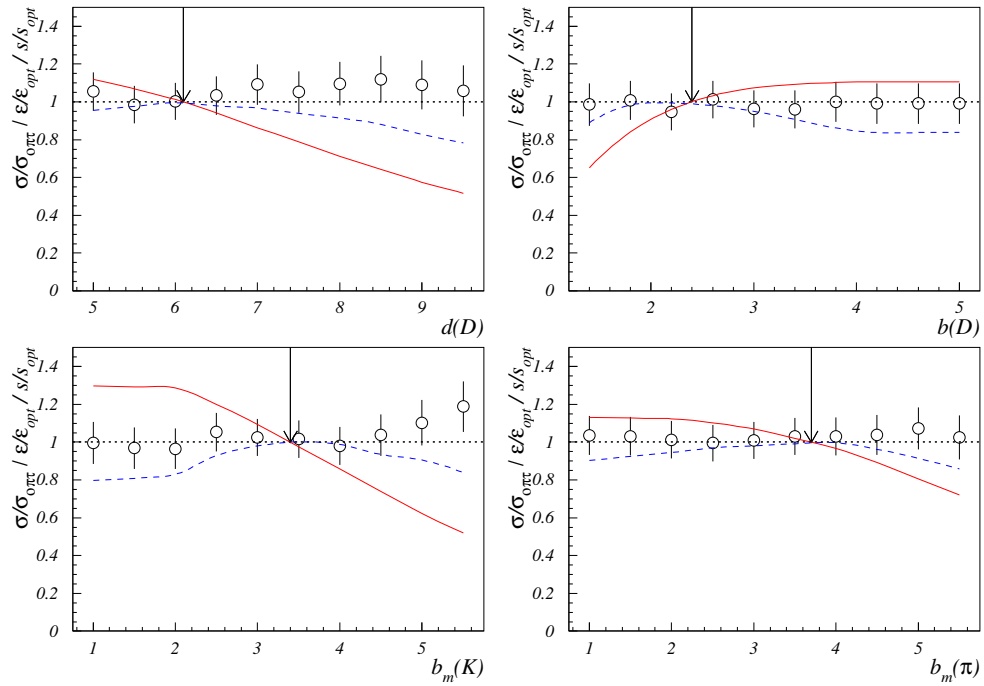
A Stability of cuts

The stability of the cuts was tested with two methods:

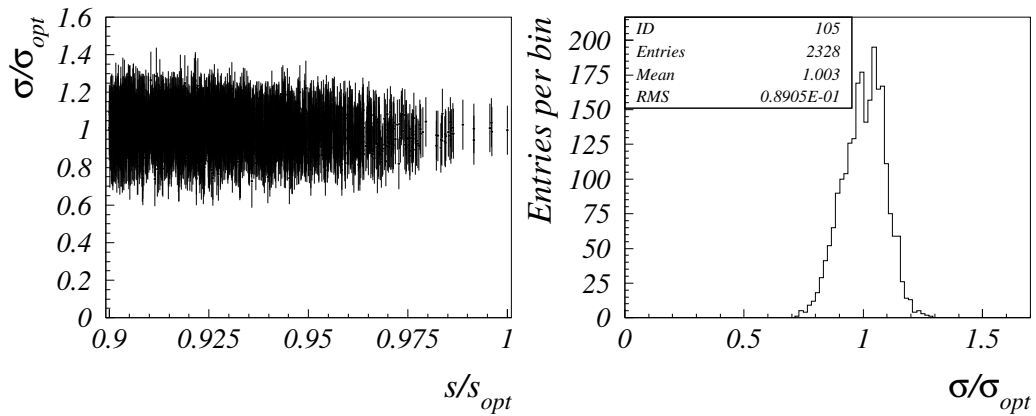
1. By varying one cut while the others were fixed at their optimized values
2. By calculating all combinations of cuts within a 3 dimensional (for D^+) or 4 dimensional (D^0 , D^{*+} and D_s^+) matrix and keeping only those with relative significance larger than 90% of the value at optimal cuts. For D_s^+ the limit was chosen at 95% of the value at optimal cuts because of the small statistics of the signal.

The results of the first method are presented in Figs. A.1a, A.2a, A.3a and A.4a. The cuts used in the various optimizations are summarized in Table 4.2. For each reconstructed type of meson, each cut is presented in a separate plot, which shows the relative cross sections σ/σ_{opt} presented with circles and error bars as a function of the cut. The relative significance s/s_{opt} is shown as a dashed blue line and the relative efficiency ϵ/ϵ_{opt} as a solid red line. The horizontal dashed line shows the normalization. The cut value at the highest significance is indicated with an arrow. The cross section is calculated as the ratio of the number of reconstructed events in real data and Monte Carlo. The cross section, the efficiency and the significance are normalized to the values, where the significance is at its maximum. All stability plots show a stable behavior of the cross section. The variations do not exceed 15 %.

For the second type of stability plots, two histograms are presented per optimization, one for each D-meson type: The relative cross section σ/σ_{opt} is plotted as a function of the relative significance s/s_{opt} and the distribution of the cross sections for all cut combinations is shown, where the relative significance exceed 90%. The mean and the r.m.s. of these distributions are indicators of the systematic error on the cross section coming from the cut optimization. The results are shown in Figs. A.1b, A.2b, A.3b, A.4b and the results are summarized in Table A.1. The mean value of the cross sections for D^+ and D^0 is close to the value at the optimized cuts, while for D_s^+ and D^{*+} the mean is lower for about one sigma.



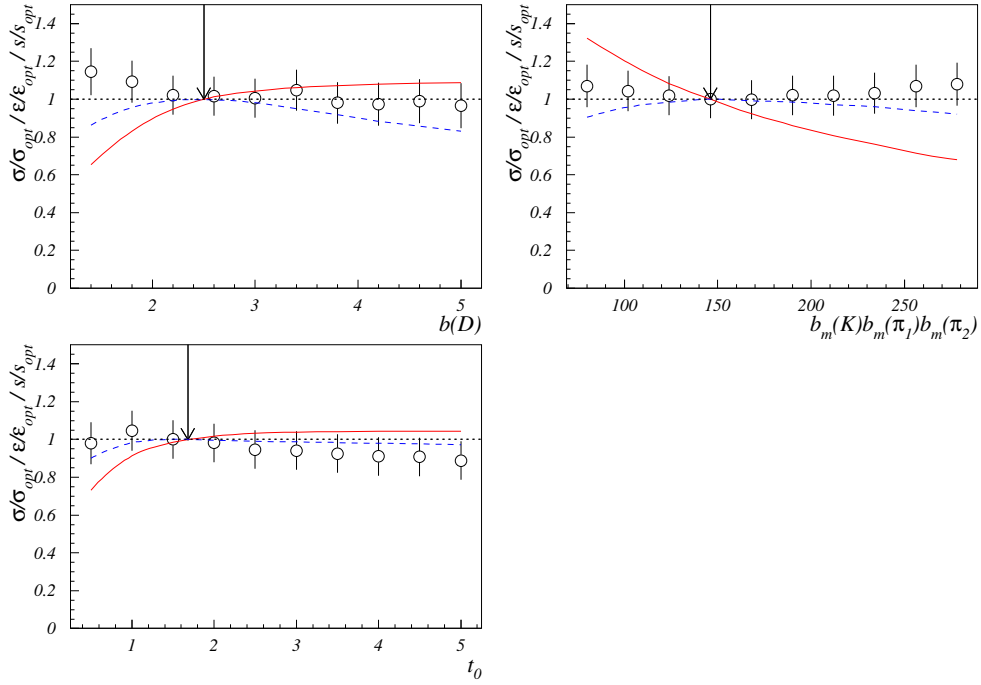
(a) With method 1



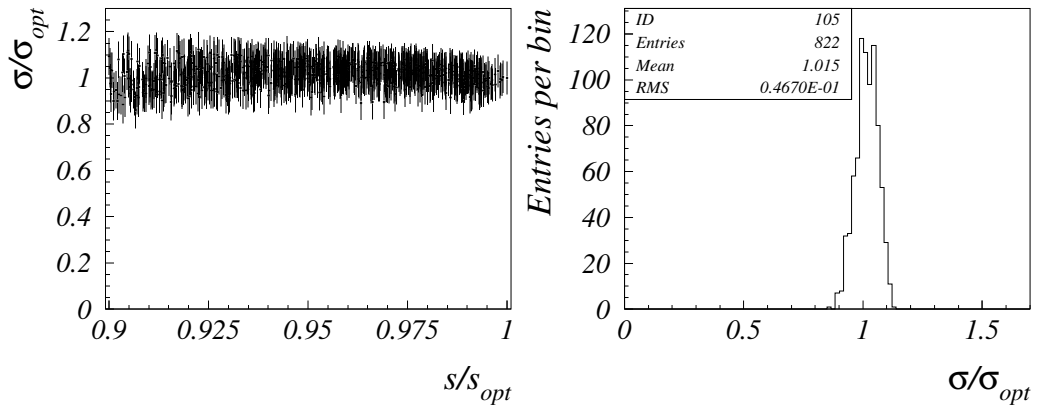
(b) With method 2

Figure A.1: Stability of analysis cuts in the reconstruction of $D^0 \rightarrow K^- \pi^+$.

dp

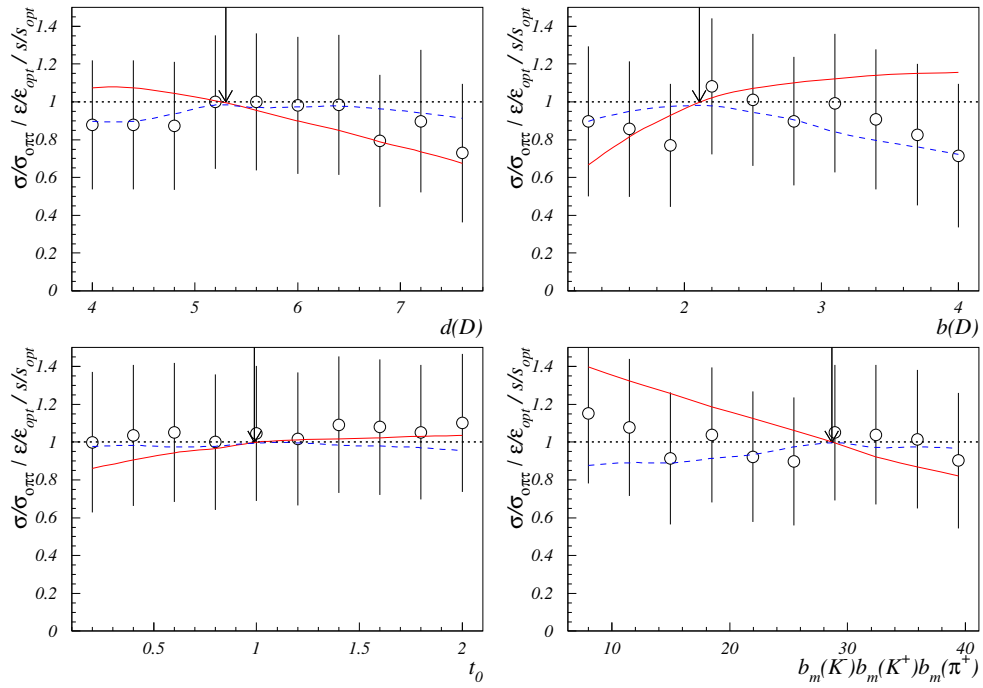


(a) With method 1

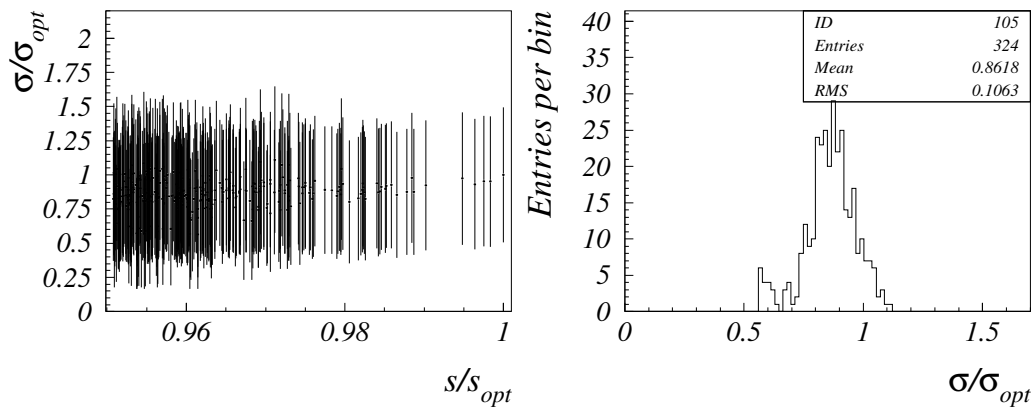


(b) With method 2

Figure A.2: Stability of analysis cuts in the reconstruction of $D^+ \rightarrow K^- \pi^+ \pi^+$.

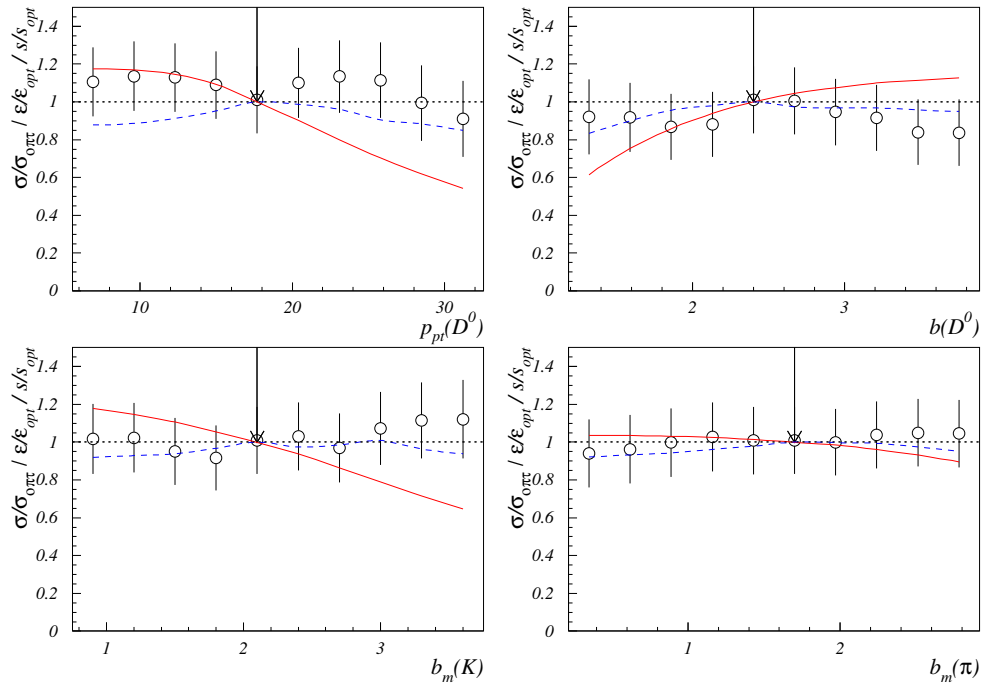


(a) With method 1

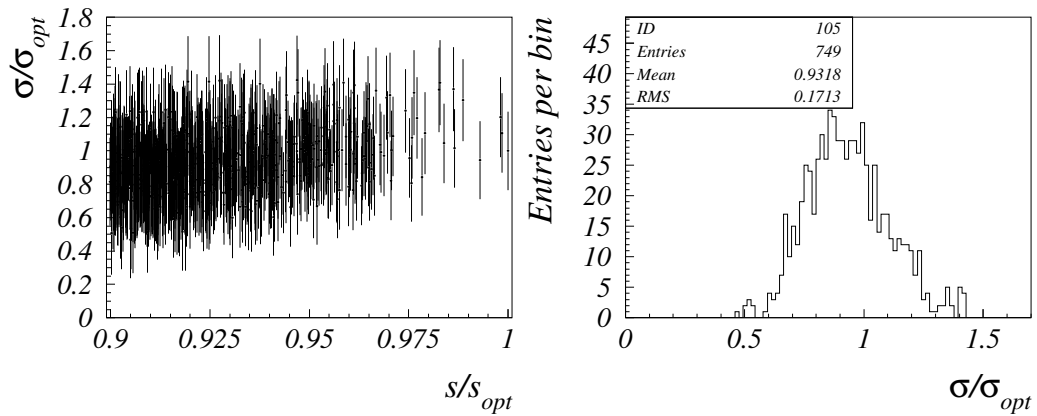


(b) With method 2

Figure A.3: Stability of analysis cuts in the reconstruction of $D_s^+ \rightarrow K^- K^+ \pi^+$.



(a) With method 1



(b) With method 2

Figure A.4: Stability of analysis cuts in the reconstruction of $D^{*+} \rightarrow D^0\pi \rightarrow K^-\pi^+\pi^+$.

	mean	r.m.s
D^0	1.00	0.09
D^+	1.02	0.05
D^{*+}	0.93	0.17
D_s^+	0.86	0.11

Table A.1: The mean and the r.m.s. of the distributions of the relative cross sections calculated on a multi-dimensional matrix.

meson	signal window [MeV]	side bands [MeV]
D^0	$ \Delta m < 75$	$75 < \Delta m < 150$
D^+	$ \Delta m < 50$	$50 < \Delta m < 100$
D_s^+	$ \Delta m < 33$	$45 < \Delta m < 66$
D^{*+}	$ \Delta q < 2.5$	

Table B.1: Window sizes used in the comparison.

B Comparison between MC and data

The agreement between real data and Monte Carlo was checked by comparing the distributions of some relevant variables after the analysis cuts had been applied. To get the distribution for signal events of a given variable, two histograms were filled first: one with events from the signal window and the other one with the events from sidebands. Then the distribution for side bands was subtracted from the distribution for signal window. The window sizes are summarized in Table B.1. For D^{*+} instead of sidebands the wrong sign combinations in the signal window were used.

Since the fractions of generated signal events per wire differ from that in real data, for the Monte Carlo we filled the histograms separately for each wire and then took the weighted sum, with the weights:

$$f_i = p_i/n_i \tag{B.1}$$

where $p_i = \frac{A_i \mathcal{L}_i}{\sum_i A_i \mathcal{L}_i}$ is the fraction of signal events in real data for i^{th} wire (assuming linear A-dependence) and $n_i = \frac{N_i}{\sum_i N_i}$ is the fraction of Monte Carlo events per wire i . The distribution from Monte Carlo was finally normalized to the same number of events as in the real data and plotted together with the real data distribution. Real data are shown with error bars and Monte Carlo with error boxes. For each distribution also the $\chi^2/n.d.f.$ was calculated and printed in each plot. It was calculated by:

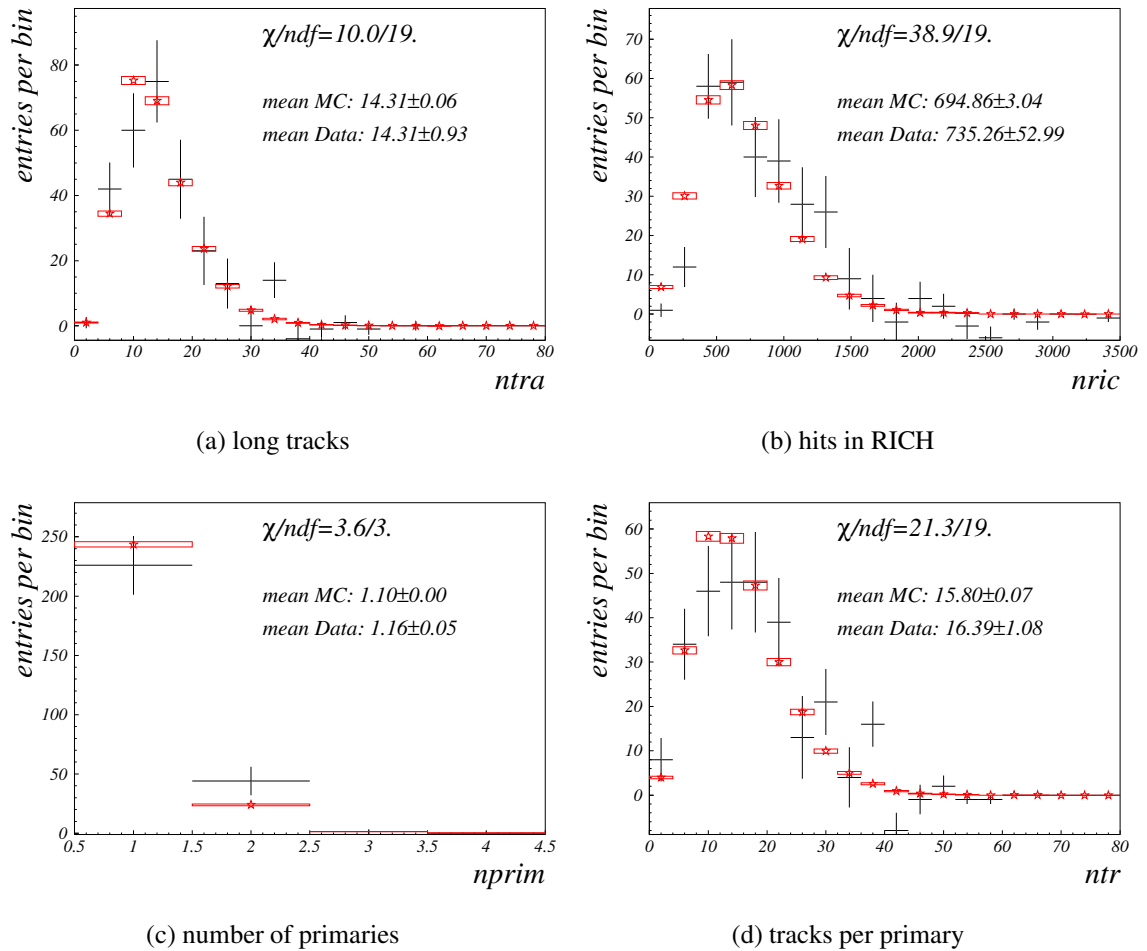
$$\chi^2 = \sum_i \frac{(n_i^{DATA} - n_i^{MC})^2}{\sigma_i^2} \quad (\text{B.2})$$

where n_i is the i^{th} bin content and σ_i the error for real data bins.

The following distributions have been checked:

- Event multiplicities (Fig. B.1)
- Momentum (Figs. B.2, B.3 and B.4)
- Transverse momentum (Figs. B.5 and B.6)
- Impact parameter significance of kaons and pions (Figs. B.7 and B.8)
- Product of cuts (Fig. B.9)
- Impact parameter significances of D-mesons (Fig. B.10)
- Distance significances (Fig. B.11)

For all distributions a good agreement between the real data and Monte Carlo has been found.

**Figure B.1:** Comparison of event multiplicities.

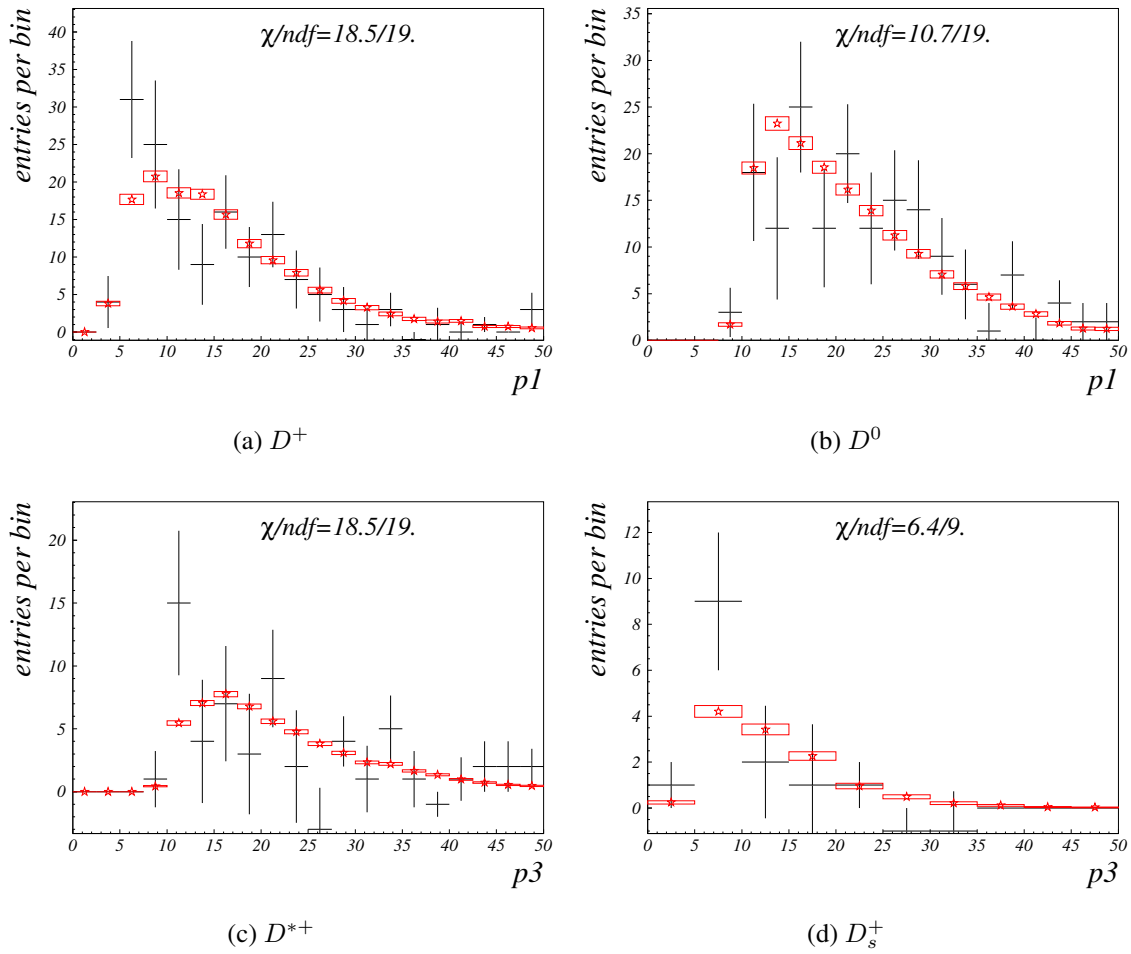


Figure B.2: Comparison of momentum distributions of kaons.

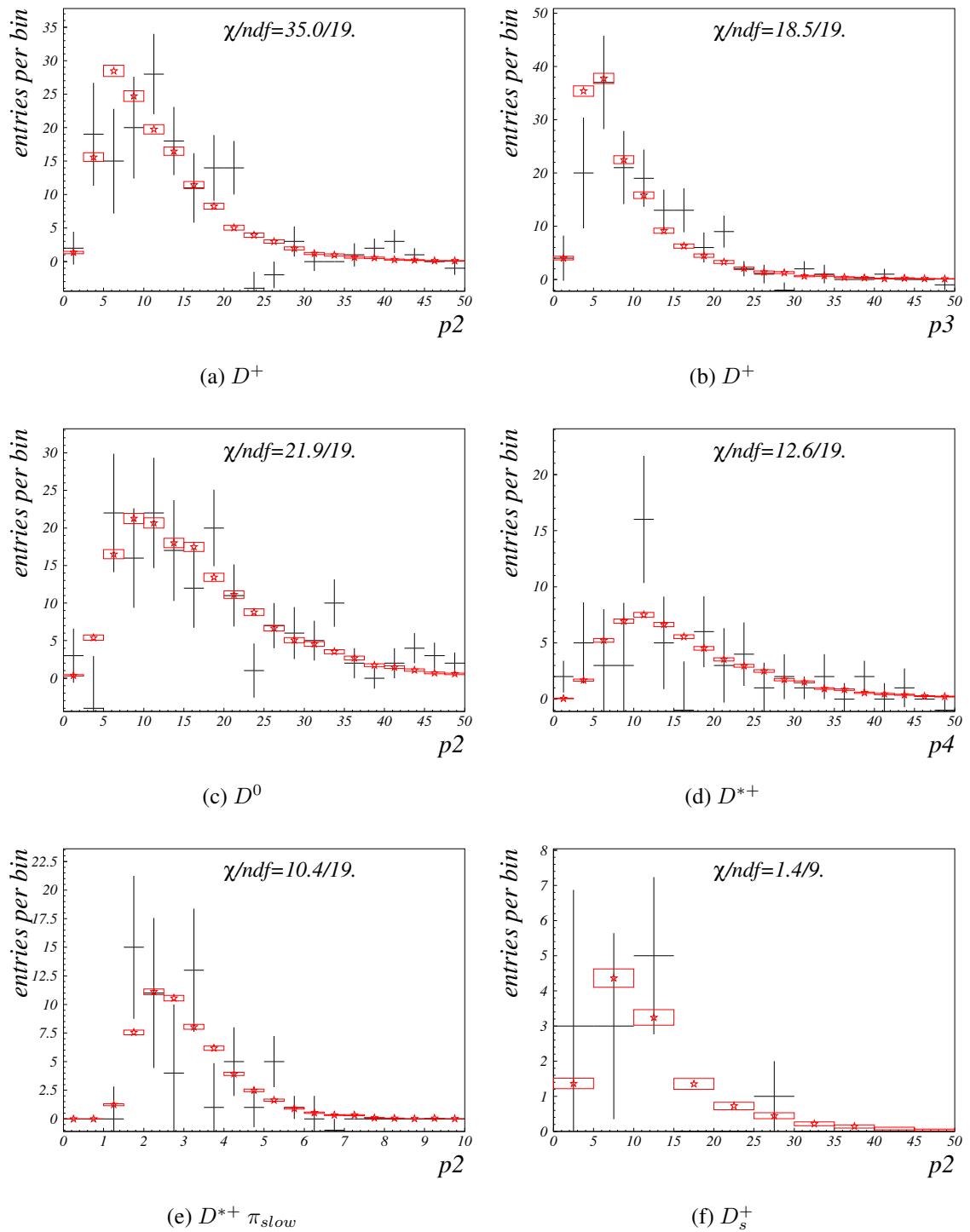


Figure B.3: Comparison of momentum distributions of pions.

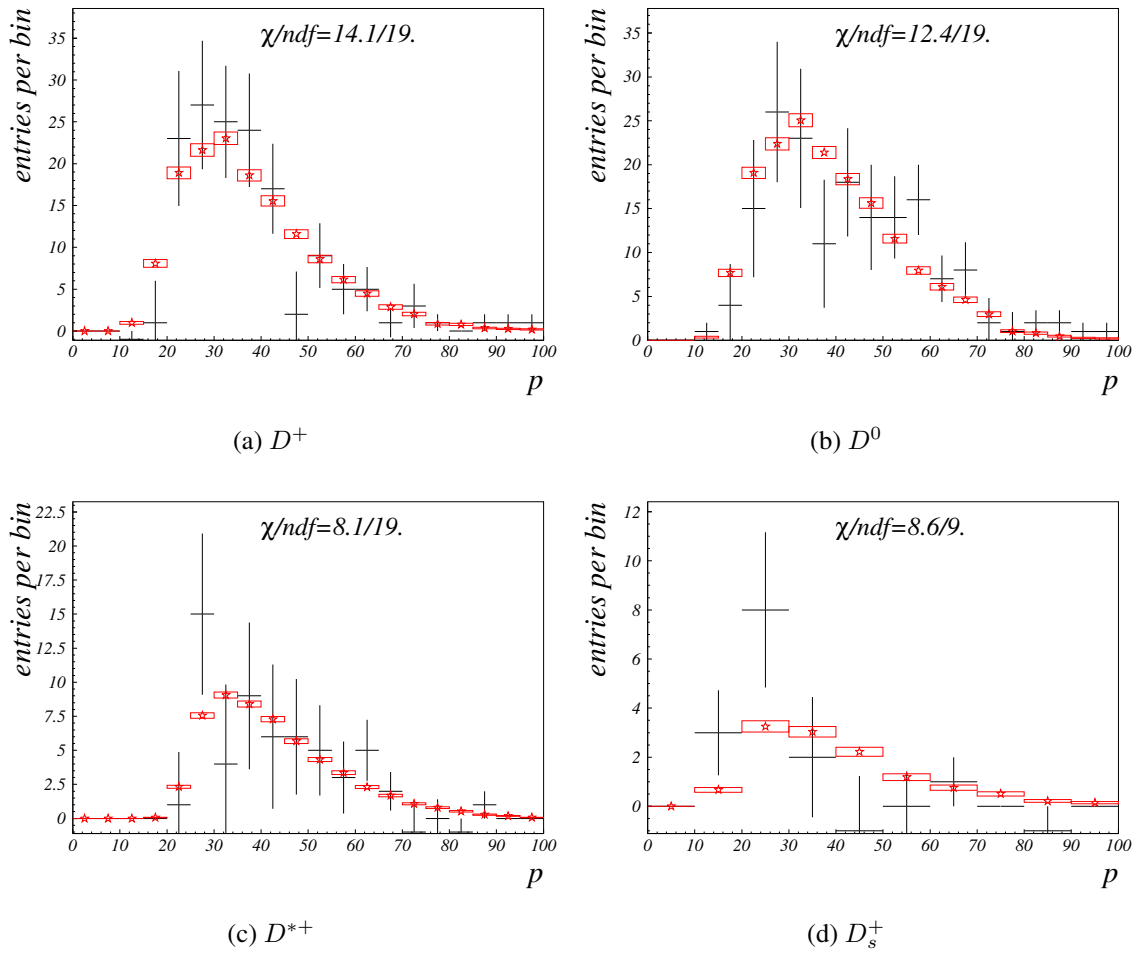


Figure B.4: Comparison of momentum distributions of D-mesons.

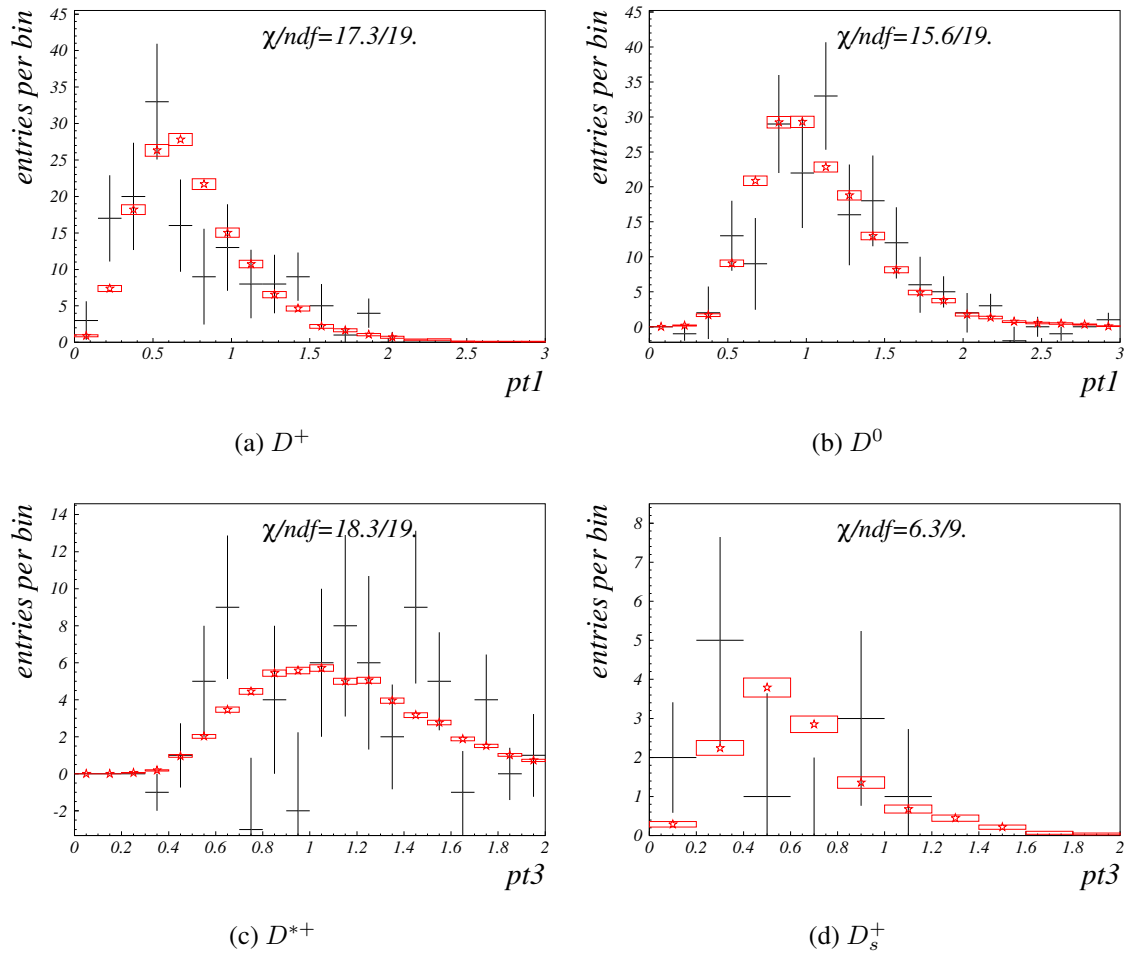


Figure B.5: Comparison of transversal momentum distributions of kaons.

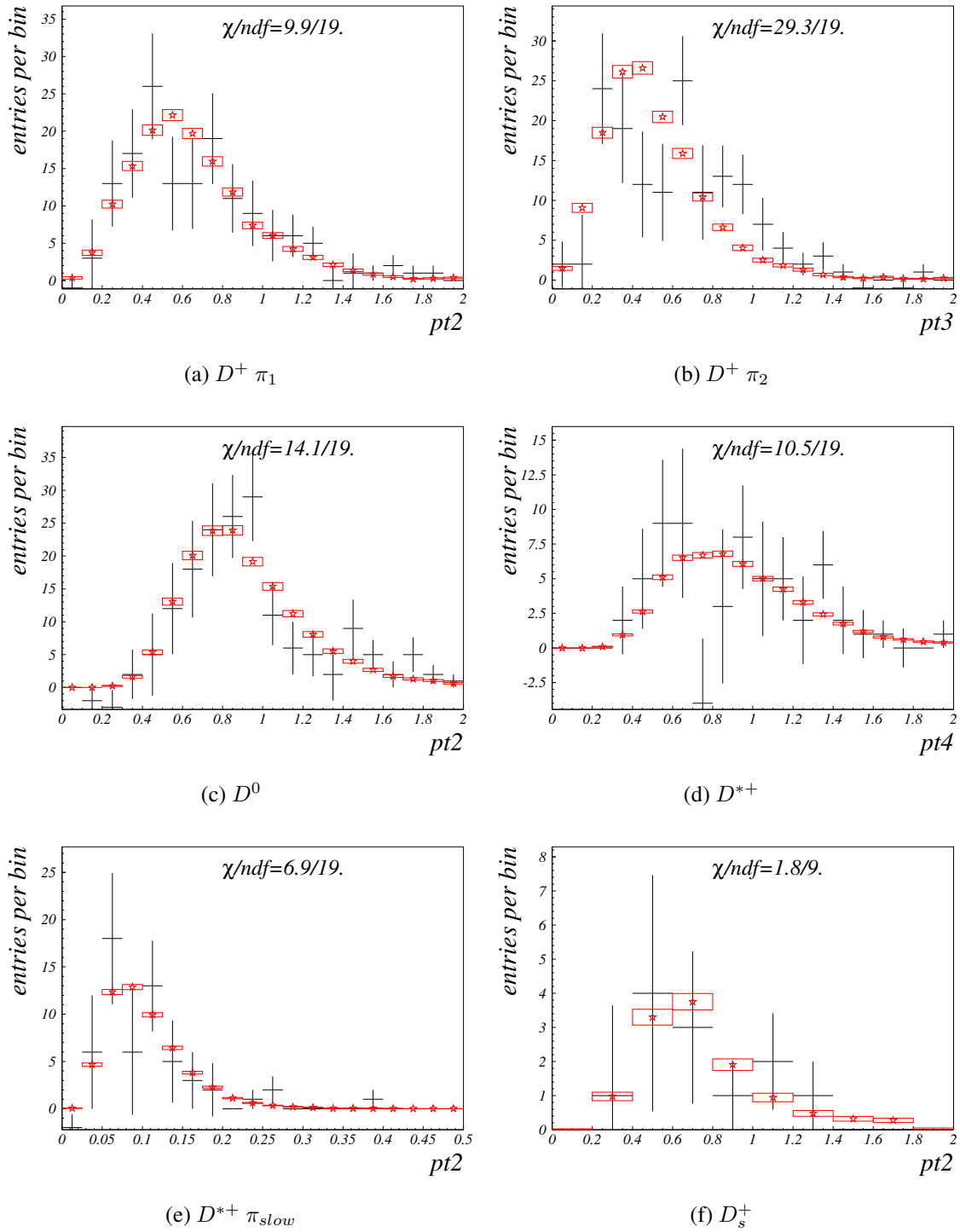


Figure B.6: Comparison of transversal momentum distributions of pions.

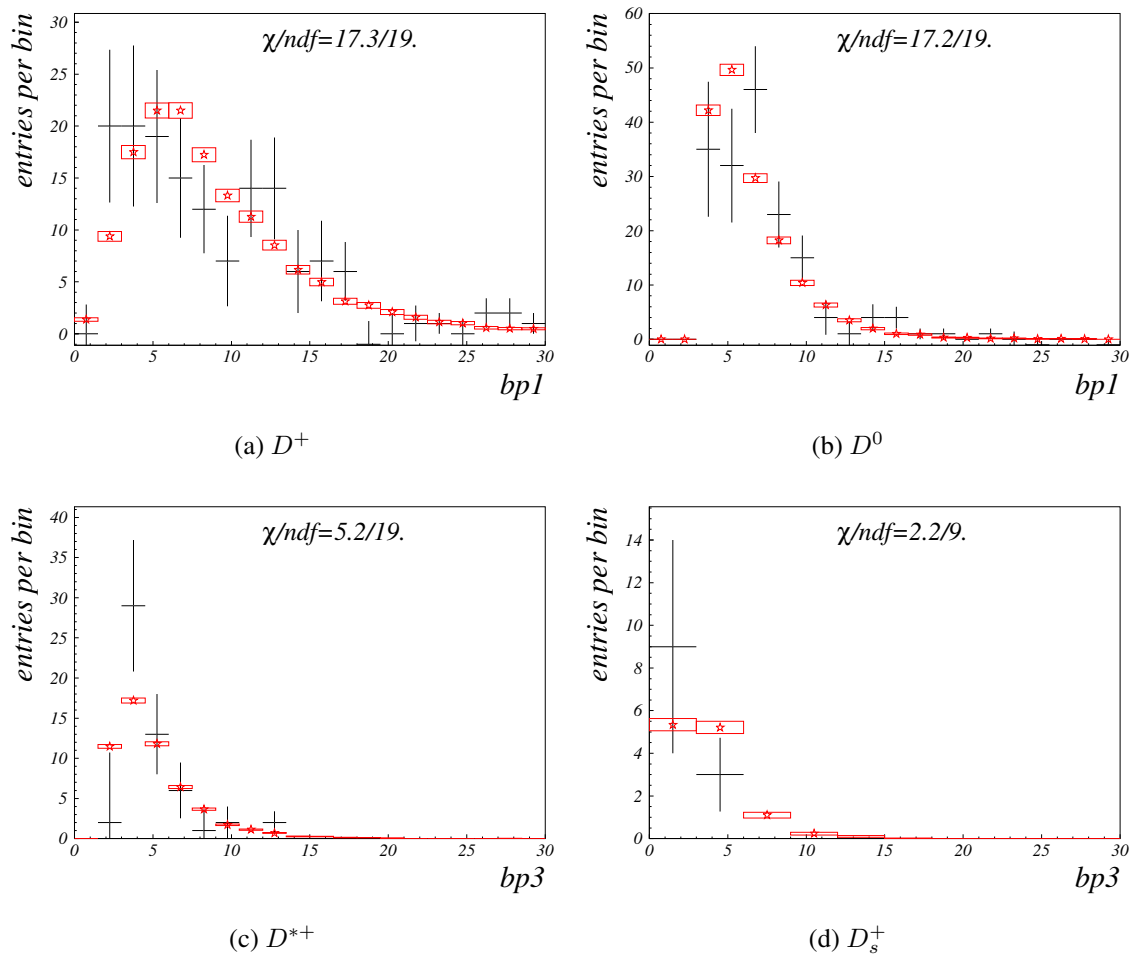


Figure B.7: Comparison of impact parameter significance distributions of kaons.

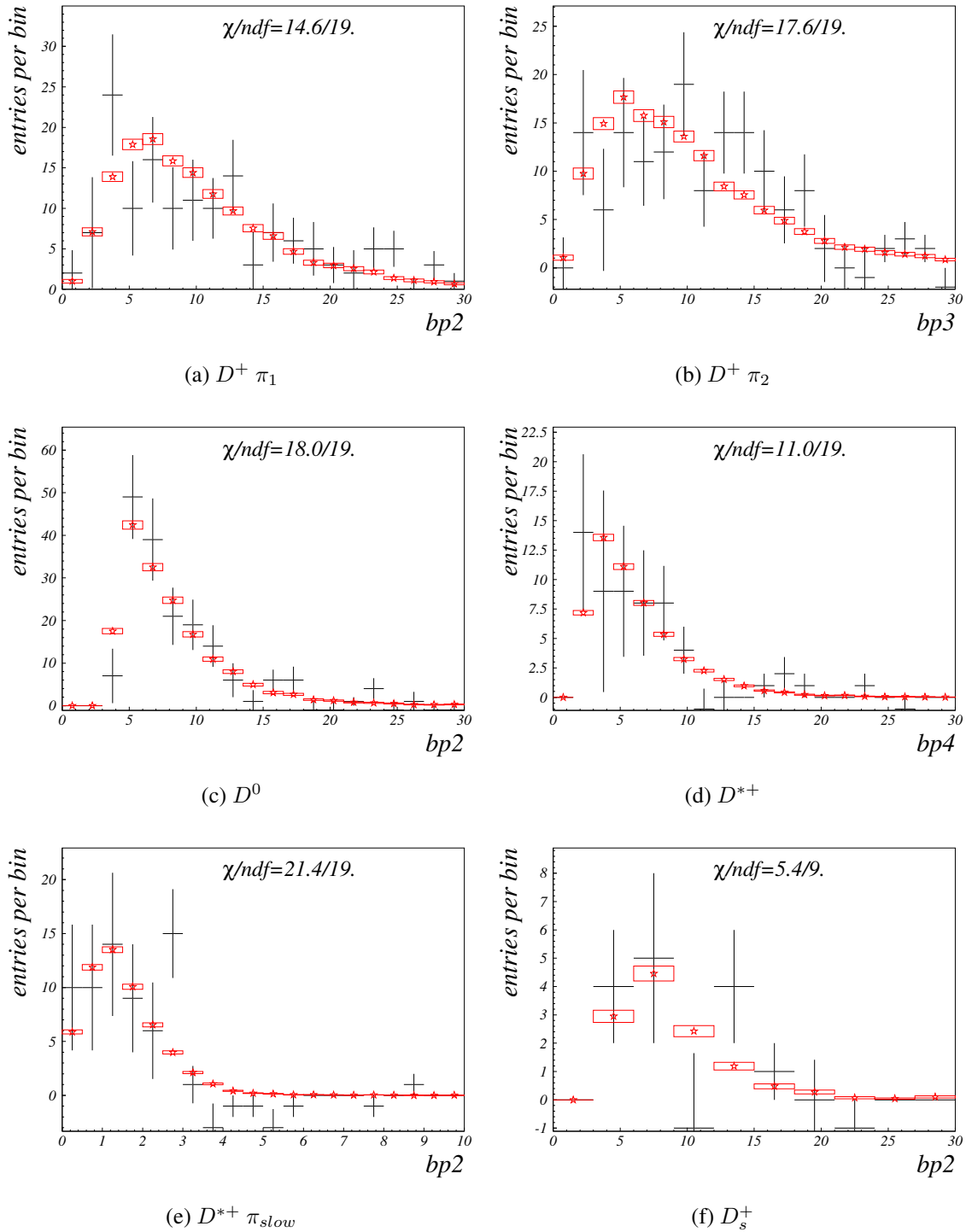


Figure B.8: Comparison of impact parameter significance distributions of pions.

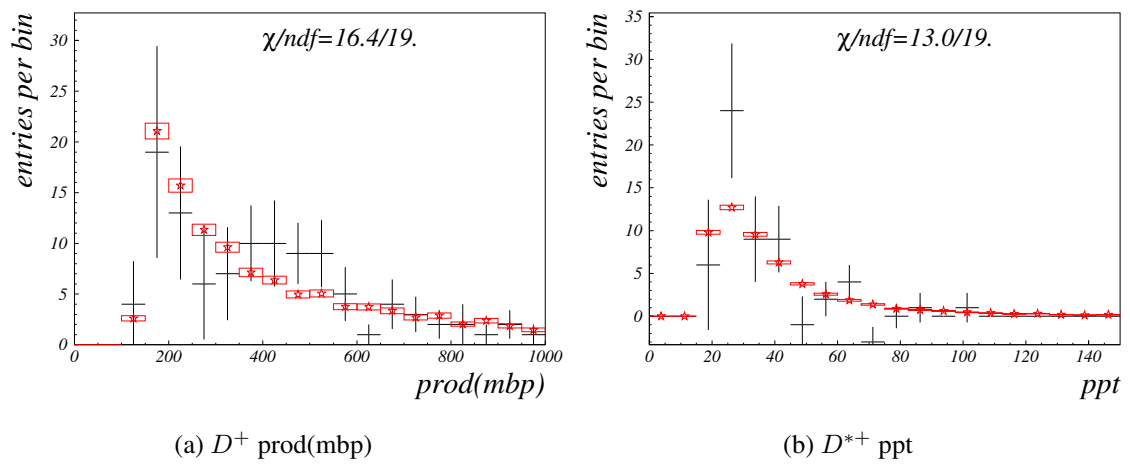


Figure B.9: Comparison of product of impact parameter significances (a) and momentum dependent p_T -cut (b).

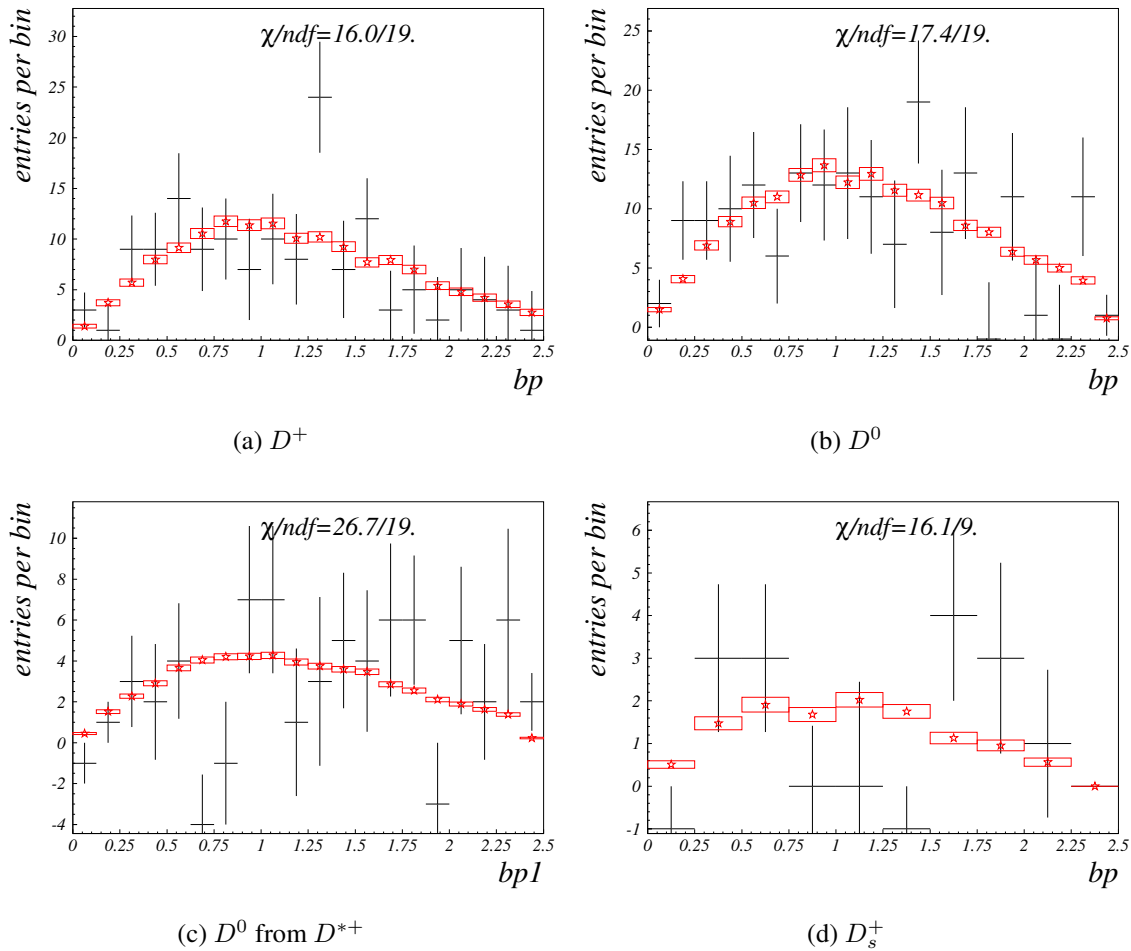
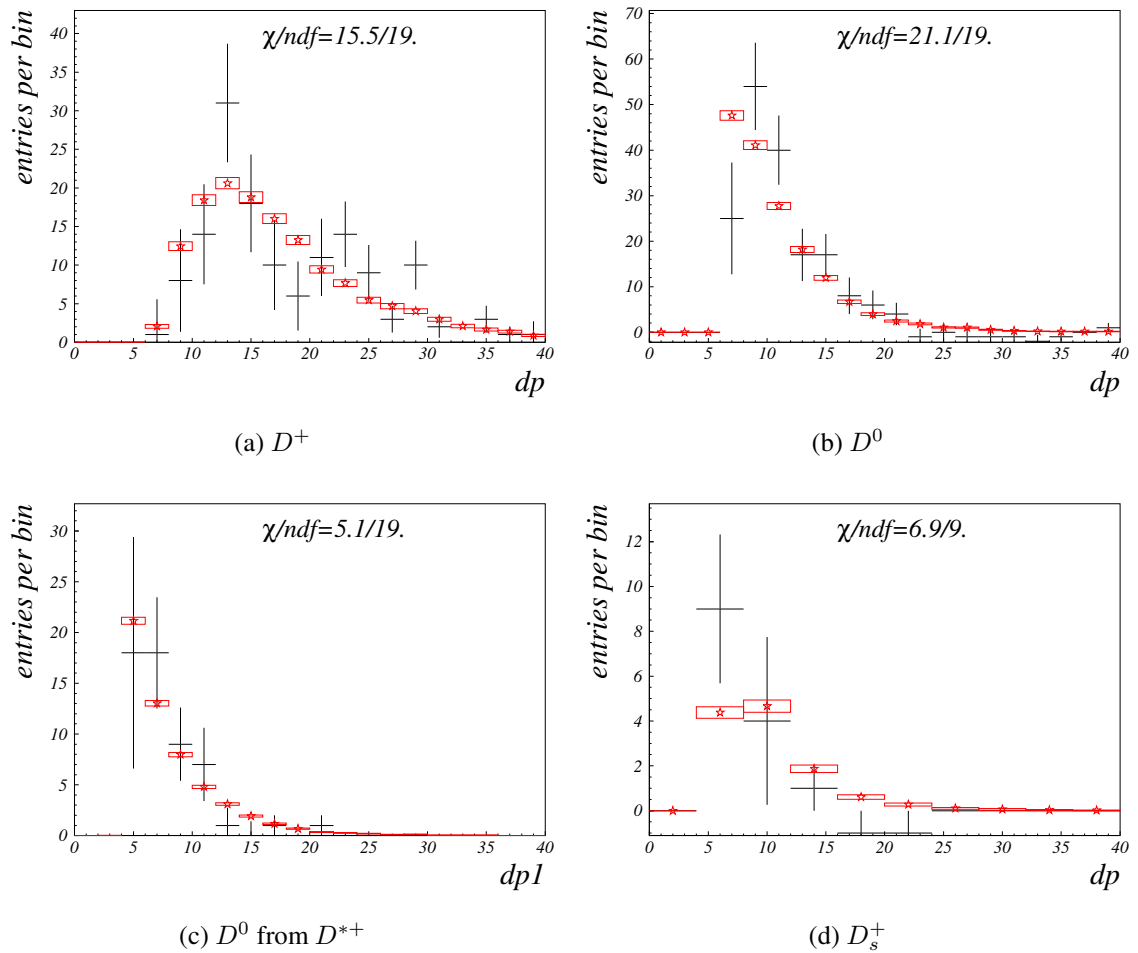


Figure B.10: Comparison of impact parameter significance distributions of D mesons.

**Figure B.11:** Comparison of distance significance distributions of D mesons.

References

- [1] S. Frixione, M. L. Mangano, P. Nason and G. Ridolfi, *Adv. Ser. Direct. High Energy Phys.* **15** (1998) 609 [arXiv:hep-ph/9702287].
- [2] P. Nason, *To appear in the proceedings of 8th International Symposium on Heavy Flavor Physics (Heavy Flavors 8), Southampton, England, 25-29 Jul 1999.*
- [3] P. Nason, S. Dawson and R. K. Ellis, FERMILAB-Pub-87/222T 1987
- [4] C. Lourenco, H. Woehri, C. Lourenco and H. K. Wohri, *Phys. Rept.* **433** (2006) 127 [arXiv:hep-ph/0609101].
- [5] J. Hinchliffe, J. Womersley, hep-ex/0612006v1, December 1996.
- [6] A. Pich, [arXiv:hep-ph/0001118].
- [7] C. Lourenco, H. Woehri, CERN-EP/2003-xxx, January 2003.
- [8] M. E. Peskin and D. V. Schroeder, *Reading, USA: Addison-Wesley (1995) 842 p.*
- [9] R.P. Feynman, *Acta Phys. Polonica* 24, 697(1963).
- [10] T. Sjostrand, L. Lonnblad and S. Mrenna, [arXiv:hep-ph/0108264].
- [11] W-M Yao *et al.* [Particle Data Group Collaboration], *J. Phys. G: Nucl. Part. Phys* **33** 1.
- [12] G. A. Alves *et al.* [E769 Collaboration], *Phys. Rev. Lett.* **77**, 2388 (1996) [Erratum-ibid. **81**, 1537 (1998)].
- [13] M. Aguilar-Benitez *et al.* [LEBC-EHS Collaboration], *Phys. Lett. B* **135**, 237 (1984).
- [14] M. Aguilar-Benitez *et al.* [LEBC-EHS Collaboration], *Z. Phys. C* **40**, 321 (1988).
- [15] R. Ammar *et al.*, *Phys. Rev. Lett.* **61**, 2185 (1988).
- [16] K. Kodama *et al.* [Fermilab E653 Collaboration], *Phys. Lett. B* **263**, 573 (1991).
- [17] M. J. Leitch *et al.* [E789 Collaboration], *Phys. Rev. Lett.* **72** (1994) 2542.

- [18] P. Nason, S. Dawson, R. K. Ellis, Fermilab-PUB-89/91-T, BNL-42398.
- [19] D. Dujmić, PhD Thesis Hamburg 2001
- [20] P. Conde Muino, PhD Thesis, Hamburg 2002
- [21] A. Gorišek, PhD Thesis, Ljubljana 2003
- [22] A. Bogatyrev, HERA-B internal presentations, 2003-2006
- [23] T. Lohse et al., “An Experiment to Study CP Violation in the B System Using an Internal Target at the HERA Proton Ring. Proposal, DESY-PRC 94-02 (1994).
- [24] T. Lohse et al., “An Experiment to Study CP Violation in the B System Using an Internal Target at the HERA Proton Ring. Design Report”, DESY-PRC 95/01 (1995).
- [25] I. Bigi, A. I. Sanda, “CP violation in heavy flavor decays, Predictions and search strategies”. Nucl. Phys., B (55 p), 1986.
- [26] I. Abt *et al.* [HERA-B Collaboration], Phys. Rev. D **73** (2006) 052005 [arXiv:hep-ex/0512030].
- [27] K. Hagiwara *et al.* [Particle Data Group Collaboration], Phys. Lett. B **592** (2004).
- [28] K. Ehret, Nucl. Instrum. Meth. A **446** (2000) 190.
- [29] C. Bauer *et al.*, Nucl. Instrum. Meth. A **501** (2003) 39.
- [30] W. Gradl, Nucl. Instrum. Meth. A **461** (2001) 80.
- [31] H. Albrecht *et al.* [HERA-B Outer Tracker Group], [arXiv:physics/0507048].
- [32] H. Albrecht *et al.*, Nucl. Instrum. Meth. A **541** (2005) 610 [arXiv:physics/0412064].
- [33] H. Albrecht *et al.* [HERA-B Outer Tracker Group], [arXiv:physics/0701122].
- [34] I. Arino *et al.*, Nucl. Instrum. Meth. A **516** (2004) 445 [arXiv:hep-ex/0303012].
- [35] G. Avoni *et al.*, Nucl. Instrum. Meth. A **461** (2001) 332.
- [36] V. Eiges *et al.*, Nucl. Instrum. Meth. A **461** (2001) 104.
- [37] M. Dam *et al.*, Nucl. Instrum. Meth. A **525** (2004) 566.
- [38] I. Abt *et al.*, Luminosity determination at HERA-B, submitted to Elsevier Science (2007)
- [39] H. Albrecht, S. Nowak, HERA-B note 95-065 ARTE 1995.
- [40] H. Pi, Comp. Phys. Commun.71, 173(1992).

-
- [41] R. Brun *et al.*, GEANT3, Internal Report CERN-DD/EE/84-1, CERN(1987).
- [42] H. Emiliyanov *et al.*, Grover, HERA-B internal note.
- [43] M. Starič “How to combine different wires”, Hera B Week Jan. 2005, Oral presentation.
- [44] R. Brun, O. Couet, C. Vandoni, and P. Zanmarini, ”PAW - Physics Analysis Workstation, The Complete Reference,” Version 1.07, CERN, Geneva, Switzerland, October 1989.
- [45] E. M. Aitala *et al.* [E791 Collaboration], Phys. Lett. B **462**, 225 (1999). [arXiv:hep-ex/9906034].
- [46] I. Abt *et al.* [HERA-B Collaboration], Eur. Phys. J. C **50** (2007) 315 [arXiv:hep-ex/0606049].
- [47] A. F. Wallace, FERMILAB-THESIS-1997-29.
- [48] B. Schwingenheuer, “Measurements of open charm cross sections with HERA-B” HERA-B note 2006.

Povzetek doktorskega dela

V doktorski disertaciji obravnavam meritev produkcijskih presekov mezonov D pri trkih protonov energije 920 GeV z jedri v mirujoči tarči. Merski podatki so bili zajeti s spektrometrom HERA-B na inštitutu DESY v Hamburgu jeseni 2002. V vzorcu je približno 180 milijonov dogodkov. Za tarčo so služile žice iz treh različnih materialov, ki so bile postavljene okoli curka protonov.

Komponente detektorja HERA-B delimo na dve glavni skupini: komponente za merjenje sledi nabitih delcev in komponente za identifikacijo delcev. Sledilni sistem sestavljajo detektor verteksov (VDS), notranji (ITR) in zunanji (OTR) sledilni sistem in dipolni magnet. Komponente sistema za identifikacijo delcev pa so števec Čerenkovih obročev (RICH), elektromagnetni kalorimeter (ECAL) in mionski detektor (MUON).

Značilno za neelastične trke protonov z jedri je veliko število delcev, ki nastanejo pri reakciji. Iz njih moramo izbrati le tiste, ki pripadajo iskanemu razpadu. Pričakujemo, da je presek za produkcijo kvarka c za 2 do 3 velikostne razrede manjši od neelastičnega preseka, poleg tega so razvejitvena razmerja razpadov majhna. Zato potrebujemo pri rekonstrukciji razpada ostre reze na merjenih količinah, da ločimo delce iz razpada mezona D od ostalih nabitih delcev. Določili smo produkcijske preseke za štiri mezone D , ki so bili rekonstruirani v naslednjih razpadnih kanalih:

- $D^0 \rightarrow K^- \pi^+$
- $D^+ \rightarrow K^- \pi^+ \pi^+$
- $D_s^+ \rightarrow \phi \pi^+ \rightarrow (K^- K^+) \pi^+$
- $D^{*+} \rightarrow D^0 \pi^+ \rightarrow (K^- \pi^+) \pi^+$

Razvejitvena razmerja so zbrana v tabeli I.

Poenostavljeni izospinski model napoveduje za razmerje med preseki mezonov D^+ in D^0 vrednost 0.42 in za razmerje D^{*+} in D^0 vrednost 0.46 [4]. Napoved za razmerje preseka D_s^+ in vsoto presekov D^0 in D^+ je 0.2 [1].

Za določitev izkoristka in za optimizacijo selekcijskih rezov smo uporabili dogodke iz simulacije Monte Carlo. Rekonstrukcija realnih podatkov in simulacije Monte Carlo je bila narejena z isto programsko kodo.

Razvejitevna razmerja [%]			
$D^0 \rightarrow K^- \pi^+$	$D^+ \rightarrow K^- \pi^+ \pi^+$	$D_s^+ \rightarrow \phi \rightarrow K^+ K^- \pi^+$	$D^{*+} \rightarrow D^0 \rightarrow K^- \pi^+ \pi^+$
3.80 ± 0.07	9.51 ± 0.34	2.16 ± 0.28	2.57 ± 0.05

Tabela I: Razvejitevna razmerja [11]

Rekonstrukcija mezonov D

Mezoni D^0 , D^+ in D_s^+ so razmeroma dolgoživi delci, zato v rekonstrukciji zahtevamo, da njihovi razpadni produkti izhajajo iz točke (sekundarni vertex), ki je ločena od interakcijske točke protona z jedrom (primarni vertex). Zahtevali smo, da dogodek vsebuje vsaj en rekonstruiran primarni vertex.

Rekonstruirane delce smo izbirali z naslednjimi zahtevami: da ima delec vsaj 5 zadetkov v VDS in 10 zadetkov v OTR in ni označen kot klon, da je njegova gibalna količina manjša od 250 GeV/ c in da je kvaliteta rekonstruirane sledi $\chi^2/n.d.f < 10$.

Delce smo identificirali na podlagi informacije iz detektorja Čerenkovih obročev. Za kaone iz D^0 smo zahtevali, da je verjetnost za kaonsko hipotezo $L_K(K) > 0.5$, za kaone iz D^+ in D_s^+ pa $L_K(K) > 0.33$. Za pione, razen tistega iz razpada $D^{*+} \rightarrow D^0 \pi^+$, smo zahtevali, da je verjetnost za vsoto elektronske, mionske in pionske hipoteze $L_e(\pi) + L_\mu(\pi) + L_\pi(\pi) > 0.05$.

Izbrane kaonske in pionske kandidate smo nato kombinirali v mezone D^0 , D^+ in D_s^+ ter določili sekundarne vertexe. Za invariantne mase kombinacij smo zahtevali, da so v območju ± 0.5 GeV okrog nominalne mase ustreznega mezona D . Pri rekonstrukciji D_s^+ smo zahtevali tudi, da je invariantna masa para $K^+ K^-$ v območju mase mezona ϕ , $|\Delta m_\phi| < 10$ MeV. Kandidate D^{*+} smo dobili s kombiniranjem kandidatov D^0 in pionskih kandidatov, pri čemer smo naredili obe nabojni kombinaciji. Dogodke z napačno nabojno kombinacijo ($\bar{D}^0 \pi^+$) smo uporabljali kot oceno za ozadje v kanalu s pravilno nabojno kombinacijo.

Selekcija dogodkov

Največji delež k ozadju prispevajo delci iz interakcijske točke. To ozadje lahko zmanjšamo s zahtevki, da je (1) sekundarni vertex ločen od interakcijske točke, (2) da delci, ki tvorijo sekundarni vertex, ne izhajajo iz interakcijske točke in (3), da rekonstruirani mezon D izhaja iz interakcijske točke. Tem zahtevam zadostimo z rezi na naslednjih količinah: (1) $d(D)$, razdalja med sekundarnim in primarnim vertexom, deljena z napako, (2) $b_m(K)$, $b_m(\pi)$, vpadni parameter kaona oz. piona na najbližji primarni vertex, deljen z napako, in (3) $b(D)$, vpadni parameter mezona D na najbližji primarni vertex, deljen z napako.

Izkaže se, da je za tridelčni razpad $D^+ \rightarrow K^- \pi^+ \pi^+$ in $D_s^+ \rightarrow K^- K^+ \pi^+$ rez na produktu $b_m(K)b_m(\pi_1)b_m(\pi_2)$ oz. $b_m(K_1)b_m(K_2)b_m(\pi)$ bolj učinkovit, kakor rez na posameznih b_m . Iz dvodimenzionalnih porazdelitev tega produkta in časa razpada mezona D tudi razberemo korelacijo, ki omogoči še boljše ločevanje signala in ozadja. Poleg reza na produktu vpadnih

$D^0 \rightarrow K^- \pi^+$	$D^+ \rightarrow K^- \pi^+ \pi^+$
neoptimirani rezi	
$L_K(K) > 0.5$ $L_e(\pi) + L_\mu(\pi) + L_\pi(\pi) > 0.05$	$L_K(K) > 0.33$ $L_e(\pi) + L_\mu(\pi) + L_\pi(\pi) > 0.05$
optimirani rezi	
$d(D^0) > 6.1$ $b(D^0) < 2.4$ $b_m(K) > 3.4$ $b_m(\pi) > 3.7$	$b(D^+) < 2.5$ $b_m(K)b_m(\pi_1)b_m(\pi_2) > 146$ $\sqrt[3]{b_m(K)b_m(\pi_1)b_m(\pi_2)} > 4(t - t_0), t_0 = 1.68$
$D_s^+ \rightarrow \phi \pi^+ \rightarrow K^- K^+ \pi^+$	$D^{*+} \rightarrow D^0 \pi^+ \rightarrow K^- \pi^+ \pi^+$
neoptimirani rezi	
$L_K(K) > 0.33$ $L_e(\pi) + L_\mu(\pi) + L_\pi(\pi) > 0.05$ $ \Delta m_\phi < 10 MeV$ $ \cos \theta_{K\pi} > 0.5$	$L_K(K) > 0.5$ $L_e(\pi) + L_\mu(\pi) + L_\pi(\pi) > 0.05$ $L_e(\pi) + L_\mu(\pi) + L_\pi(\pi) \geq 0$ $ \Delta m_{D^0} < 75 MeV$
optimirani rezi	
$d(D_s^+) > 5.3$ $b(D_s^+) < 2.11$ $b_m(K^-)b_m(K^+)b_m(\pi) > 28.7$ $\sqrt{b_m(\phi)b_m(\pi)} > 0.75(t - t_0), t_0 = 1.0$	$b(D^0) < 2.4$ $b_m(K) > 2.1$ $b_m(\pi) > 1.7$ $p_{pT}(D^0) > 17.7$

Tabela II: Rezi pri selekciji dogodkov

parametrov smo uporabili še rez oblike $\sqrt[3]{b_m(K)b_m(\pi_1)b_m(\pi_2)} > 4(t-t_0)$ oz. $\sqrt{b_m(\phi)b_m(\pi)} > 0.75(t-t_0)$, kjer je razpadni čas t izražen v enotah življenjskega časa mezona D , t_0 pa izbran z optimizacijo, opisano spodaj. Pri selekciji mezonov D^{*+} smo poleg ostalih rezov uporabili še rez na produktu gibalne količine mezona D^0 in transverzalnih gibalnih količin K in π iz D^0 : $p_{pT} = p(D)p_T(K)p_T(\pi)$.

Vrednosti navedenih rezov smo določili z optimizacijskim postopkom, ki ni vključeval izmerjenih dogodkov v območju invariantne mase pričakovanega signala. Zahtevali smo, da je signifikanca signala, $s = S/\sqrt{S+B}$, največja. Z S smo označili pričakovano število mezonov D , z B pa pričakovano število dogodkov v ozadju. Pričakovano število signalnih dogodkov smo ocenili iz rekonstruiranega števila dogodkov v simulaciji Monte Carlo s predpostavko, da je presek za tvorbo mezona D enak uteženemu povprečju objavljenih rezultatov drugih eksperimentov. Ozadje B smo ocenili z linearno interpolacijo iz števila dogodkov v stranskih pasovih. Izjema je rekonstrukcija mezona D^{*+} , kjer smo ozadje ocenili iz kombinacij nevtralnega mezona D^0 s pionom z napačnim predznakom. Vse reze podajamo v tabeli II.

vzorec	D^0	D^+	D_s^+	D^{*+}
skupno	174.8 ± 16.8	148.2 ± 15.6	11.4 ± 4.0	61.3 ± 13.0
delci	75.9 ± 10.9	54.9 ± 9.4	4.9 ± 2.6	21.0 ± 6.6
antidelci	99.0 ± 11.9	92.8 ± 11.3	6.7 ± 2.9	40.6 ± 8.3
C	66.1 ± 9.6	52.9 ± 8.4	4.2 ± 2.2	26.6 ± 6.4
W	92.3 ± 11.7	78.8 ± 10.9	6.7 ± 3.0	24.8 ± 7.5
Ti	17.4 ± 5.7	16.7 ± 5.3	0.4 ± 1.0	9.6 ± 4.0

Tabela III: Število rekonstruiranih mezonov D .

mezon	merjen $c\tau$ [μm]	$\chi^2/n.d.f$	PDG $c\tau$ [μm]
D^+	302 ± 33	36/19	311.8
D^0	120 ± 13	36/24	123.0
D_s	165 ± 52	6.2/7	147.0

Tabela IV: Izmerjeni življenjski časi mezonov D . Desni stolpec podaja vrednosti svetovnega povprečja [11].

Signalni dogodki

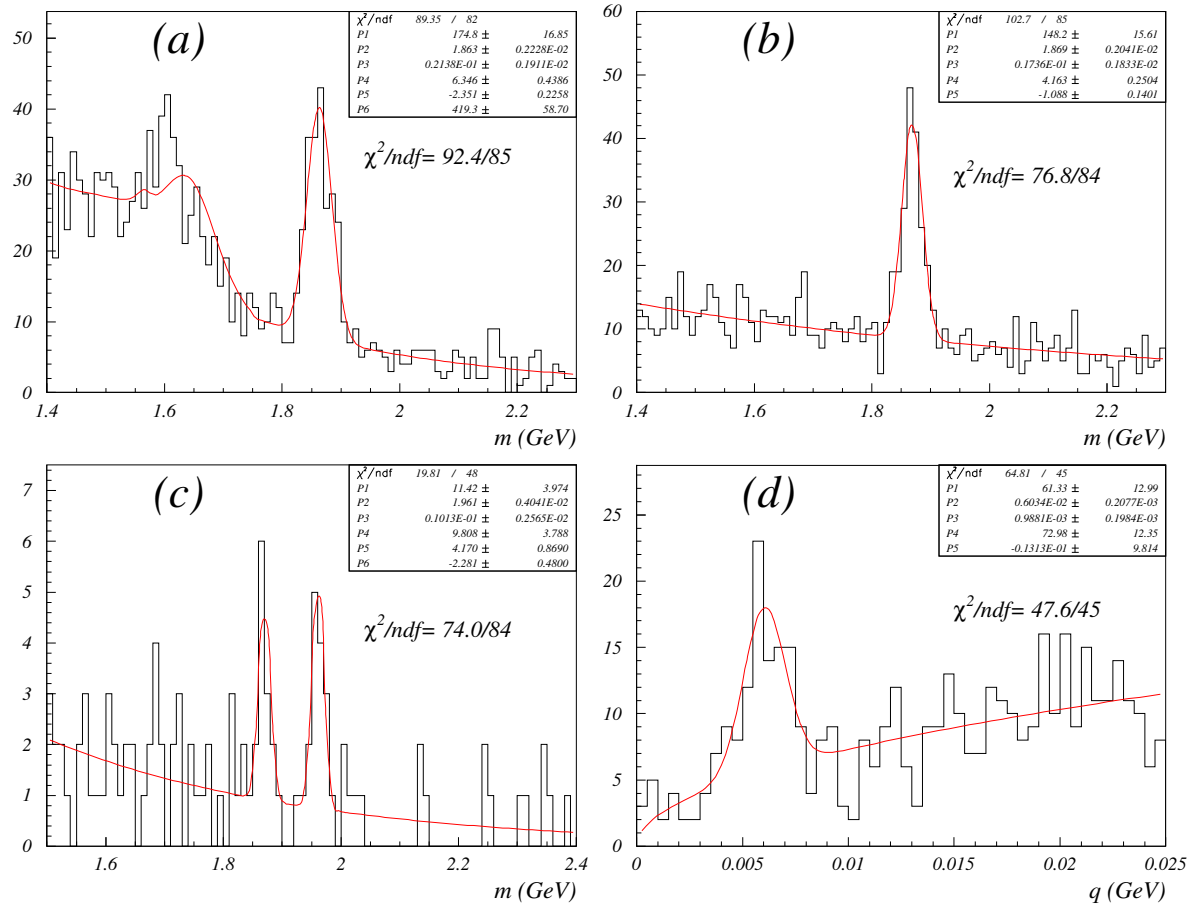
Slika I prikazuje porazdelitve po invariantni masi za dogodke, ki preživijo selekcijske kriterije iz tabele II. Rekonstruirani razpadi $D^0 \rightarrow K^- \pi^+$, $D^+ \rightarrow K^- \pi^+ \pi^+$, $D_s^+ \rightarrow \phi \pi^+ \rightarrow K^- K^+ \pi^+$ in $D^{*+} \rightarrow D^0 \pi^+ \rightarrow K^- \pi^+ \pi^+$ so vidni kot vrhovi pri ustrezni masi (oz. razliki mas) mezona D . Na sliki Ic je levo od vrha pri masi mezona D_s^+ viden tudi vrh pri masi mezona D^+ , ki ustreza razpadu $D^+ \rightarrow \phi \pi^+$.

Vrhovom v porazdelitvah smo prilagajali Gaussovo funkcijo, pri čemer so bili vsi trije parametri prosti. Ozadje smo pri D^+ in D_s^+ opisali z eksponentno funkcijo (dva prosta parametra). Pri D^0 smo dodali eksponentnemu ozadju še obliko $c\bar{c}$ ozadja, ki smo ga določili iz simulacije Monte Carlo (trije prosti parametri). Nastavek za ozadje pri D^{*+} je bil $a(q^{1/2} + bq^{3/2})$, kjer sta a in b prosta parametra, q pa je razlika invariantnih mas $q = m(K^- \pi^+ \pi^+) - m(K^- \pi^+) - m_{\pi^+}$.

Za vsakega izmed mezonov D smo tako določili število dogodkov za celoten vzorec, posebej za delce in antidelce in posebej za vrsto tarče. Številke so zbrane v tabeli III. Skupno smo rekonstruirali 175 D^0 , 148 D^+ , 11 D_s^+ in 61 D^{*+} .

Za mezone D^0 , D^+ in D_s^+ smo preverili porazdelitve po življenjskem času. Uporabljali smo simultano prilagajanje z metodo največje zanesljivosti in primerjali rezultate z vrednostmi svetovnega povprečja [11]. Rezultati skupaj z vrednostmi χ^2 nad številom prostostnih stopenj iz prilagajanja so zbrani v tabeli IV. Vsi izmerjeni življenjski časi se skladajo s svetovnim povprečjem [11].

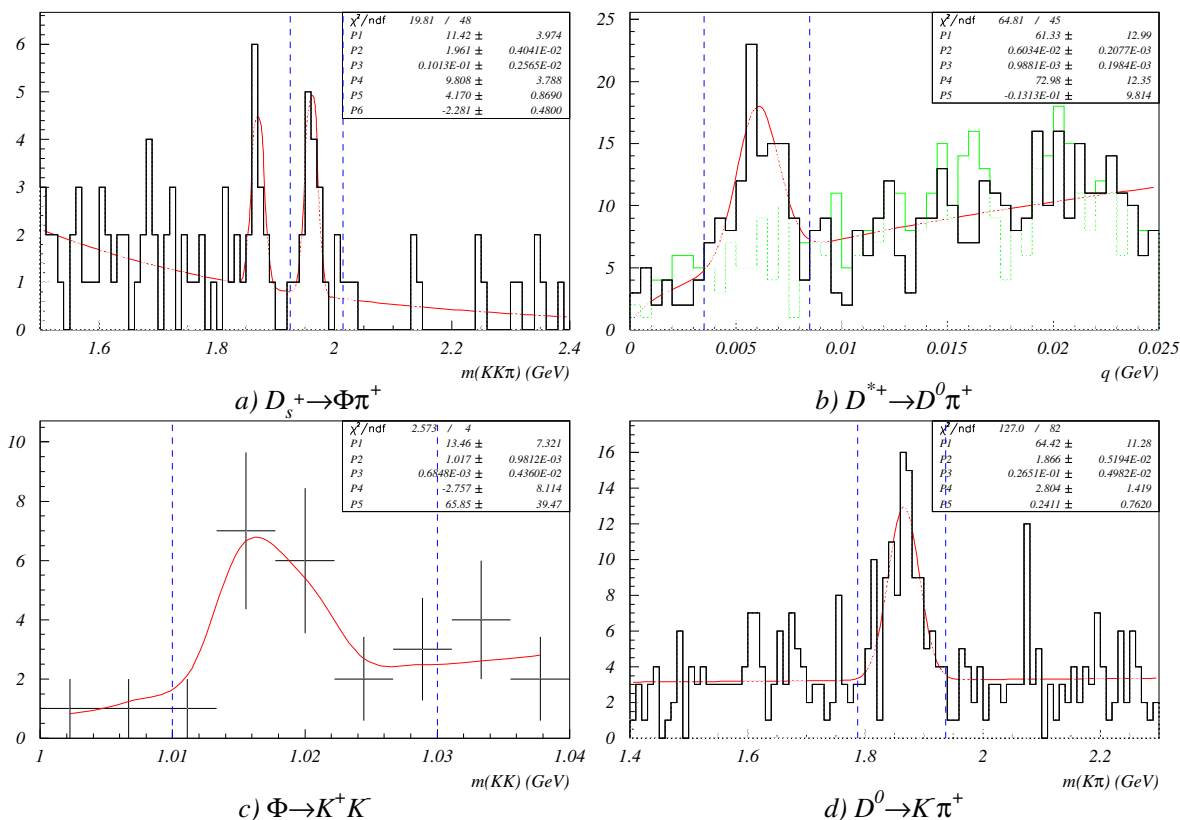
Mezona D_s^+ in D^{*+} smo rekonstruirali v dvostopenjskem razpadnem kanalu, kjer dva delca



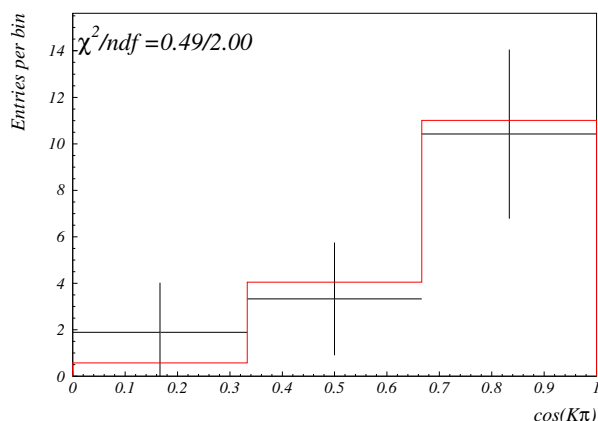
Slika I: Porazdelitev po invariantni masi za rekonstruirane razpade (a) $D^0 \rightarrow K^- \pi^+$, (b) $D^+ \rightarrow K^- \pi$, (c) $D_s^+ \rightarrow \phi \pi^+ \rightarrow (K^- K^+) \pi^+$ in (d) razlika invariantnih mas q za $D^{*+} \rightarrow D^0 \pi^+ \rightarrow (K^- \pi^+) \pi^+$ v realnih podatkih.

tvorita vmesno stanje. D_s^+ razpade v dva delca, ϕ in π^+ , in ϕ razpade v dva nabita kaona. Podobno tudi D^{*+} razpade v dva delca, D^0 in π^+ , in mezon D^0 nato rekonstruiramo v razpadu v $K^- \pi^+$. V obeh primerih sta vmesni stanji vidni v porazdelitvi po invariantni masi, če se omejimo na dogodke, kjer je invariantna masa rekonstruiranega kandidata za mezon D znotraj signalnega okna. Porazdelitve z vriscim položajem signalnega okna prikazuje slika II.

V primeru $D_s^+ \rightarrow \phi \pi^+ \rightarrow (K^+ K^-) \pi^+$ rekonstruiramo razpad psevdoskalarne delca v vektorski delec in psevdoskalar. V takih razpadih ima v težiščnem sistemu vektorskega delca le ta zaradi ohranitve vrtilne količine komponento z spina enako 0, če os z položimo v smer gibalne količine skalarne delca. Pri razpadu vektorskega delca v dva skalarna delca pričakujemo v takem primeru kotno porazdelitev sorazmerno s $\cos^2(\theta_{K\pi})$, kjer je $\theta_{K\pi}$ kot med smerjo razpadnih produktov K in π . Slika III kaže kotno porazdelitev za dogodke v signalnem oknu D_s^+ in je v skladu s pričakovano.



Slika II: Porazdelitve po invariantni masi za začetna (zgoraj) in vmesna (spodaj) stanja: (a) $D_s^+ \rightarrow \phi \pi^+$, (b) $D^{*+} \rightarrow D^0 \pi^+$, (c) $\phi \rightarrow K^- K^+$, dogodki v signalnem oknu D_s^+ in (d) $D^0 \rightarrow K^- \pi^+$, dogodki znotraj signalnega okna D^{*+} . Navpične črtkane linije označujejo signalna okna. Pri (b) smo prikazali tudi napačne nabojne kombinacije (\bar{D}^0, π^+) (zeleno).



Slika III: Kotna porazdelitev piona proti smeri kaona iz razpada $D_s^+ \rightarrow \phi \pi^+ \rightarrow K^+ K^- \pi^+$ v težiščnem sistemu ϕ za rekonstruirane signalne dogodke. Signalne dogodke smo določili tako, da smo dogodkom v signalnem oknu odšteli ozadje, ki smo ga določili z linearno ekstrapolacijo iz stranskih pasov. Pričakovana porazdelitev $\cos^2 \theta_{K\pi}$ je prikazana z rdečo črto.

$\Delta\sigma_{pN} [\mu\text{b}]$				
vzorec	D^0	D^+	D_s^+	D^{*+}
skupno	26.3 ± 2.5	10.7 ± 1.1	10.4 ± 3.6	13.0 ± 2.8
delci	11.8 ± 1.7	4.0 ± 0.7	4.2 ± 2.3	4.9 ± 1.5
antidelci	14.5 ± 1.7	6.6 ± 0.8	6.4 ± 2.7	7.9 ± 1.6
C	29.2 ± 4.3	10.9 ± 1.7	10.2 ± 5.5	16.0 ± 3.8
W	26.2 ± 3.3	11.0 ± 1.5	12.1 ± 5.5	10.1 ± 3.0
Ti	20.7 ± 6.7	9.2 ± 2.9	3.1 ± 7.6	16.2 ± 6.8

Tabela V: Izmerjeni produkcijski preseki na nukleon za območje $-0.15 < x_F < 0.05$ (kinematske porazdelitve niso preutežene). Napaka je statistična.

Produkcijski presek

Presek znotraj akceptance detektorja je podan z izrazom:

$$\Delta\sigma_{pN} = \frac{N}{Br \cdot \epsilon \cdot \sum_i \mathcal{L}_i A_i^\alpha} \quad (\text{I})$$

kjer je N število izmerjenih razpadov, Br je razvejitevno razmerje, ϵ izkoristek rekonstrukcije, A_i atomsko število, \mathcal{L}_i integrirana luminoznost i -te tarče in α parameter za odvisnost preseka od atomskega števila A .

Izkoristek rekonstrukcije ϵ smo določili iz simulacije Monte Carlo. Dogodke smo obdelali z isto programsko kodo, in analizirali z enakimi rezi, kakor realne podatke. Izkoristke smo določili posebej za delce in antidelce in posebej za vsako tarčo tako, da smo delili število rekonstruiranih mezonov s številom generiranih. Povprečni izkoristek smo določili s povprečenjem po delcih in antidelcih in z uteževanjem rezultatov za posamezne žice po enačbi:

$$\epsilon = \sum_i p_i \epsilon_i, \quad p_i = \frac{A_i^\alpha \mathcal{L}_i}{\sum_k A_k^\alpha \mathcal{L}_k} \quad (\text{II})$$

Za odvisnost preseka od atomskega števila, smo v enačbah I in II privzeli $\alpha = 1$ ter iz števila rekonstruiranih razpadov (tabela III) izračunali preseke. Rezultate smo podali v tabeli V.

Za vsak delec smo določili asimetrijo med vodilnim delcem (LP) in nevodilnim delcem ($nonLP$), ki jo definiramo kot relativno razliko presekov

$$A = \frac{\sigma_{LP} - \sigma_{nonLP}}{\sigma_{LP} + \sigma_{nonLP}} \quad (\text{III})$$

Za vodilni delec velja tak mezon, ki ima lahek valenčni kvark enak, kakor jih imajo delci v curku. V našem primeru so vodilni delci antimezoni \bar{D}^0 , D^- in D^{*-} . Obe stanji mezona D_s^+ , pozitivno in negativno, po tej definiciji nista vodilni. Za primerjavo smo tudi tu vzeli antidelec

kot vodilnega. Iz izmerjenih presekov, podanih v tabeli V, smo izračunali asimetrije in jih povzeli v tabeli VI.

	D^0	D^+	D^{*+}	D_s^+
Meritev	0.10 ± 0.09	0.25 ± 0.10	0.24 ± 0.18	0.20 ± 0.33
PYTHIA	0.24	0.22	0.23	-0.06

Tabela VI: Izmerjena asimetrija vodilnega delca proti nevodilnemu in napoved generatorja Pythia.

Podatke smo zajemali s tarčami iz treh različnih materialov, zato lahko določimo odvisnost preseka od atomskega števila A . Le-to običajno parametriziramo kot

$$\sigma_{pA} = \sigma_{pN} \cdot A^\alpha \quad (\text{IV})$$

σ_{pA} je presek na jedro, σ_{pN} presek na nukleon. Parameter α smo določili s simultanim prilagajanjem z metodo največje zanesljivosti izmerjenim porazdelitvam po invariantni masi za posamezne tarče. Število prostih parametrov pri tem prilagajanju je bilo po 8 za D^+ in D^{*+} , in po 9 za D^0 in D_s^+ . Rezultat je $\alpha = 0.98 \pm 0.04$ in se sklada s predpostavko, da je presek odvisen linearno od atomskega števila.

Kinematske porazdelitve

Izmerili smo obe projekciji diferencialnega preseka: projekcijo v prečni smeri $d\sigma/dp_T^2$ in projekcijo v vzdolžni smeri $d\sigma/dx_F$. Feynmanova spremenljivka x_F je definirana kot $x_F = 2p_z/\sqrt{s}$, kjer je p_z komponenta gibalne količine v vzdolžni smeri in je \sqrt{s} energija trka, oboje podano v težiščnem sistemu trka.

Za opis porazdelitve transverzalne gibalne količine smo uporabili nastavek:

$$\frac{d\sigma}{dp_T^2} \propto \left[1 + \left(\frac{\sqrt{\pi} \Gamma(\beta - \frac{3}{2}) p_T}{2 \Gamma(\beta - 1) \langle p_T \rangle} \right)^2 \right]^{-\beta} \quad (\text{V})$$

kjer sta $\langle p_T \rangle$ in β prosta parametra, $\Gamma(x)$ pa gama-funkcija. Enačba V je izpeljanka enačbe ki jo je uporabljal Frixione v [1].

Za opis porazdelitve po x_F navadno uporabljajo obliko

$$\frac{d\sigma}{dx_F} \propto (1 - |x_F|)^n \quad (\text{VI})$$

ki pa ne opisuje dobro porazdelitve pri majhnih x_F , kjer je porazdelitev bolj podobna Gaussovi. Funkcijo, sestavljeno iz Gaussove v osrednjem delu in enačbe VI, so uporabili pri E791 [45].

vzorec	$\langle p_T \rangle$ [GeV/c]	β	χ^2/ndf	$\langle p_T \rangle, \beta = 6$	χ^2/ndf
D^0	1.03 ± 0.09	3.3 ± 1.1	0.59	1.03 ± 0.07	0.67
D^+	1.07 ± 0.06	30 ± 76	0.83	1.04 ± 0.06	0.78
D^{*+}	1.03 ± 0.11	8.7 ± 10.1	1.13	1.02 ± 0.11	1.10
$D^0/D^+/D^{*+}$	1.03 ± 0.04	6.4 ± 2.8	0.82	1.03 ± 0.04	0.81

Tabela VII: Izmerjena parametra $\langle p_T \rangle$ in β pri porazdelitvah po transverzalni gibalni količini.

Glasi se

$$\frac{d\sigma}{dx_F} = \begin{cases} Ae^{-\frac{x_F^2}{2\sigma_g^2}} & , |x_F| < x_b \\ A'(1 - |x_F|)^n & , |x_F| \geq x_b \end{cases} \quad (\text{VII})$$

Razmerje konstant A/A' in parameter σ_g določimo tako, da je funkcija pri x_b gladka. Poleg normalizacije sta prosta parametra le potenca n in točka stika x_b .

Najprej smo primerjali porazdelitve v simulaciji Monte Carlo. Porazdelitve so si med različnimi mezoni D zelo podobne, večje pa so razlike med delci in antidelci: porazdelitev po x_F je širša za delce, kakor za antidelce. Potem smo sestavili vzorec z mešanico mezonov D , kakršno smo izmerili na podatkih. S prilagajanjem enačb V in VII smo dobili naslednje vrednosti prostih parametrov: $\langle p_T \rangle = 0.898$ GeV/c, $\beta = 4.8$, $n = 5.42$ in $x_b = 0.052$.

Diferencialni presek pri transverzalni gibalni količini p_T izračunamo iz števila dogodkov ΔN znotraj intervala širine Δp_T^2 z izrazom podobnim enačbi I:

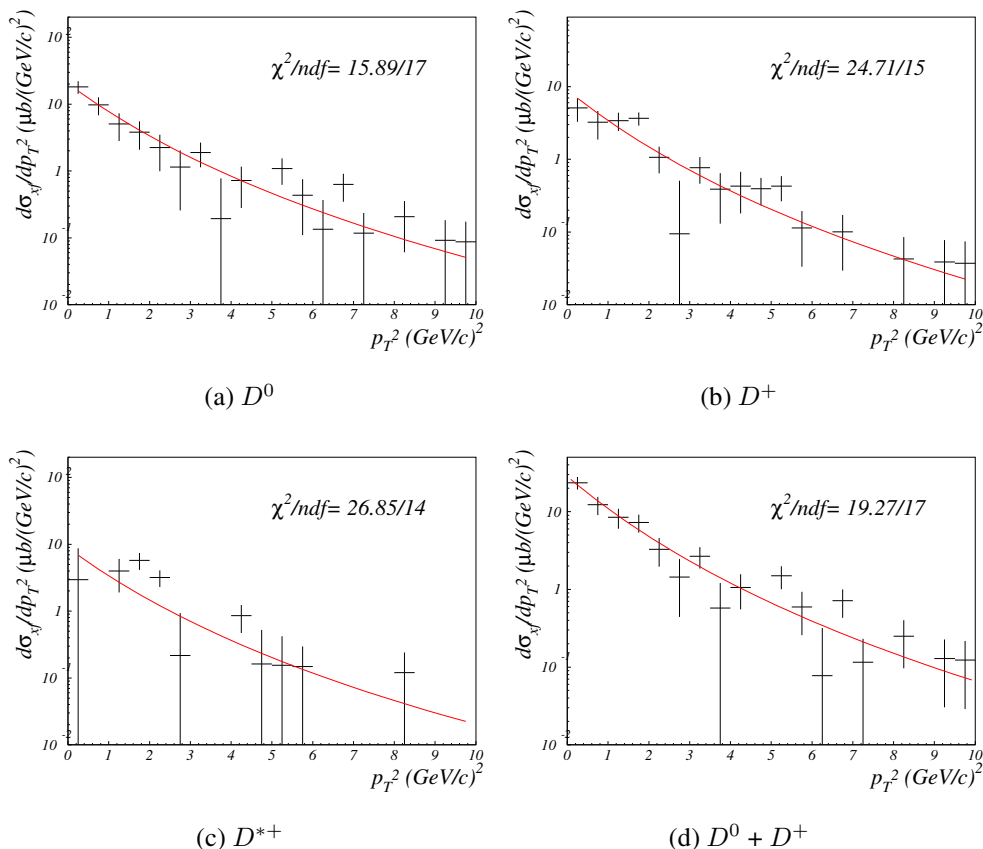
$$\frac{d\sigma}{dp_T^2} = \frac{\frac{\Delta N}{\Delta p_T^2}}{Br \cdot \epsilon(p_T^2) \cdot \sum_i \mathcal{L}_i A_i} \quad (\text{VIII})$$

kjer je $\epsilon(p_T^2)$ izkoristek za ta interval. Le-tega smo določili s simulacijo Monte Carlo na enak način, kakor skupni izkoristek. Podobno izračunamo tudi $d\sigma/dx_F$.

Izmerjene diferencialne preseke $d\sigma/dp_T^2$ v območju akceptance detektorja $-0.15 < x_F < 0.05$ prikazuje slika IV. Izmerjenim presekom $d\sigma/dp_T^2$ in $d\sigma/dx_F$ smo prilagajali nastavka V in VII. Rezultate za parametra $\langle p_T \rangle$ in β podajamo v tabeli VII. Izmerjena povprečna transverzalna gibalna količina $\langle p_T \rangle$ je signifikantno večja od tiste iz simulacije Monte Carlo, medtem ko je potenca β sicer večja a skladna s simulirano.

Pri prilagajanju $d\sigma/dx_F$ smo parameter x_b postavili na vrednost, ki so jo izmerili pri eksperimentu E791: $x_b = 0.062$ [45]. Rezultat prilagajanja, $n = 7.5 \pm 3.2$, se sklada s povprečjem objavljenih rezultatov drugih eksperimentov ($n = 7.7 \pm 1.4$ [4]). Zaradi omejene akceptance detektorja HERA-B je negotovost pri določitvi parametra n znatna.

Ker se izkoristek spreminja s p_T^2 in x_F , je za pravilno določitev skupnega izkoristka potrebno preuteževanje generiranih mezonov. Uteži za kinematski porazdelitvi smo določili iz rezultatov prilagajanja podatkom in simulaciji Monte Carlo z deljenjem normirane porazdelitve v podatkih



Slika IV: Diferencialni presek $d\sigma/dp_T^2$, s funkcijo V simultano prilagojeno z metodo največje zanesljivosti vzorcem mezonov D^0 , D^+ in D^{*+} . Vzorec mezonov D_s^+ smo izključili iz prilagajanja zaradi malega števila rekonstruiranih dogodkov. Presek (d) je vsota presekov (a) in (b).

D^0	D^+	D_s^+	D^{*+}
1.087 ± 0.032	1.126 ± 0.040	1.185 ± 0.091	1.192 ± 0.055

Tabela VIII: Faktorji za korekcijo izkoristka zaradi preuteževanja kinematskih porazdelitev.

z normirano porazdelitvijo v simulaciji Monte Carlo. Za vse mezone D smo uporabili iste uteži. Nato smo ponovno računali izkoristke za vse štiri mezone enkrat z uteženo simulacijo Monte Carlo in enkrat z neutrženo in iz razmerja določili korekcijski faktor za presek. Napako na korekcijskem faktorju smo določili tako, da smo spreminjali posamezne parametre za eno standardno deviacijo gor in dol in vzeli polovico odstopanja. Napaki iz variacije $\langle p_T \rangle$ in β smo sešteli v kvadratu. Skupni korekcijski faktorji za izkoristke zaradi preuteževanja kinematskih porazdelitev so zbrani v tabeli VIII. Za ekstrapolacijo meritve na celotni fazni prostor smo določili delež mezonov D znotraj akceptance detektorja $-0.15 < x_F < 0.05$. Ta delež smo računali z obema parametrizacijama porazdelitve po x_F in z vrednostjo eksponenta $n = 7.7 \pm$

D^0	D^+	D_s^+	D^{*+}
0.90	0.86	0.86	0.90

Tabela IX: Korekcijski faktorji za izkoristek rekonstrukcije zaradi večjega izkoristka identifikacije v simulaciji Monte Carlo v primerjavi z realnimi podatki.

1.4, ki smo ga prevzeli od rezultatov drugih eksperimentov. Povprečna vrednost rezultatov obeh parametrizacij je $f_{vis} = 0.55 \pm 0.05$.

Sistematske napake

Produksijski presek Iz enačbe I razberemo, da na sistematsko napako totalnega preseka vpliva naslednje: način štetja mezonov D , natančnost razvejitvenega razmerja, natančnost poznavanja luminoznosti in sistematske napake pri določanju izkoristka rekonstrukcije.

Sistematsko napako pri štetju dogodkov smo ocenili tako, da smo spreminjali nastavek za kombinatorno ozadje. Pri mezonih D^0 , D^+ in D_s^+ smo namesto eksponentne funkcije poskusili z linearno in s kvadratno funkcijo; večjo od obeh razlik do rezultata z eksponentnim nastavkom smo podali kot sistematsko napako. Pri mezonu D^{*+} smo poskusili z obliko ozadja, dobljeno s prilagajanjem enakega nastavka dogodkom z napačno nabojno kombinacijo ter razliko v številu dogodkov šteli v sistematsko napako.

Sistematske napake pri določanju izkoristka izvirajo iz končne statistike simulacije dogodkov, iz natančnosti simulacije detektorja in iz preuteževanja kinematskih porazdelitev v simulaciji. Natančnost simulacije detektorja prispeva k sistematski razliki med dejanskim in simuliranim izkoristkom za rekonstrukcijo in identifikacijo delcev ter izkoristkom rezov.

Sistematsko napako na izkoristku rekonstrukcije delcev smo ocenili na podlagi razpadov $K_S^0 \rightarrow \pi^+\pi^-$ in sistematsko napako pri identifikaciji delcev z razpadi $K_S^0 \rightarrow \pi^+\pi^-$ in $\phi \rightarrow K^+K^-$. Izkoristki identifikacije delcev so v realnih podatkih za $\sim 5\%$ nižji od izkoristkov v simulaciji. Iz porazdelitve kaonov in pionov po gibalni količini smo določili povprečne korekcijske faktorje izkoristka rekonstrukcije mezonov D za kaone in pione in dobili za obe vrsti mezonov za vsak identificiran delec vrednost 0.95. Faktorji za korekcijo izkoristka za posamezne mezone D zaradi identifikacije delcev so zbrani v tabeli IX.

Sistematsko napako zaradi rezov smo ocenili tako, da smo v simulaciji poslabšali natančnost rekonstruiranih sledi delcev za 10% in razliko v izkoristku šteli v napako. Deset odstotno neujemanje v ločljivosti smo predtem ocenili s primerjanjem vpadnih parametrov pionov na žico med simulacijo in realnimi podatki.

Vse prispevke k sistematski napaki na preseku podajamo v tabeli X. Celotno sistematsko napako smo dobili s seštevanjem v kvadratih.

Razmerje presekov K sistematski napaki na razmerjih presekov ne prispevajo vsi izvori v polni meri. Nekorelirani so način štetja mezonov D , statistična napaka simulacije Monte Carlo

prispevki	D^0	D^+	D_s^+	D^{*+}
štetje dogodkov	3.4%	2.6%	6.0%	9.7%
razvejitevno razmerje	1.8%	3.6%	13%	1.9%
luminoznost	3.7%	3.7%	3.7%	3.7%
statistika MC	1.2%	1.3%	3.7%	1.1%
rekonstrukcija delcev	3.0%	4.5%	4.5%	4.5%
identifikacija delcev	4.0%	6.0%	6.0%	4.0%
analizni rezi	3.2%	2.7%	4.8%	2.6%
preuteževanje	2.9%	3.6%	7.7%	4.6%
skupno	9%	11%	19%	13%

Tabela X: Prispevki k sistematski napaki na produkcijskem preseku.

prispevki	D^+/D^0	D^{*+}/D^0	$D_s^+/(D^0 + D^+)$
štetje dogodkov	4.3%	10.0%	6.3%
razvejitevno razmerje	4.0%	0.5%	13%
statistika MC	1.8%	1.6%	3.7%
rekonstrukcija delcev	1.5%	1.5%	1.0%
identifikacija delcev	2.0%	0.0%	1.4%
analizni rezi	0.6%	1.4%	1.7%
preuteževanje	1.0%	2.0%	4.5%
skupno	6%	11%	16%

Tabela XI: Prispevki k sistematski napaki na razmerjih presekov.

in razvejitevno razmerje. Pri razmerju presekov D^{*+}/D^0 upoštevamo le napako na razvejitvenem razmerju $D^{*+} \rightarrow D^0\pi^+$. Prispevki k sistematski napaki na razmerju presekov so podani v tabeli XI.

Parameter α K sistematski napaki na parametru α prispevata napaka na integrirani luminoznosti (2.2%) in statistična napaka simulacije Monte Carlo (0.6%). Celotna sistematska napaka je 2.3%.

Asimetrija vodilni-nevodilni delec Sistematsko napako na asimetriji vodilnega proti nevodilnemu delcu smo računali iz definicijske enačbe III. Prispeva le statistična napaka na simulaciji Monte Carlo. Sistematska napaka na asimetriji je 0.01 za D^0 , D^+ in D^{*+} in 0.04 za D_s^+ .

Rezultati

Produksijski presek Ko upoštevamo korekcijske faktorje iz tabel VIII in IX, dobimo iz nekorrigiranih presekov iz tabeli V končne rezultate za preseke na nukleon v akceptanci detektorja $\sigma_{pN}(D^0) = 26.8 \pm 2.6 \pm 2.1 \mu\text{b}$, $\sigma_{pN}(D^+) = 11.0 \pm 1.1 \pm 1.2 \mu\text{b}$, $\sigma_{pN}(D_s) = 10.2 \pm 3.5 \pm 1.9 \mu\text{b}$ in $\sigma_{pN}(D^{*+}) = 12.1 \pm 2.6 \pm 1.2 \mu\text{b}$.

Te vrednosti ekstrapoliramo na celotni fazni prostor v x_F tako, da jih delimo z faktorjem $f_{vis} = 0.55 \pm 0.05$, napako na faktorju pa v kvadratu prištejemo sistematskim napakam iz tabele X. Ekstrapolirani preseki na nukleon za posamezne mezone D so $\sigma_{pN}(D^0) = 48.7 \pm 4.7 \pm 6.2 \mu\text{b}$, $\sigma_{pN}(D^+) = 20.0 \pm 2.0 \pm 2.9 \mu\text{b}$, $\sigma_{pN}(D_s) = 18.5 \pm 6.4 \pm 3.9 \mu\text{b}$ in $\sigma_{pN}(D^{*+}) = 22.0 \pm 4.7 \pm 3.5 \mu\text{b}$. Izmerjene preseke podajamo tudi v tabeli XII.

Ob upoštevanju energijske odvisnosti preseka lahko naše meritve primerjamo z obstoječimi meritvami pri drugih energijah. Primerjavo prikazuje slika V. Merskim točkam smo prilagajali nastavek

$$\sigma(\sqrt{s}) = p_0 \cdot \left(1 - \frac{p_1}{\sqrt{s}^{p_3}}\right)^{p_2} \quad (\text{IX})$$

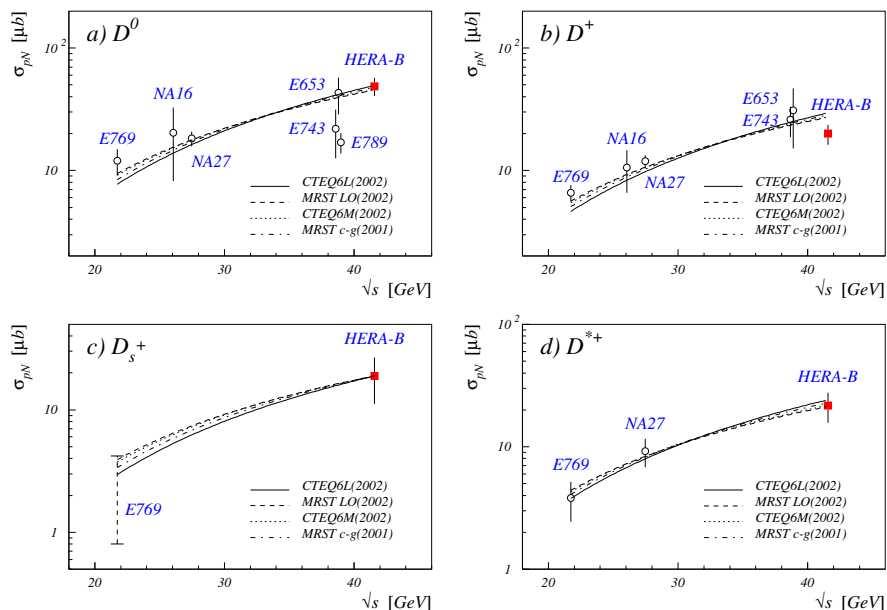
iz [4]. Naše merske točke so skladne z obstoječimi meritvami.

Vsota presekov na nukleon $\sigma(D^0) + \sigma(D^+) + \sigma(D_s^+) = 87.2 \pm 8.2 \pm 11.6 \mu\text{b}$ predstavlja $(89.1 \pm 4.1)\%$ celotnega preseka za tvorbo kvarka c [11]. Iz tega dobimo produktijski presek za par kark-antikvark $\sigma(c\bar{c}) = 48.9 \pm 4.6 \pm 6.9 \mu\text{b}$. Sistematsko napako smo ocenili s pomočjo simulacije Monte Carlo.

Razmerje presekov Iz rezultatov v tabeli XII smo izračunali razmerja presekov: razmerje $\sigma(D^+)/\sigma(D^0) = 0.41 \pm 0.06 \pm 0.02$ je najbolj natančna meritev v trkih protonov z jedri in se dobro ujema z obstoječimi meritvami, kakor tudi s svetovnim povprečjem v trkih hadronov z nukleoni 0.41 ± 0.03 [4]. Naša meritev je tudi skladna z napovedjo 0.42 iz izsospinskega modela. Razmerje $\sigma(D^{*+})/\sigma(D^0) = 0.45 \pm 0.11 \pm 0.05$ se dobro ujema z rezultati eksperimentov E769 in NA27. Rezultat za razmerje $\sigma(D_s^+)/(\sigma(D^0) + \sigma(D^+)) = 0.28 \pm 0.10 \pm 0.05$ odstopa za eno standardno deviacijo od napovedi 0.20 iz [1] in za 1.6 standardnih deviacij od svetovnega povprečja 0.10 ± 0.02 meritev na trkalnikih e^+e^- [11].

	$\sigma[\mu\text{b}]$			
	D^0	D^+	D_s^+	D^{*+}
vidni presek	$26.8 \pm 2.6 \pm 2.4$	$11.0 \pm 1.1 \pm 1.2$	$10.2 \pm 3.5 \pm 1.9$	$12.1 \pm 2.6 \pm 1.6$
totalni presek	$48.7 \pm 4.7 \pm 6.2$	$20.0 \pm 2.0 \pm 2.9$	$18.5 \pm 6.4 \pm 3.9$	$22.0 \pm 4.7 \pm 3.5$

Tabela XII: Preseki na nukleon znotraj akceptance detektorja $-0.15 < x_F < 0.05$ (vidni presek) in ekstrapolirani na celotno območje v x_F (totalni presek)



Slika V: Primerjava z rezultati drugih eksperimentov. Parametre za prilagajanje funkcije IX za različne teoretske opise smo prevzeli iz [4]

Delež vektorskih mezonov v hadronizaciji Ker vsi vektorski mezoni D razpadejo preko močne interakcije v skalarne mezone D , lahko delež vektorskih mezonov v hadronizaciji, P_V , določimo iz izmerjenih presekov:

$$P_V = \frac{\sigma(D^{*0}) + \sigma(D^{*+})}{\sigma(D^0) + \sigma(D^+)} \quad (\text{X})$$

S predpostavko, da imamo v hadronizaciji enako število kvarkov u in d (invarianca na izospin), lahko iz meritve dveh presekov izračunamo vrednost P_V :

$$R_1 = \frac{\sigma(D^+)}{\sigma(D^0)} \quad P_V = \frac{1 - R_1}{(1 + R_1) Br_{(D^{*+} \rightarrow D^0)}} = 0.62 \pm 0.08 \pm 0.04 \quad (\text{XI})$$

$$R_2 = \frac{\sigma(D^{*+})}{\sigma(D^0)} \quad P_V = \frac{R_2}{1 - R_2 \cdot Br_{(D^{*+} \rightarrow D^0)}} = 0.65 \pm 0.22 \pm 0.10 \quad (\text{XII})$$

$$R_3 = \frac{\sigma(D^{*+})}{\sigma(D^+)} \quad P_V = \frac{R_3}{1 + R_3 \cdot Br_{(D^{*+} \rightarrow D^0)}} = 0.63 \pm 0.09 \pm 0.05 \quad (\text{XIII})$$

Naše vrednosti se dobro ujemajo z svetovnim povprečjem $P_V = 0.59 \pm 0.01$ [4].

Asimetrija vodilni-nevodilni delec Izmerili smo asimetrijo med preseki za vodilne in nevodilne delce in rezultate padali v tabeli XIII. Napovedi iz generatorja Pythia se dobro ujemajo z meritvijo.

	D^0	D^+	D^{*+}	D_s^+
Meritev	$0.10 \pm 0.09 \pm 0.01$	$0.25 \pm 0.10 \pm 0.01$	$0.24 \pm 0.18 \pm 0.01$	$0.21 \pm 0.33 \pm 0.04$
PYTHIA	0.24	0.22	0.23	-0.06

Tabela XIII: Asimetrije med preseki za vodilne in nevodilne delce. V enačbi III smo pri D_s^+ uporabili presek za antidelec kot vodilni delec.

Parameter α Za parameter odvisnosti od atomskega števila α smo izmerili vrednost $\alpha = 0.98 \pm 0.04 \pm 0.03$. Eksperiment E789 je objavil vrednost $\alpha = 1.02 \pm 0.03 \pm 0.02$. Oba rezultata se ujemata in kažeta, da je produkcijski presek linearno odvisen od atomskega števila jeder v tarči.

Izjavljam, da je disertacija rezultat samostojnega raziskovalnega dela.

Ljubljana, v juniju 2007

Samo Kupper